Ph. D. Thesis

Optical characterization and device application of BiSb in the infrared region

Hajime Nishiyama

A thesis submitted for the degree of Doctor of Engineering at Institute of Science Tokyo in 2025

Department of Electrical and Electronic Engineering

Supervisor: Prof. Dr. Pham Nam Hai

Thesis Defense Committee:

Professor Pham Nam Hai (Chair)

Professor Shigeki Nakagawa

Professor Takaaki Manaka

Professor Akira Yamada

Associate Professor Shinsuke Miyajima

Professor Wakana Kubo

Professor Yukio Kawano

Abstract

The mid-infrared (MIR) region of electromagnetic spectrum is important for characterizing the vibrational modes of various chemical and biomolecular compounds. BiSb, a material known as a first discovered topological insulator (TI), has the smallest bulk bandgap of only 20 meV among TIs, making it suitable for MIR detection. In addition to its absorption of MIR light, BiSb has a large Seebeck coefficient, suggesting that BiSb is suited as an absorber of a MIR photothermoelectric (PTE) detector.

This thesis presents the first comprehensive studies of the optical properties and device application of BiSb topological insulator in the infra-red region. Firstly, we measure the infrared optical constants (n, κ) of topological insulator BiSb thin films using the reflectance-transmittance method in the infrared (IR) region. We reveal that Bi, $Bi_{90}Sb_{10}$, and $Bi_{85}Sb_{15}$ stand-alone thin films show absorption of about 30% for film thicknesses around 20 nm and a large refractive index ranging from 6 to 9 in the infrared region. Secondly, we fabricate PTE detectors of BiSb and measure PTE responses. We demonstrate that BiSb films deposited on flexible Kapton substrate shows a large output of 170 μV, indicating compatibility with future flexible MIR detector systems.

Our results highlight the potential of BiSb as a MIR detection material suitable for PTE imaging devices, especially when low fabrication cost and high spatial resolution are required. BiSb-based PTE devices can be fabricated by the magnetron sputtering, which is the industrial-friendly dry process.

In Chapter 1, we introduce the background of this thesis, with focus on the IR technology and TI materials. We explain the importance of the IR technology and various types of IR detectors. We briefly explain TI and describe BiSb as the first discovered 3D

TI with a very small band gap. Finally, we state the motivation for this research and the thesis outline.

In Chapter 2, we introduce the fundamental properties of BiSb as a TI and its potential for thermoelectric detectors. We discuss the prospect of BiSb as a material candidate for IR detectors, which is the most important part for this thesis as it supports the motivation of this thesis.

In Chapter 3, we show experimental methods, including sample preparation and measurements.

In Chapter 4, we determine the (n,κ) of BiSb thin films by the RT method in the 0.1 eV-1 eV range. This chapter shows that BiSb has the potential to be a good material for MIR detectors, which can be fabricated with an easy process and low cost.

In Chapter 5, we demonstrate that $Bi_{90}Sb_{10}$ thin films fabricated by magnetron sputtering exhibit strong photothermoelectric responses in the MIR region. The PTE response is systematically evaluated for various device geometries on both sapphire and Kapton substrates. The results in this chapter highlight the potential of sputtered BiSb thin films for high spatial resolution MIR detector arrays with low fabrication cost.

In Chapter 6, we discuss the future prospects and summarize this thesis.

List of Abbreviations

SHA	spin Hall angle
SHE	spin Hall effect
SSE	spin Seebeck effect
XRD	X-ray diffraction
XRR	X-ray reflectivity
XRF	X-ray fluorescence spectrometry
THz	terahertz
IR	infrared
MIR	mid infrared
NIR	near infrared
TI	topological insulator
TSS	topological surface state
PTE	photothermoelectric effect
PVE	photovoltaic effect
PCE	photoconductive effect
PGE	photogating effect
PBE	photobolometric effect

List of symbols

f	wavelength
λ	frequency
S	Seebeck coefficient

Index

Chapter 1. Introduction

1-1 Infrared technology

1-1-1 Overview of IR and detection mechanism

Terahertz(THz) - Infrared (IR) are electromagnetic region between electromagnetic wave and photonics (Fig. 1.1.1.1). The mid-infrared (MIR) region of the electromagnetic spectrum is important for characterizing the vibrational modes of various chemical and biomolecular compounds. As a result, this spectral region is highly suitable for chemical or biological sensing, with many applications in various fields, such as medical diagnostics, infrastructure monitoring, and security scanning [1].

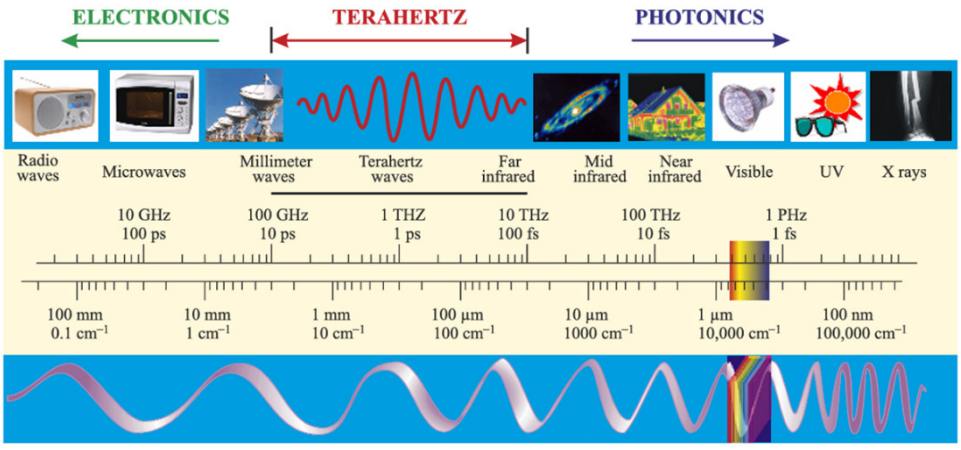

Fig. 1.1.1.1 Electromagnetic spectrum [2].

There are mainly two types of infrared detectors; photon detector and thermal detector [3]. Photon detector converts light directly into electrical signal, while thermal detector converts light into heat and then heat into resistance (bolometer), pressure (Golay cell),

and so on. For the photon detector, photovoltaic effect (PVE), photoconductive effect(PCE), photogating effect(PGE) are used. For the thermal detector, photothermoeffect (PTE), thermopile, pyroelectric effect, photobolometric effect (PBE), and Golay cell are used. Each type of detectors has advantages and disadvantages as shown in table 1.1.1.1. Photon detectors operate at high speed and high sensitivity, but require cooling for low energies. On the other hand, thermal detectors operate at room temperature but at low speed and low sensitivity. Thermal detectors have a potential to be a useful infrared detector operating at room temperature, if speed and sensitivity are improved. Here, we introduce these detection mechanisms including the narrow gap semiconductor HgCdTe detector and the quantum well IR photodetector.

Table 1.1.1.1 Comparison of the representative photodetection mechanism [4,5].

	Photon	Thermal		
	PVE	**PTE**	**Pyroelectric**	**PBE**
Mechanism	Separation of electron-hole pairs	Seebeck effect	Pyroelectric effect	Resistance change by temperature
Spectral response	Narrowband	Broadband	Broadband	Broadband
Chopper	Unnecessary	Unnecessary	Necessary	Unnecessary
Speed	Fast	Slow	Slow	Slow
External power source	Unnecessary	Unnecessary	Unnecessary	Necessary
Dominating noise	Johnson noise	Johnson noise	Johnson noise Dielectric loss	Johnson noise 1/f noise
Temperature stabilizer	Unnecessary	Unnecessary	Necessary	Necessary
Cooling unit	Unnecessary (Necessary for low energy)	Unnecessary	Unnecessary	Unnecessary

HgCdTe is a narrow-bandgap semiconductor whose energy gap can be continuously tuned by varying the alloy composition, enabling bandgap engineering over a wide infrared spectral range (Fig.1.1.1.2). HgCdTe IR detectors operate as intrinsic semiconductor photodetectors in which incident infrared radiation generates electron–hole pairs through interband absorption. Owing to the tunable bandgap, the spectral response can be modified by adjusting the alloy composition, and the photoexcited carriers are collected by an electric field to produce a measurable photocurrent. [6]

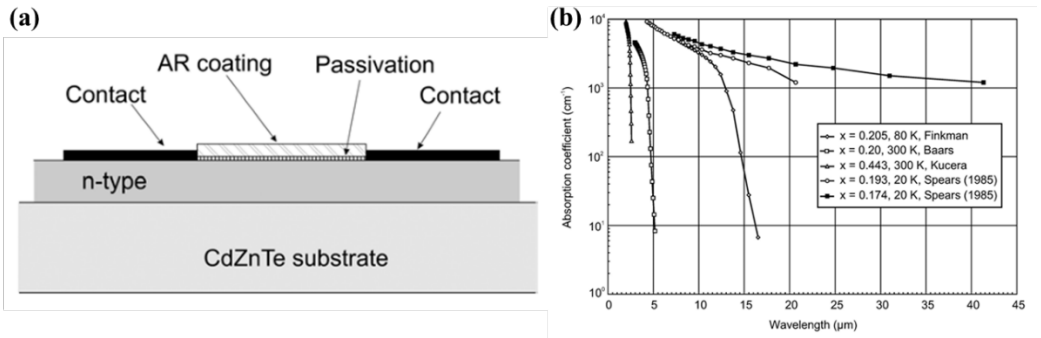

Fig. 1.1.1.2 (a) Schematic diagram of IR detector of HgCdTe. (b) IR absorption coefficient of HgCdTe [6]. Reprinted with permission from Reports on Progress of Physics.

PVE detector consists of different materials which constitute p-n junctions or Schottky junctions, as shown in Fig. 1.1.1.3. When light is irradiated onto the semiconductor's p−n junction or Schottky barrier with sufficient energy, electron−hole pairs are generated. The electron-hole pairs are separated and moved by the built-in electric field at the p-n junction or Schottky barrier, where electrons and holes accumulate in opposite junction areas, resulting in an open-circuit voltage that opposes the direction of the internal electric field. PVE detector can be fabricated by local doping of semiconductors, construction of heterogeneous structures, and formation of contacts with metals. The response time is fast, and cooling units, temperature stabilizers, or choppers are not required. Materials such as InGaAs, InSb are used in IR PVE detectors [5].

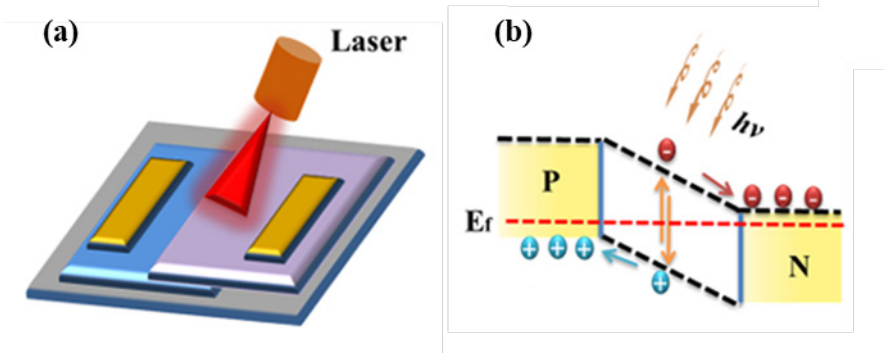

Fig.1.1.1.3 (a) Schematic diagram of PVE detector. (b) Working principle diagram of PVE detector [7]. Reprinted with permission from Materials Today Communications.

PCE detectors generally consists of semiconductors (Fig.1.1.1.4). When light is irradiated onto a semiconductor material with sufficient energy, the material which absorbs energy excites an excess of charge carriers, which increases the concentration of free carriers and reduces the resistance of the semiconductor. As a result, the conductivity increases and this change is detected. When the photon energy of the irradiated light is larger than the material's bandgap, electrons in the valence band get excited into the conduction band, which creates photogenerated electron−hole pairs. Under an external bias voltage, electrons / holes are moved toward the source / drain electrode, which realizes a large current. Under dark conditions, a limited number of charge carriers get excited by the bias voltage, which generates a small dark current. Materials such as MCT, PbS are used for PCE detectors [5].

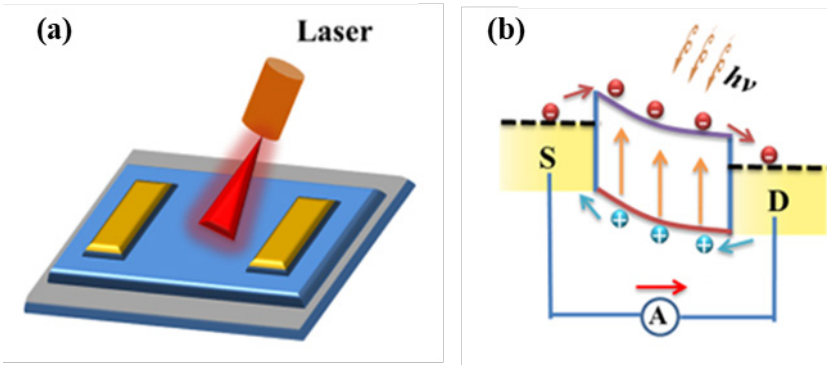

Fig. 1.1.1.4 (a) Schematic diagram of PCE detector. (b) Working principle diagram of PCE detector [7]. Reprinted with permission from Materials Today Communications.

PGE is a special case of PCE. PGE detector consists of materials with defects or quantum wells which trap electrons or holes in trap states. This trap hinders the recombination of the electrons and holes, which makes the carrier lifetime longer. This realizes an enhanced photocurrent. In addition, the charge trap states act as local floating gates that modulate the channel conductivity, by which the conductivity can be effectively controlled. electrons and holes continuously moved before recombination, which enhances optical response. However, these transfer and trapping process are a cause of slow response. [5]

Quantum well infrared photodetectors (QWIP) (Fig. 1.1.1.5) utilize intersubband optical absorption in semiconductor heterostructures, where incident radiation promotes carriers to higher-energy states that enable charge transport under an applied electric field. The resulting change in carrier transport is detected as an electrical signal. Materials such as AlGaAs / GaAs are used. [2]

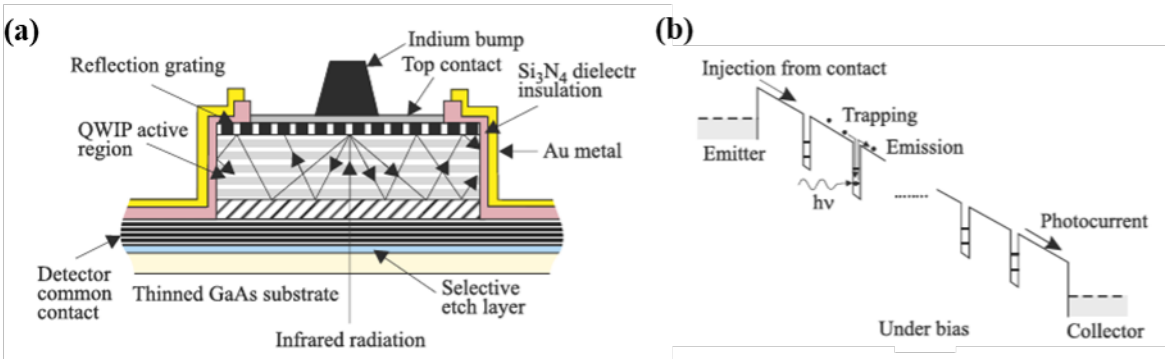

Fig. 1.1.1.5 (a) Schematic diagram of QWIP detector. (b) Working principle diagram of QWIP detector [2].

PTE detectors consist of a photo absorbing material and electrodes (Fig.1.1.1.6). PTE involves a conversion of light into heat, and heat into electrical signal. The latter conversion can be achieved by the thermoelectric Seebeck effect. Seebeck effect is a phenomenon that a voltage is generated along a temperature difference of a material, and it is expressed as $V = S\Delta T$, where V is a voltage, S is Seebeck coefficient, ΔT is a temperature difference. Although the response is slow, cooling, temperature stabilizer, or chopping are not required. Furthermore, the dominant noise is just the Johnson noise. Materials such as graphene, black phosphorus are used in PTE detectors [5].

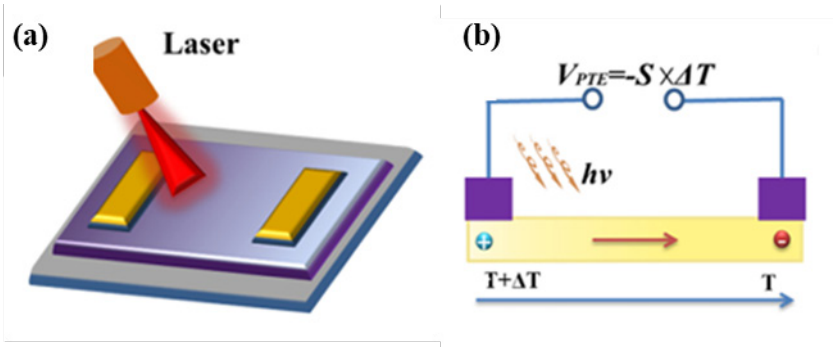

Fig. 1.1.1.6 (a) Schematic diagram of PTE detector. (b) Working principle diagram of PTE detector [7]. Reprinted with permission from Materials Today Communications.

The thermocouple (Fig. 1.1.1.7) is one type of the PTE detectors The thermocouple consists of two different metals or semiconductors, and an absorber material. When light is irradiated, absorption difference occurs between distinct parts of the thermocouple, which makes temperature gradient and PTE voltage. It is known that the sensitivity of the thermocouple is not as good as bolometers or pyroelectric detectors. [8]

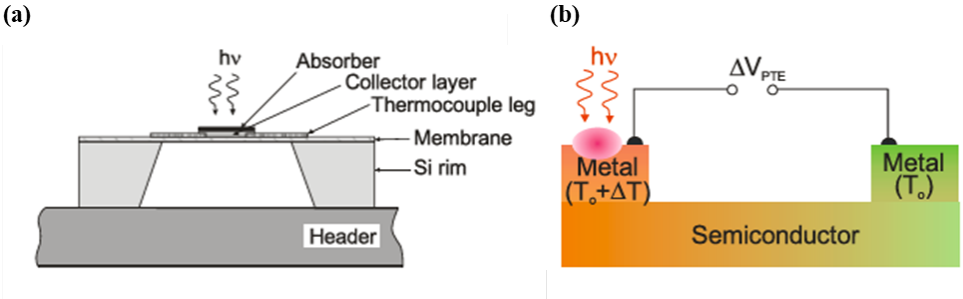

Fig. 1.1.1.7 (a) Schematic diagram of thermocouple detector. (b) Working principle diagram of thermocouple detector [8].

The pyroelectric detector (Fig.1.1.1.8) is a small capacitor which consists of two conducting electrodes. The electrodes are mounted perpendicularly to a spontaneous polarization. When light is irradiated, the change in polarization makes a charge on the capacitor, which generates a current. The magnitude of the current is related to the temperature rise and the pyroelectrical coefficient of the material. The pyroelectric detector responses in broadband wavelength, and there is no need of external power

source and cooling unit. However, the detected signal needs to be chopped or modulated. The response speed is slow. Materials such as BTO, PVDF are used [8].

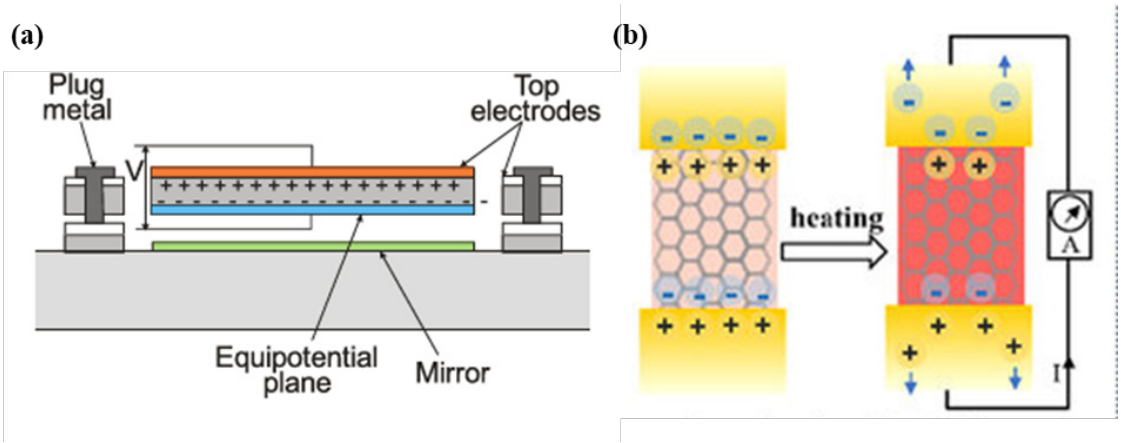

Fig. 1.1.1.8 (a) Schematic diagram of pyroelectric detector [8]. (b) Working principle diagram of pyroelectric detector [9]. Reprinted with permission from Nanotechnology.

The main material of PBE detector (Fig. 1.1.1.9) is photosensitive material whose thermal resistance changes by the temperature change. Therefore, a material with a small thermal capacity and large temperature coefficient is desirable. The thermal resistance is expressed as:

$$R_{\mathrm{h}} = \frac{\mathrm{d}T}{\mathrm{d}P} \ , \qquad (1.1.1.1)$$

where $\mathrm{d}P$ is the incident radiation absorbed by the detector, $\mathrm{d}T$ is the temperature difference, which is related to the sensitivity of the detector. PBE is similar to PCE in that the resistance changes in the photoresponse, but, in case of PBE, there is no direct photon-electron interaction. PBE detector needs an external bias voltage to observe photoinduced change in electrical conductivity via photocurrent. However, cooling, temperature stabilizers, and choppers are not required. Materials such as VOx, CdS are used [5].

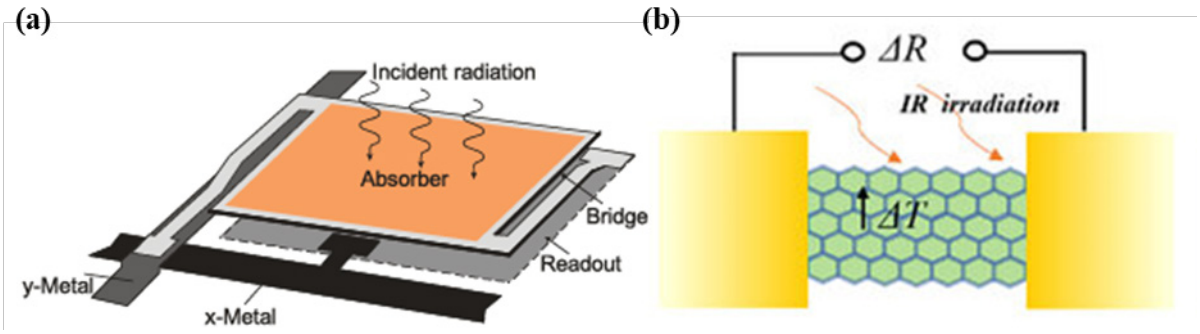

Fig. 1.1.1.9 (a) Schematic diagram of PBE detector [2]. (b) Working principle diagram of PBE detector [9]. Reprinted with permission from Nanotechnology.

The Golay cell (Fig. 1.1.1.10) consists of a gas (usually xenon for its low thermal conductivity) and an additional absorber material. When light is irradiated, a gas expansion occurs inside a hermetically sealed container, which distorts a flexible membrane. The distortion of the membrane is detected via optical system (a capacitive detector or a tunneling displacement transducer). Inside the gas container is the cavity with reflective walls, which enhances the absorption. The noise of the Golay cell is the temperature noise caused by the thermal exchange between the gas and the additional absorber. The response time is about ~ms [2].

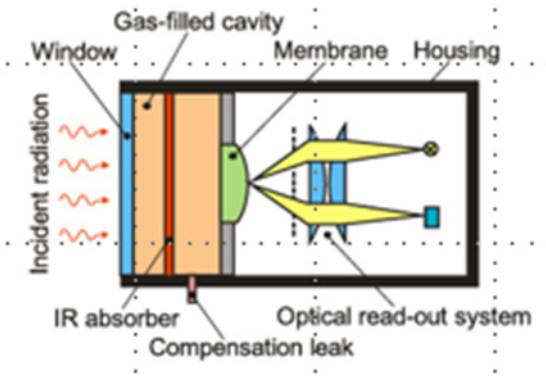

Fig. 1.1.1.10 (a) Schematic diagram of Golay cell [2].

1-1-2 PTE IR detector

In this chapter, we introduce PTE IR detectors using materials: black phosphorus, graphene, PEDOT:PSS, CNT film, and single-metal thermocouples [4].

Black phosphorus (BP) is a direct bandgap semiconductor. It is known that the bandgap of BP is changed from ~0.3 to ~2 eV when decreasing the thickness from the bulk to the monolayer [10]. When approaching 10 nm, the bandgap is still close to the bulk value. The MIR response originating from the interband absorption of BP has been observed in the multilayer BP [11]. A single-pixel PTE detector of BP has been developed [12] and the spatial resolution is ~720 nm under 1550 nm illumination, which is near the diffraction-limited resolution (~ λ /2). BP is also known for its strong in-plane anisotropy.

The polarization-sensitive PTE detector using BP was fabricated [13] and it responses in a range from 400 to 1700 nm (Fig. 1.1.2.1), where the responsivity is 0.35 mA W^{-1} at 1200 nm. The response time is ~ 40 μs, which is limited by the measurement setup. However, BP photodetector has a critical issue that it is chemically unstable. To tackle the drawback, the selenium-doped BP terahertz photodetector operating at room temperature has been reported [14].

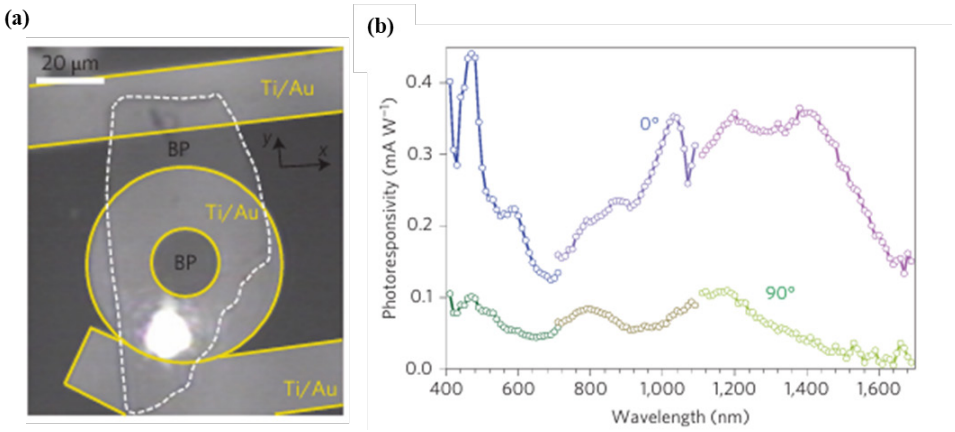

Fig. 1.1.2.1 (a) Optical image of a black phosphorus photodetector. (b) Polarization-sensitive reflection spectrum of the black phosphorus photodetector [13]. Reprinted with permission from Nature Nanotechnology.

Graphene is two-dimensional nanomaterial of carbon. The use of graphene for photodetectors has been investigated. Graphene photodetectors have ultra-broadband light absorption and ultrafast response speed due to the zero bandgap and the high mobility, respectively [15,16]. Although its thermal conductivity is high (~2500 Wm^{-1}

K^{-1} for suspended monolayer graphene) and Seebeck coefficient is small [17,18], graphene can be used for PTE detector using hot-carrier. Basically, the temperature of electron is assumed to be equal to the lattice temperature. However, in the case of graphene, hot carriers can be generated by optical excitation. When light is irradiated, the absorbed energy of electron-hole pairs is dissipated rapidly among the charge carriers due to the strong electron–electron interaction, which generates hot carriers (Fig. 1.1.2.2) [19]. Meanwhile, due to the weak electron- phonon interaction, energy transfer between carriers and lattice are suppressed [20,21].

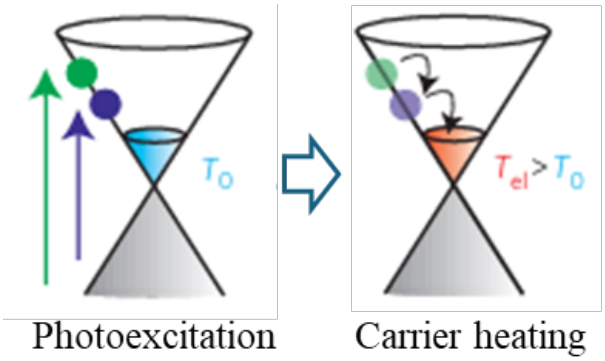

Fig. 1.1.2.2 Schematic of the generation of hot electrons in graphene [19]. Reprinted with permission from Nature Nanotechnology.

A terahertz PTE detector of graphene operating at the room temperature has been reported (Fig. 1.1.2.3) [22]. The detector is designed with asymmetric metal electrodes with different work functions (Au, Cr) to realize a temperature gradient under global illumination. The PTE response to 1.54 μm radiation was measured and the responsivity is ~0.25 V W^{-1}, which is lower than that of 1.19 μm irradiation due to the optical phonon emission during the energy-relaxation process of hot carriers.

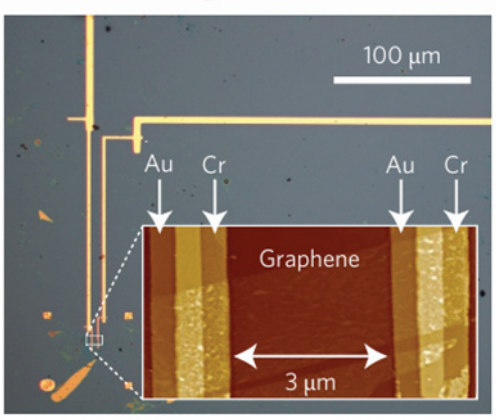

Fig. 1.1.2.3 AFM image of a graphene photodetector [22]. Reprinted with permission from Nature Nanotechnology.

PEDOT:PSS is a conductive polymer known for its mechanical flexibility and tunable electrical properties, while graphene offers high carrier mobility and broadband optical absorption. By combining these materials, PEDOT:PSS/graphene composites provide an effective platform for IR detection. IR absorption in graphene induces changes in carrier dynamics or local temperature, which are transferred to the polymer matrix through interfacial coupling, leading to a detectable electrical response (Fig. 1.2.2.4) [23].

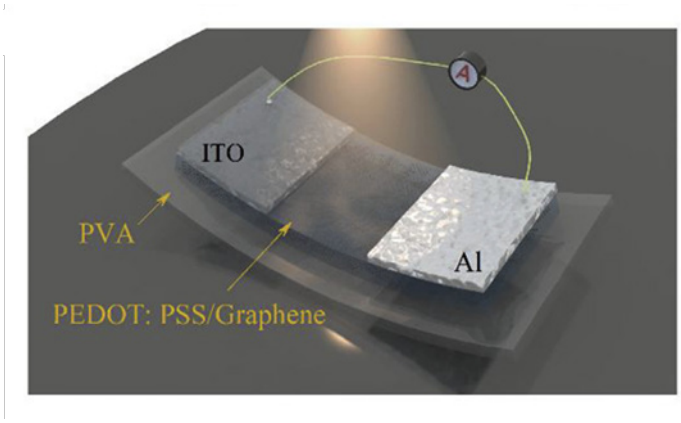

Fig. 1.1.2.4 Schematic of PEDOT:PSS/Graphene IR detector [23]. Reprinted with permission from Carbon.

CNT film (Fig. 1.1.2.5 (a)) is known for its broadband absorption characteristic ranging from THz-IR (Fig. 1.1.2.5 (b)) and large Seebeck coefficient. Broadband detection of

THz-IR using CNT film has been investigated [24]. PTE IR detection is also reported (Fig. 1.1.2.5 (c)).

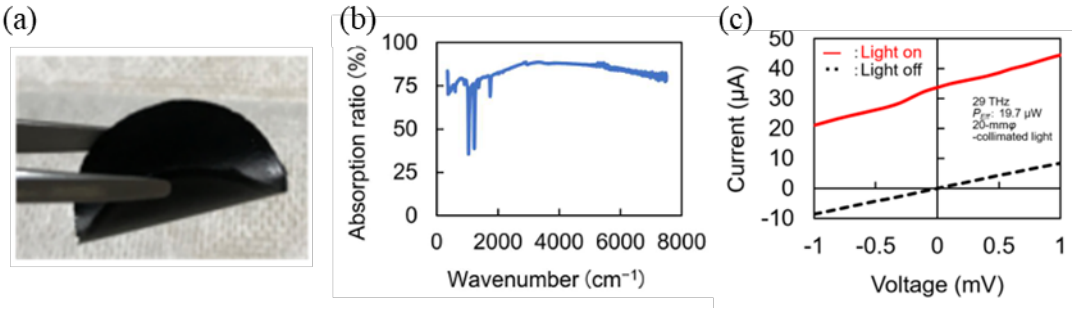

Fig. 1.1.2.5 (a) Schematic of CNT film [24]. (b) IR absorption of CNT film [25]. (c) PTE IR response of CNT film detector under the radiation of 29 THz (~10.3 μm) [24].

An antenna-coupled single-metal thermocouple for the polarization-sensitive IR detection has been reported (Fig. 1.1.2.6) [26]. In this device, Ni was employed as the active material where heat is generated. The relative Seebeck coefficient of the junction of the edge (wide part of Ni) and antenna (narrow part of Ni) is about 0.61 μV K^{-1}. The configuration of the two antennas (left and right) makes the detector polarization sensitive. When the polarization of incident IR is parallel to the left antenna arm, photoinduced current occurs in the left arm and only the left arm is heated, which makes the temperature difference and therefore a PTE voltage arises. By optimizing the length of the antenna arm, the temperature difference and the responsivity can be enhanced. The estimated detectivity at the incident wavelength of 10.6 μm is about $1 \cdot 10^5$ cm$\sqrt{\text{Hz}}$/W.

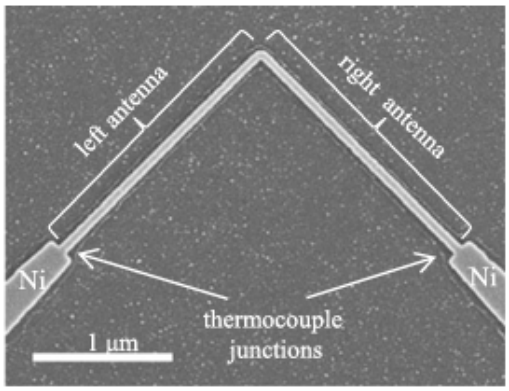

Fig. 1.1.2.6 SEM image of a metal thermocouple photodetector [26]. Reprinted with permission from IEEE Transactions on Nanotechnology.

1-2 Topological insulator

1-2-1 Band structure and significant characteristics of TI

TI is a material which has an insulating bulk and conductive surfaces. This unique characteristic comes from the strong spin-orbital coupling (SOC) of the constituent atoms. Due to the strong SOC, band inversion occurs (Fig. 1.2.1.1). In this inversion, the conduction band goes up over the Fermi level, while the valence band goes down under the Fermi level. As the conduction and valence bands have different parity, the new band is produced crossing between the bulk conduction band and bulk valence band so as to connect the band of the same parity. This band is called an edge band in 2D TI), or surface band in 3D TI, and correspond to the edge or surface conduction channels, respectively. Electron on the surface of the TI has a spin direction perpendicular to its momentum; the so-called spin-momentum locking (Fig. 1.2.1.2 (c)). The energy band of 3D TI is called Dirac cone (Fig. 1.2.1.2 (d). Although graphene also has Dirac cones, spin-momentum locking is only observed in the Dirac cones of the topological surface states of TI.

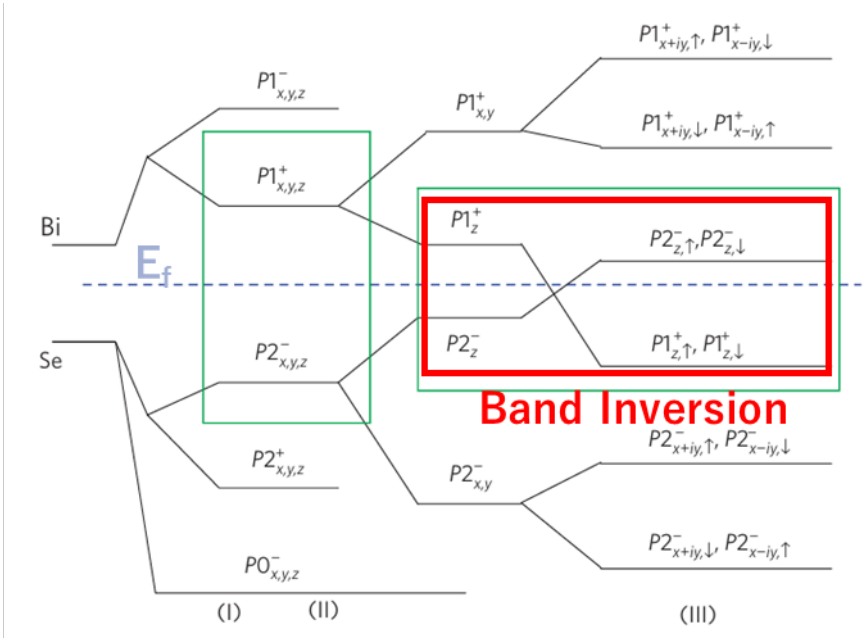

Fig. 1.2.1.1 Schematic diagram of the evolution from the atomic $P_{x,y,z}$ orbitals of Bi and Se into the conduction and valence bands of Bi_2Se_3 at the point [27]. Reprinted with permission from Nature Physics.

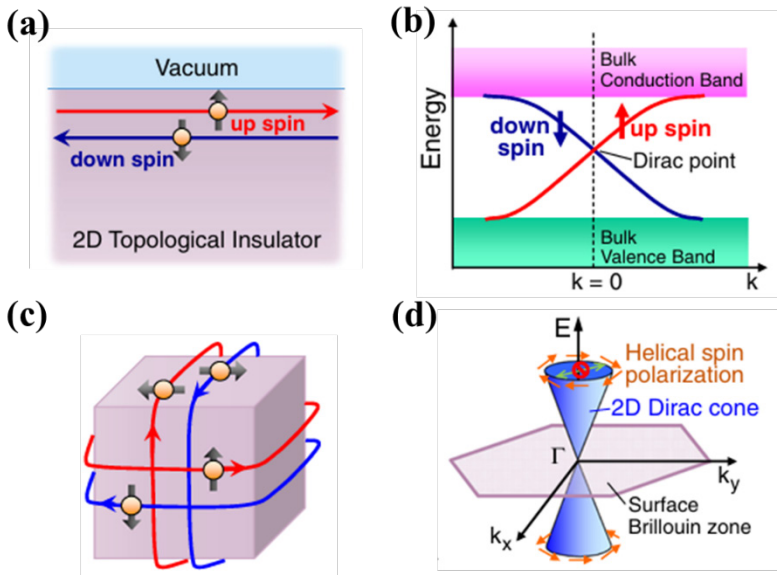

Fig. 1.2.1.2 Edge and surface states of topological insulators with Dirac dispersions. (a) Schematic real-space picture of the 1D helical edge state of a 2D TI. (b) Energy dispersion of the spin non-degenerate edge state of a 2D TI forming a 1D Dirac cone. (c) Schematic real-space picture of the 2D helical surface state of a 3D TI. (d) Energy dispersion of the spin non-degenerate surface state of a 3D TI forming a 2D Dirac cone; due to the helical spin polarization, back scattering from k to -k is prohibited [28]. Reprinted with permission from Journal of the Physical Society of Japan.

1-2-2 Optical characteristics of TI

TI is expected to absorb a weak light such as THz wave because of its surface states. The THz photodetector using TI is investigated theoretically. In one study, optical response of TI has been calculated in the range of 0- 0.3 eV (Fig.1.2.2.1) [29].

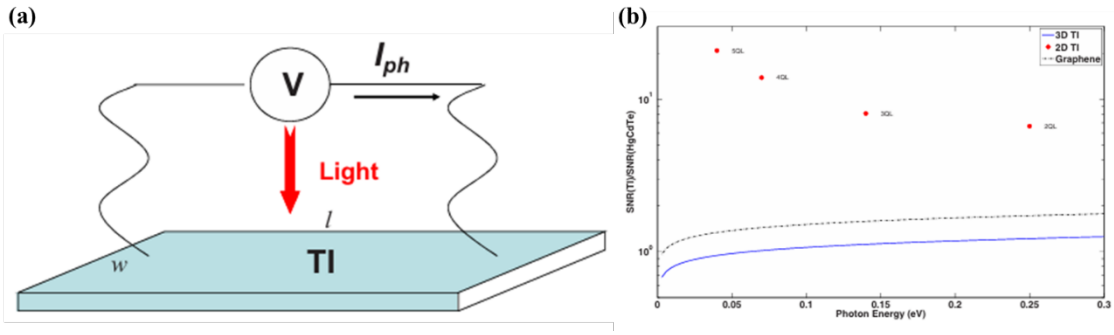

Fig. 1.2.2.1 (a) Schematic of a typical photoresistor using TI. (b) SNR of 3D TI (blue line), 2D TI (red dots), graphene (dotted line) [29]. Reprinted with permission from Physical Review B.

For Bi_2Se_3, optical absorption correlated with its surface band has been observed (Fig. 1.2.2.2 (a)) [30]. In this study, optical transition between the surface states is discussed, as the parallel characteristic of the two surface bands leads to strong absorption (Fig. 1.2.2.2 (b)).

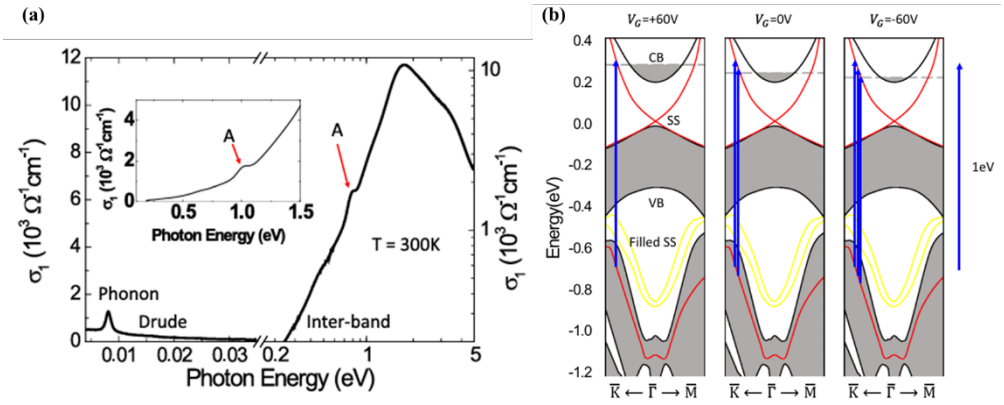

Fig. 1.2.2.2 (a) Optical conductivity of Bi_2Se_3 thin film (d=50 QL). (b) Schematic band structure and possible origin of absorption peak [30]. Reprinted with permission from Physical Review B.

1-2-3 Thermoelectric characteristics of TI

TI is known not only for its unique spintronic characteristics, but also for its significant thermoelectric characteristics, which also comes from the unique energy band structure. Schematics of Density of states (DOS) of an ideal TI are shown in Fig. 1.2.3.1 [31,32]. Using the DOS, the thermoelectric parameters have been calculated (Fig. 1.2.3.2) [33]. It can be seen that TI has a large Seebeck coefficient (*S*) and a large figure of merit (*ZT*).

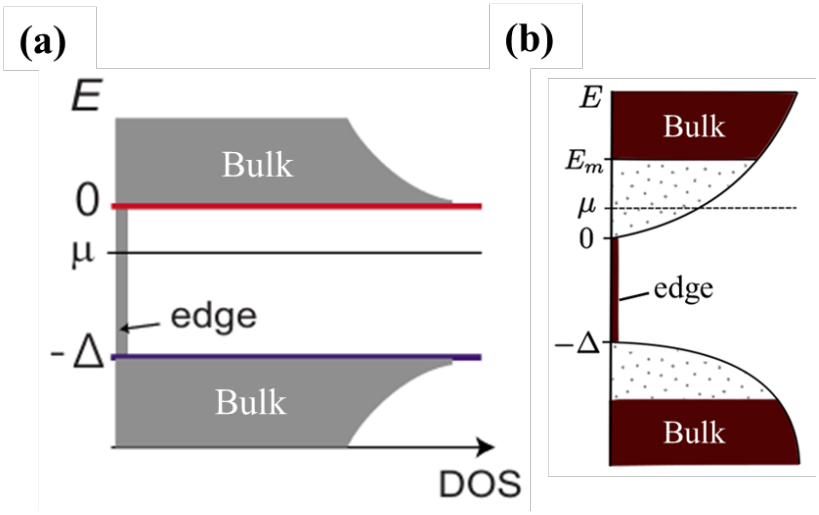

Fig. 1.2.3.1 DOS of ideal (a) 2D TI [31] and (b) 3D TI [32]. Reprinted with permission from Physical Review B and Applied Physics Letters, respectively.

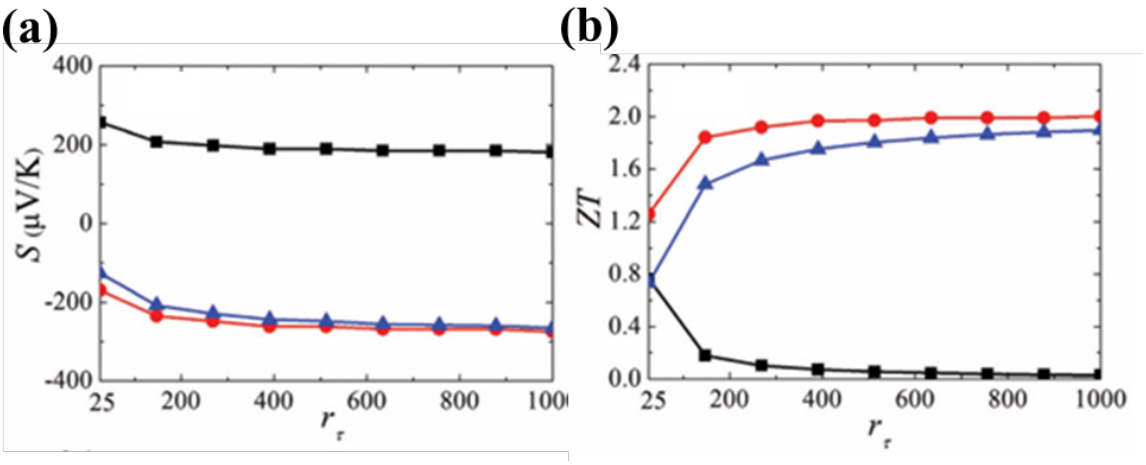

Fig. 1.2.3.2 (a) Seebeck coefficient *S*, (b) figure of merit *ZT* of the p-type 3-QL Bi_2Te_3 film, as a function of the relaxation time ratio γ_τ [33]. Reprinted with permission from Nanoscale.

1-2-4 IR detector of TI

TI has surface states and thus absorption of low energy photons is expected owing to its zero gap characteristics. It has been reported of PVE IR detector utilizing heterojunctions

of Bi_2Se_3 [34] (Fig.1.2.4.1) and Bi_2Te_3 [35] (Fig. 1.2.4.2) on Si. In both detectors, the surface states of TI are considered to be effectively used.

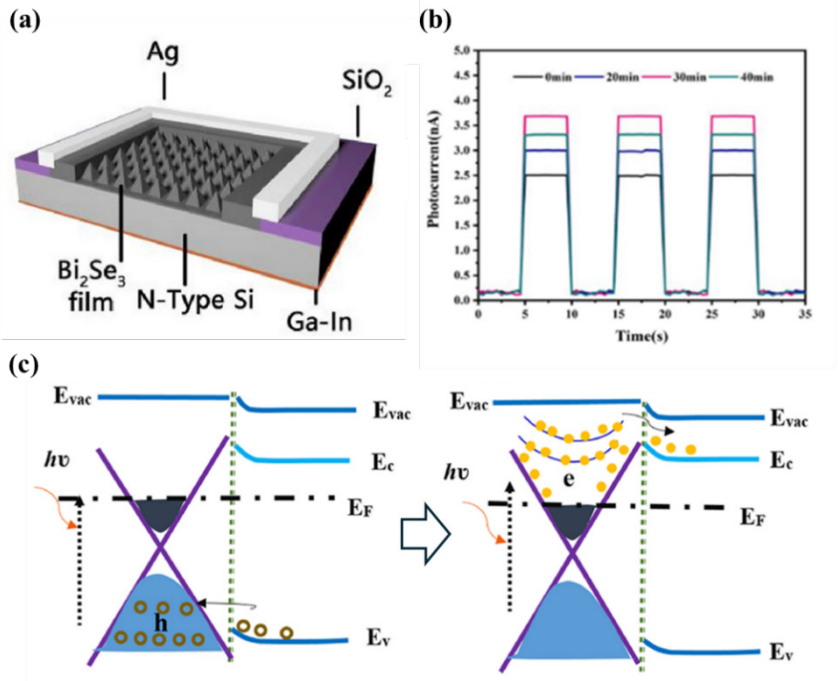

Fig. 1.2.4.1 Schematic diagram of a Bi_2Se_3-Si heterojunction photodetector. (b) Photoresponse of the detector. (c) Schematic diagram of microscopic mechanisms of photocurrent generation for the photodetector [34]. Reprinted with permission from Optical Materials.

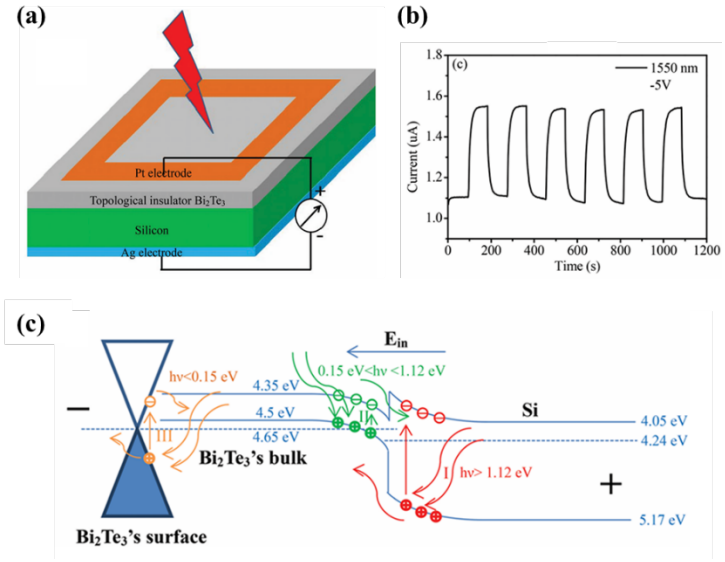

Fig. 1.2.4.2 (a) Schematic diagram of a Bi_2Te_3-Si heterojunction photodetector. (b) Photoresponse of the detector. (c) Schematic diagram of microscopic mechanisms of photocurrent generation for the photodetector [35]. Reprinted with permission from Nanoscale.

1-3 Motivation and thesis outline

As shown in chapter 1-1, very narrow bandgap semiconductors, such as HgCdTe, have traditionally been used as a MIR-absorbing material. However, it is often costly and time-consuming to grow epitaxial thin films of HgCdTe on single-crystalline substrates using precise growth techniques such as liquid-phase epitaxy or molecular beam epitaxy (MBE). There is a restriction of substrate material on which a film of HgCdTe semiconductor can be grown epitaxially. In contrast, there are TI-based photodetectors using PVE with high sensitivity and broad operational wavelengths, such as heterojunctions of Bi_2Te_3 and Bi_2Se_3 with semiconductors such as Si and Ge, as shown in chapter 1-2. Among these TIs, BiSb is particularly promising, as it has the smallest bulk bandgap of only 20 meV, making it suitable for MIR detection.

For the mechanism of detection, as shown in chapter 1-1, the thermal detector has a potential to be a useful infrared detector operating at room temperature, if speed and sensitivity are improved. As a PTE IR detection, recently, a camera with an array of CNT-based PTE detectors deposited on a flexible substrate has been demonstrated [36], which showcases the potential of the technology. However, CNT-based PTE detectors require solution-based processes [37], which may limit the spatial resolution and the size of the substrate. In contrast, BiSb can be deposited by magnetron sputtering, an industry-friendly dry process. Thus, BiSb is promising for PVE devices with high spatial resolution and low fabrication cost.

In the next chapter (chapter 2), we introduce the spintronic and thermoelectric characteristics of BiSb to show the possibility of BiSb as a PTE detector's material.

References

[1] "Extending opportunities," Nature Photon, **6,** 407 (2012).

[2] A. Rogalski, and F. Sizov, "Terahertz detectors and focal plane arrays," Opto-Electronics Review, **19,** 346-404 (2011).

[3] A. Rogalski, "Infrared detectors: an overview", Infrared Physics & Technology, **43,** 187-210 (2002).

[4] X. Lu, L. Sun, P. Jiang, *et al*., "Progress of Photodetectors Based on the Photothermoelectric Effect," Advanced Materials, **31,** 1902044 (2019).

[5] Z. Bao, Y. Wang, K. Zhang, *et al*., "Topological materials-based photodetectors from the infrared to terahertz range," Journal of Semiconductors, **46,** 081401 (2025).

[6] A. Rogalski, "HgCdTe infrared detector material: history, status and outlook," Reports on Progress of Physics, **68,** 2267 (2005).

[7] M. Yang, H. Zhou, J. Wang, "Topological insulators photodetectors; Preparation,

advances and application challenges," Materials Today Communications, **33,** 104190 (2022).

[8] A. Rogalski, “Progress in performance development of room temperature direct terahertz detectors,” Journal of Infrared, Millimeter, and Terahertz Waves, **43,** 709–727 (2022).

[9] C. Bai, G. Wu, J. Yang, *et al*., “2D materials-based photodetectors combined with ferroelectrics,” Nanotechnology, **35,** 352001 (2024).

[10] L. K. Li, Y. J. Yu, G. J. Ye, "Black phosphorus field-effect transistors," Nature Nanotechnology, **9,** 372 (2014).

[11] Q. Guo, A. Pospischil, M. Bhuiyan, *et al*., "Black Phosphorus Mid-Infrared Photodetectors with High Gain," Nano Letters, **16,** 4648 (2016).

[12] M. Engel, M. Steiner, P. Avouris, "Black Phosphorus Photodetector for Multispectral, High-Resolution Imaging," Nano Letters, **14,** 6414 (2014).

[13] H. Yuan, X. Liu, F. Afshinmanesh, *et al*., "Polarization-sensitive broadband photodetector using a black phosphorus vertical p–n junction," Nature Nanotechnology, **10,** 707 (2015).

[14] L. Viti, A. Politano, K. Zhang, *et al*., "Thermoelectric terahertz photodetectors based on selenium-doped black phosphorus flakes," Nanoscale, **11,** 1995 (2019).

[15] K. S. Novoselov, A. K. Geim, S. V. Morozov, *et al*., "Electric Field Effect in Atomically Thin Carbon Films," Science, **306,** 666 (2004).

[16] F. H. L. Koppens, T. Mueller, P. Avouris, *et al*., "Photodetectors based on graphene, other two-dimensional materials and hybrid systems," Nature Nanotechnology, **9,** 780 (2014).

[17] W. W. Cai, A. L. Moore, Y. W. Zhu, *et al*., "Thermal Transport in Suspended and Supported Monolayer Graphene Grown by Chemical Vapor Deposition," Nano Letters, **10,** 1645 (2010).

[18] P. Wei, W. Z. Bao, Y. Pu, *et al*., "Anomalous Thermoelectric Transport of Dirac Particles in Graphene," Physical Review Letters, **102,** 166808 (2009).

[19] K. J. Tielrooij, L. Piatkowski, M. Massicotte, "Generation of photovoltage in graphene on a femtosecond timescale through efficient carrier heating," Nature Nanotechnology, **10,** 437 (2015).

[20] J. Yan, M. H. Kim, J. A. Elle, *et al*., "Dual-gated bilayer graphene hot-electron bolometer," Nature Nanotechnology, **7,** 472 (2012).

[21] D. M. Basko, I. L. Aleiner, "Interplay of Coulomb and electron-phonon interactions in graphene," Physical Review B, **77,** 041409 (2008).

[22] X. Cai, A. B. Sushkov, R. J. Suess, *et al*., "Sensitive room-temperature terahertz detection via the photothermoelectric effect in graphene," Nature Nanotechnology, **9,** 814 (2014).

[23] M. Zhang, J.T.W. Yeow, "A flexible, scalable, and self-powered mid-infrared detector based on transparent PEDOT: PSS/graphene composite," Carbon, **156,** 339-345 (2020).

[24] K. Li, D. Suzuki, and Y. Kawano, "Series Photothermoelectric Coupling Between Two Composite Materials for a Freely Attachable Broadband Imaging Sheet," Advanced Photonics Research, **2,** 2000095 (2021).

[25] K. Li, T. Araki, R. Utaki, *et al*., "Stretchable broadband photo-sensor sheets for nonsampling, source-free, and label-free chemical monitoring by simple deformable wrapping," Science Advances, **8,** eabm4349 (2022).

[26] G. P. Szakmany, A. O. Orlov, G. H. Bernstein, *et al*., "Novel Nanoscale Single-Metal Polarization-Sensitive Infrared Detectors," in *IEEE Transactions on Nanotechnology*, **14,** 379 (2015).

[27] H. Zhang, C.-X. Liu, X.-L. Qi, *et al*., "Topological insulators in Bi_2Se_3, Bi_2Te_3 and Sb_2Te_3 with a single Dirac cone on the surface," Nature Physics, **5,** 438–442 (2009).

[28] Y. Ando, "Topological Insulator Materials, "Journal of the Physical Society of Japan, **82,** 102001 (2013).

[29] X. Zhang, J. Wang, and S.-C. Zhang, "Topological insulators for high-performance terahertz to infrared applications," Physical Review B, **28,** 245107 (2010).

[30] J. Jeon, K. Yu, J. Kim, *et al*., "Observation of optical absorption correlated with surface state of topological insulator," Physical Review B, **100,** 195110 (2019).

[31] R. Takahashi, S. Murakami, "Thermoelectric transport in perfectly conducting channels in quantum spin Hall systems," Physical Review B, **81**, 161302 (2010).

[32] O. A. Tretiakov, A. Abanov, S. Murakami, and et al., "Large thermoelectric figure of merit for three-dimensional topological Anderson insulators via line dislocation engineering," Applied Physics Letters, **97**, 073108 (2010).

[33] J. Liang, L. Cheng, J. Zhang, *et al*., “Maximizing the thermoelectric performance of topological insulator Bi_2Te_3 films in the few-quintuple layer regime,” Nanoscale, **8**, 8855–8862 (2016).

[34] X. Hong, J. Shen, X. Tang, *et al*., "High-performance broadband photodetector with in-situ-grown Bi2Se3 film on micropyramidal Si substrate," Optical Materials, **117,**111118 (2021).

[35] J. Yao, J. Shao, Y. Wang, *et al*., "Ultra-broadband and high response of the Bi2Te3–Si heterojunction and its application as a photodetector at room temperature in harsh working environments," Nanoscale, **7,** 12535 (2015).

[36] L. Takai, Y. Kinoshita, N. Takahashi, *et al*., “n-type carbon nanotube inks for high-yield printing of ultrabroadband soft photo-imager thin sheets,” FlexMat, **2,** 115(2025).

[37] M. Yamamoto, D. Sakai, Y. Matsuzaki, *et al*., “Mechanically alignable and all-dispenser-printable device design platform for carbon nanotube-based soft-deformable photo-thermoelectric broadband imager sheets,” npj Flex Electron, **9,** 42 (2025).

Chapter 2. Fundamental properties of BiSb

2-1 Topological insulator characteristics

BiSb is known as the first discovered 3D TI [1].The surface band of BiSb changes by Sb concentration (Fig. 2.1.1). As shown in Fig. 2.1.2, pure Bi is a semimetal and there is no band inversion. When Sb concentration reaches about 4%, band inversion occurs. Importantly, when Sb concentration is about 7%-22%, BiSb functions as a TI.

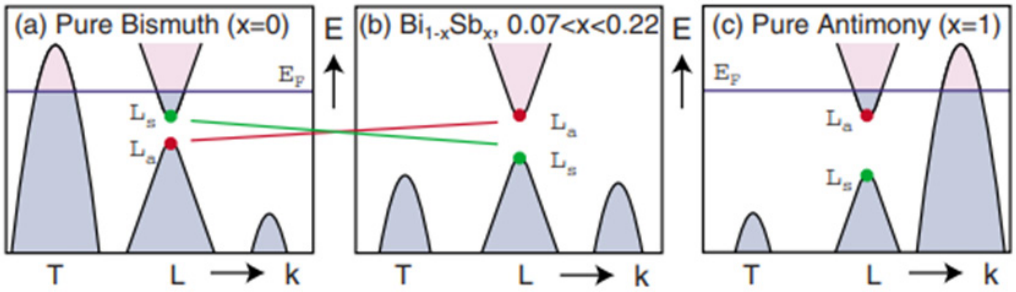

Fig. 2.1.1 Schematic representation of the band structure of $Bi_{1-x}Sb_x$, which evolves from semimetallic behavior for x<0.07 to semiconducting behavior for 0.07<x<0.22 and back to semimatallic behavior for x>0.18. The conduction and valence bands $L_{S,a}$ invert at x~0.04 [2]. Reprinted with permission from Reviews of Modern Physics.

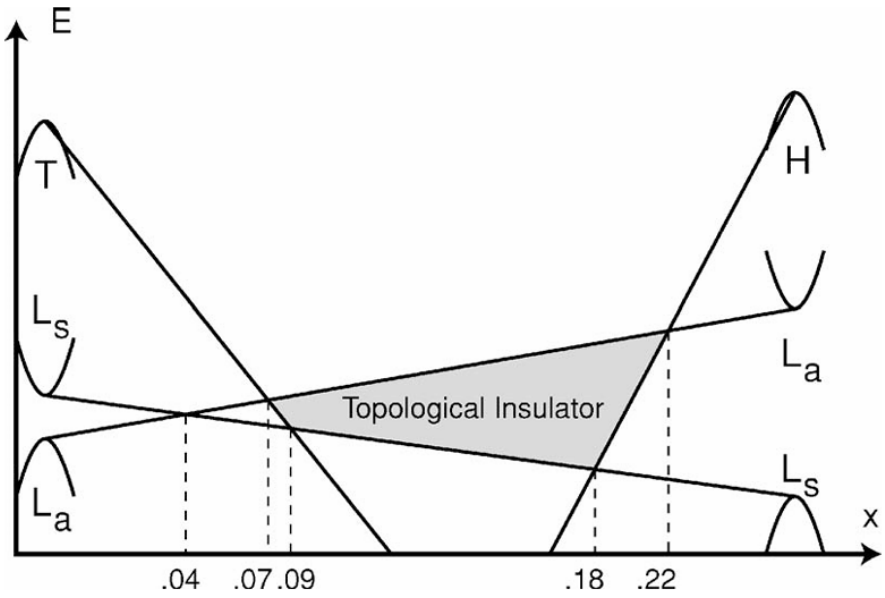

Fig. 2.1.2 Schematic representation of band energy evolution of $Bi_{1-x}Sb_x$ as a function of x [3]. Reprinted with permission from Physical Review B.

In addition, BiSb is well-known for its complex surface states among TIs [1]. As shown in Fig. 2.1.3, the two curves of the topological surface bands can change with Sb concentration.

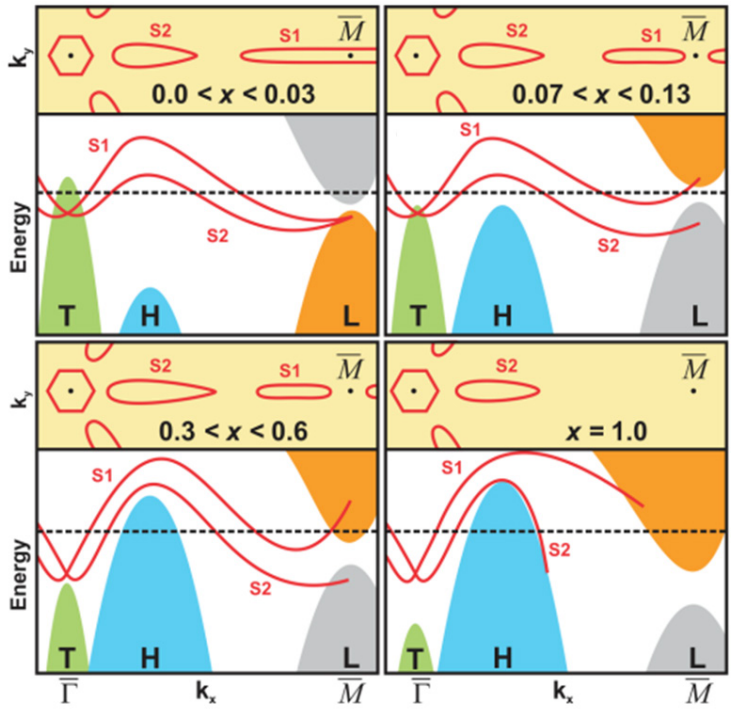

Fig. 2.1.3 Schematic of surface band structure of $Bi_{1-x}Sb_x$ (111) with different Sb concentration [4]. Reprinted with permission from Physical Review B.

2-2 Thermoelectric properties

As shown in Chapter 1, TIs have good thermoelectric parameters. BiSb is not an exception. As shown in Fig. 2.2.1 (a), it is reported that BiSb has a Seebeck coefficient raging from about -50 to 150 μVK^{-1} at different thicknesses [5]. Furthermore, the dependence of the Seebeck coefficient on magnetic field has been observed (Fig.2.2.1 (b))[6].

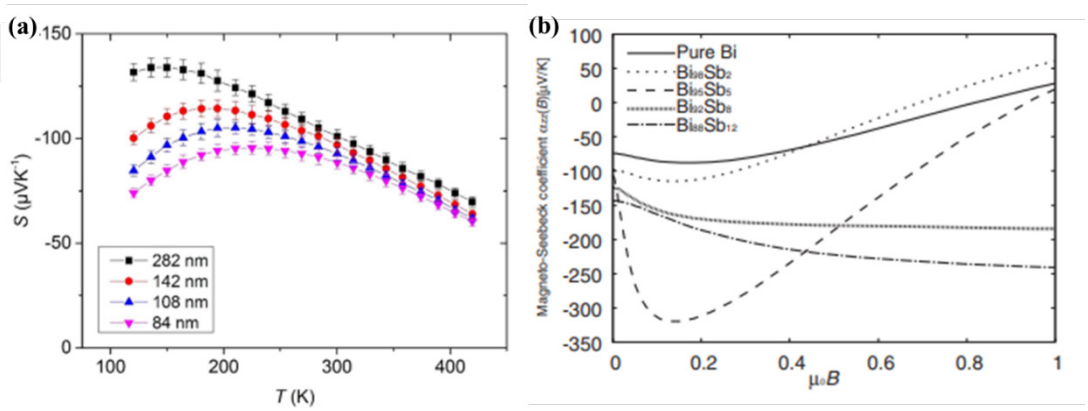

Fig. 2.2.1 (a) Measured Seebeck coefficient S of the $Bi_{87}Sb_{13}$ nanofilms in the temperature range from 110 K up to 420 K [5]. Reprinted with permission from Semiconductor Science and Technology. (b) Dependence of the Seebeck coefficient on the magnetic field for Bi, $Bi_{98}Sb_2$, $Bi_{95}Sb_5$, $Bi_{92}Sb_8$, and $Bi_{88}Sb_{12}$ [6]. Reprinted with permission from Journal of Applied Physics.

The figure of merit (Z) of BiSb is about 1 to 7 $\times 10^{-3}$ K^{-1}, and it changes by magnetic field (Fig.2.2.2) [7].

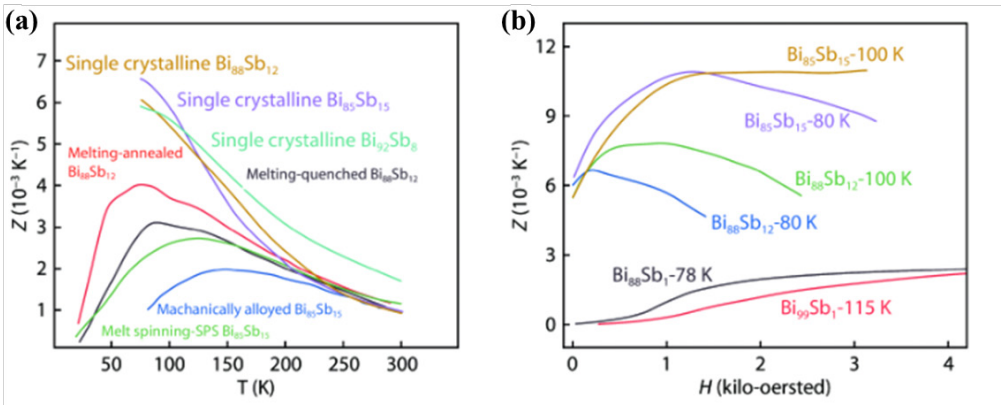

Fig. 2.2.2 (a) Temperature dependences of figure of merit Z for BiSb samples prepared by different methods. (b) Dependence upon magnetic field of the thermoelectric figure of merit of some typical BiSb [7]. Reprinted with permission from Materials Lab.

2-3 Previous spintronic and photonic applications

BiSb film can be fabricated not only by MBE [8], but also by magnetron sputtering [9] ((Fig. 2.3.1)), which allows mass production with low cost on large substrates.

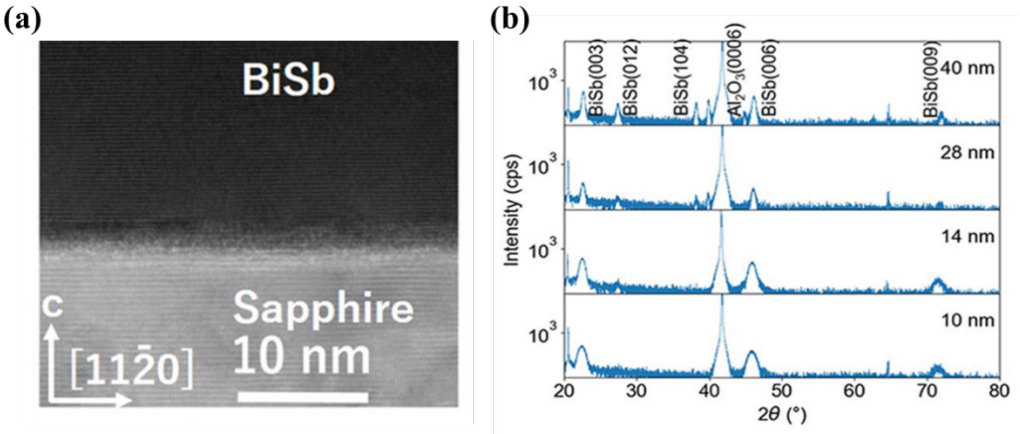

Fig. 2.3.1 (a) TEM image of BiSb on sapphire. (b) XRR spectra of sputtered BiSb on sapphire [9]. Reprinted with permission from Japanese Journal of Applied Physics.

Notably, BiSb is an exceptional promising spintronic material with a giant spin Hall angle (SHA). Ultralow power spin–orbit torque switching for MRAM applications has been investigated [10,11]. As shown in Chapter 1, THz or IR detector has been investigated theoretically and experimentally for TIs. THz BiSb detector has been reported and THz

response of about 150 μV has been obtained (Fig. 2.3.2, 2.3.3) [12,エラー! ブックマークが定義されていません。].

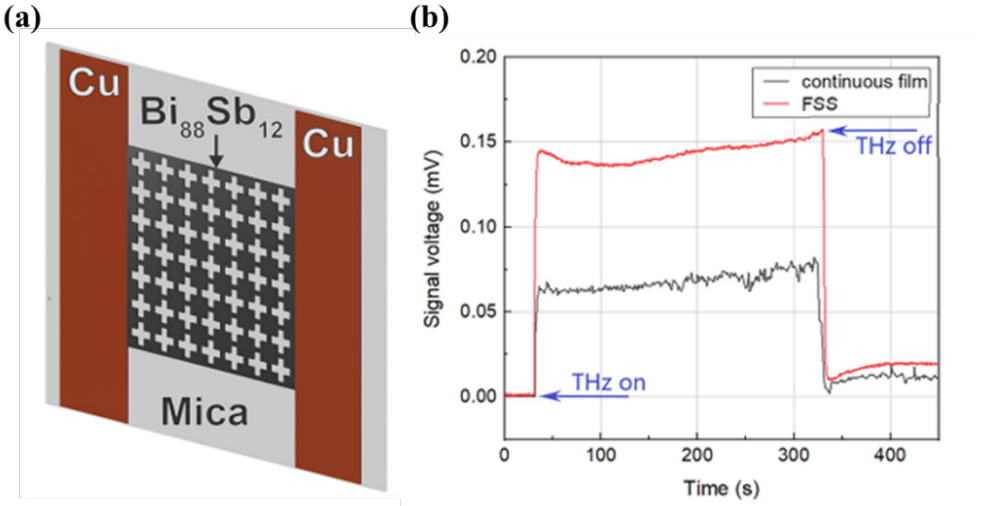

Fig. 2.3.2 (a) Schematic of THz BiSb detector. (b) THz response of the detector [12]. Reprinted with permission from Applied Physics Letters.

2-4 Prospect for infrared detector using BiSb

As shown in chapter 1 and 2, BiSb has the smallest bulk band gap among Bi-based TIs and a large Seebeck coefficient. Furthermore, it can be deposited using the industry-friendly magnetron sputtering method, which is purely physical, industry-friendly dry process for low cost fabrication. Consequently, we expect that BiSb can be a good material for use in IR PTE detectors. In this thesis, we first measure the infrared optical constants (n, κ) of topological insulator BiSb thin films using the reflectance-

transmittance method in the infrared (IR) region and use them to calculate the absorption of BiSb. Then, we will demonstrate proof-of-concept PTE detectors using BiSb.

References

[1] Y. Ando, "Topological Insulator Materials, "Journal of the Physical Society of Japan, **82**, 102001 (2013).

[2] M. Z. Hasan, C. L. Kane, "*Colloquium*: Topological insulators," Reviews of Modern Physics, **82**, 3045 (2010).

[3] L. Fu and C. L. Kane, "Topological insulators with inversion symmetry," Physical Review B, **76**, 045302(2007).

[4] H. M. Benia, C. Straβer, K. Kern, *et al*., "Surface band structure of $Bi_{1-x}Sb_x$ (111)," Physical Review B, **91**, 161406 (2015).

[5] V. Linseis, F Völklein, H Reith, *et al*., "Thickness and temperature dependent thermoelectric properties of Bi87Sb13 nanofilms measured with a novel measurement platform,"Semiconductor Science and Technology, **33**, 8 (2018).

[6] T. Teramoto, T. Komine, S. Yamamoto, *et al*., "Influence of the band structure of BiSb alloy on the magneto-Seebeck coefficient," Journal of Applied Physics, **104**, 053714 (2008).

[7] H. Su, H. Zhang, M. Zhou, "Recent progress of cryogenic thermoelectric materials," Materials Lab, **2**, 230015 (2003).

[8] Y. Ueda, N. H. D. Khang, K. Yao, *et al*., "Epitaxial growth and characterization of $Bi_{1-x}Sb_x$ spin Hall thin films on GaAs(111) substrates," Applied Physics Letters, **110**, 062401 (2017).

[9] T. Fan, M. Tobah, T. Shirokura, *et al*., "Crystal growth and characterization of topological insulator BiSb thin films by sputtering deposition on sapphire substrates," Japanese Journal of Applied Physics, **59**, 063001 (2020).

[10] N. H. D. Khang, Y. Ueda, P. N. Hai, "A conductive topological insulator with large

spin Hall effect for ultralow power spin–orbit torque switching," Nature Materials, **17**, 808–813 (2018).

[11] T. Fan, N. H. D. Khang, S. Nakano, et al., "Ultra high efficient spin orbit torque magnetization switching in fully sputtered topological insulator and ferromagnet multilayers," Scientific Reports, **12**, 2998 (2022).

[12] M. Khodzitsky, A. Tukmakova, D. Zykov, *et al*., "THz room-temperature detector based on thermoelectric frequency-selective surface fabricated from Bi88Sb12 thin film," Applied Physics Letters, **119**, 164101 (2021).

Chapter 3. Experimental methods

3-1 Sample preparation

3-1-1 Deposition of BiSb thin films

We deposited BiSb thin films with the Sb composition of 0%, 10% and 15% on Si substrates for RT measurement and on Au-coated glass substrates for R measurement. Here, the BiSb thin films were deposited using magnetron sputtering, while the Au film was deposited using electron beam evaporation. We deposited Au film thick enough for nearly 100% reflection of infrared light. 1000 μm-thick Si was chosen as the substrate because of its relatively flat transmission spectrum with transmittance of about 50% over a wide range of infrared wavelengths from 0.1 eV to 1 eV (photon energy).

3-1-2 Photothermoelectric device fabrication

We prepared samples as shown in Fig. 3.1.2.1. We prepared ribbon-shaped $Bi_{90}Sb_{10}$ thin films of l × w × t (l: length=4 mm, 10 mm,16 mm, w: width=0.25 mm, 0.5 mm, 2 mm, t: thickness =80 nm) by magnetron sputtering and lift-off technique on sapphire substrates. Pt/Ta film was then formed onto the edge of the BiSb film as electrodes. For fabrication of $Bi_{90}Sb_{10}$ thin film on a flexible Kapton substrate, we first attached the Kapton substrate to a rigid substrate, and then use it for optical lithography, BiSb deposition, and lift-off. After that, the Kapton substrate with BiSb PTE detector was peeled off from the rigid substrate for PTE measurement. We measured the thickness of the $Bi_{90}Sb_{10}$ film by using X-ray reflection (XRR) spectroscopy.

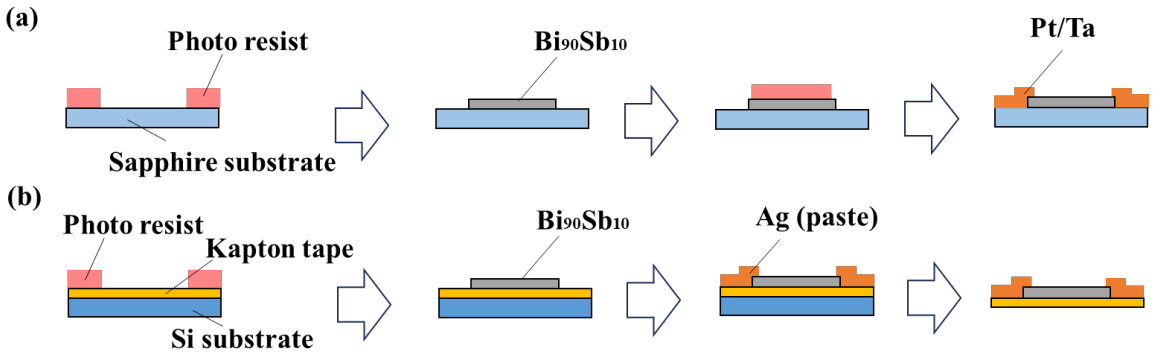

Fig. 3.1.2.1. Illustration of preparing samples. (a) Samples of BiSb/sapphire were fabricated via lift-off process. (b) Sample of BiSb/Kapton was fabricated via lift-off process, too. Si substrate was used to fix the Kapton tape and peeled off at the end.

3-2 Measurement

3-2-1 Thickness evaluation

The thicknesses of Si substrates were measured by a digimatic indicator, which shows a considerable variation in thickness of a few 10 μm (Fig. 3.2.1.1). The thicknesses of BiSb thin films (< 50 nm) on Si were measured by using the X-ray reflectivity method (Fig. 3.2.1.2), while those of thicker BiSb films (≧ 90 nm) on Au were measured by X-ray fluorescence method.

Fig. 3.2.1.1 Illustration of the measurement using the digimatic indicator [1].

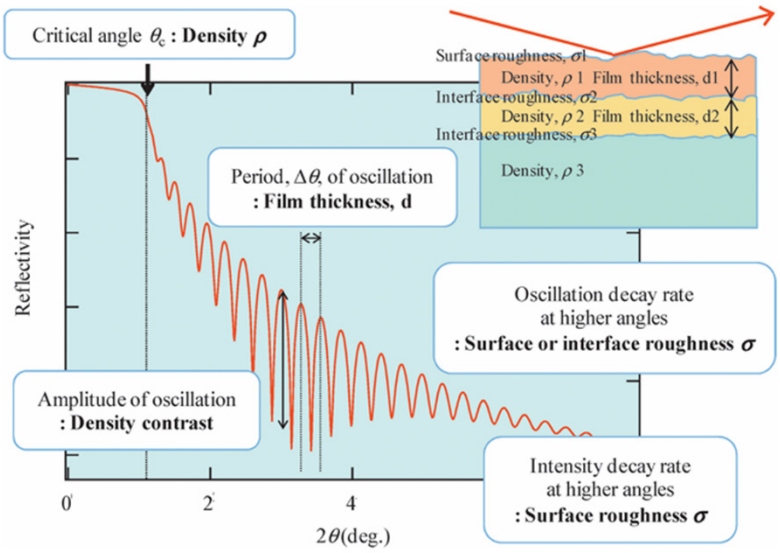

Fig. 3.2.1.2 XRR explanation [2].

Representative measured XRR and XRF spectra of BiSb are shown in Figs. 3.2.1.3 and 3.2.1.4, respectively.

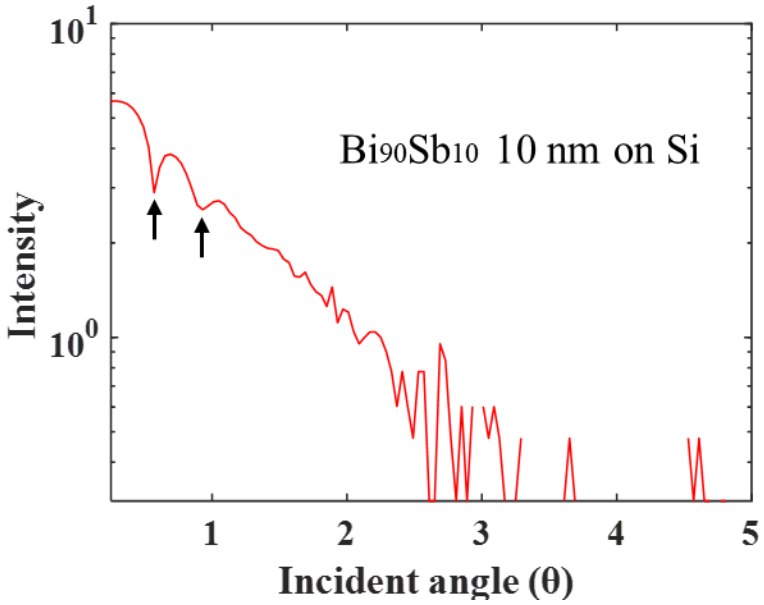

Fig. 3.2.1.3 XRR spectrum of 10 nm $Bi_{90}Sb_{10}$ on Si.

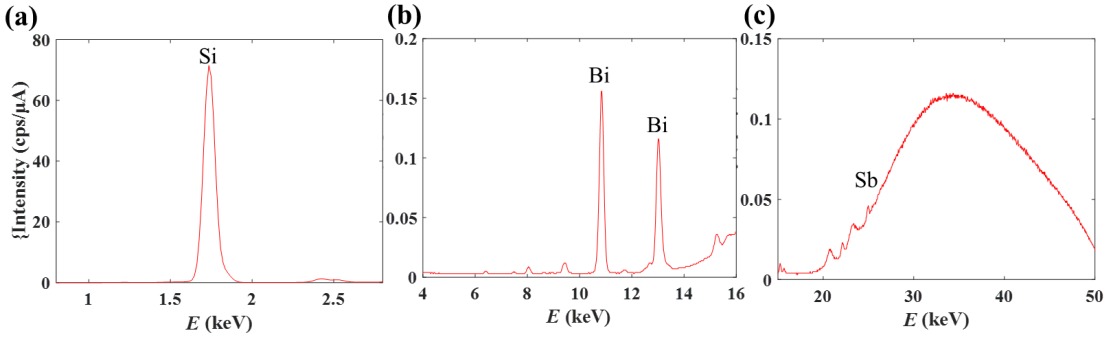

Fig.3.2.1.4 XRF spectrum of 10 nm $Bi_{90}Sb_{10}$ 10nm on Si.

3-2-2 Evaluation of optical properties by the RT method

We describe the RT method for evaluation of the optical properties of BiSb [3]. We consider a wave incident (wavelength: λ) from a medium 0 (air) to a medium 1 (Bi, $Bi_{90}Sb_{10}$, $Bi_{85}Sb_{15}$), a medium 2 (Si), a medium 3 (air), as shown in Figure 3.2.2.1. Refractive indices of medium 0, 1, 2, 3 are $n_0(=1), n_1 = n_1 - i\kappa_1, n_2 = n_2 - i\kappa, n_3(=1)$, respectively. d_1, d_2 are the thickness of a medium 1 (Bi, $Bi_{90}Sb_{10}$, $Bi_{85}Sb_{15}$), medium

2 (Si), respectively. Incidence angles in each medium are $\theta_0, \theta_1, \theta_2, \theta_3$ and these are related via Snell's law: $n_0 \sin\theta_0 = n_1 \sin\theta_1 = n_2 \sin\theta_2 = n_3 \sin\theta_3$. The amplitude of the electric vector of a light propagating forward and backward in medium j is E_j^+, E_j^-, respectively $(j = 0, 1, 2)$. r_{j+1}, t_{j+1} are reflection coefficient and transmission coefficient, respectively, of a wave propagating from a medium j to a medium $j+1$ $(j = 0, 1, 2)$. The equations of the reflection and transmission coefficients are

$$r_{j+1} = \frac{n_{j+1}\cos\theta_j - n_j\cos\theta_{j+1}}{n_{j+1}\cos\theta_j + n_j\cos\theta_{j+1}} \text{ (p polarization),} \tag{3.1}$$

$$r_{j+1} = \frac{n_{j+1}\cos\theta_{j+1} - n_j\cos\theta_j}{n_{j+1}\cos\theta_{j+1} + n_j\cos\theta_j} \text{ (s polarization).} \tag{3.2}$$

For transmission coefficient, we assumed normal incidence, so we use an equation of no incident angle shown below.

$$t_{j+1} = \frac{2n_j}{n_j + n_{j+1}} \text{(normal incidence).} \tag{3.3}$$

The phase shift in each medium is

$$\Delta 1 = \frac{2\pi n_1 \cos\theta_1 d_1}{\lambda} \text{ (medium 1),} \tag{3.4}$$

$$\Delta 2 = \frac{2\pi n_2 \cos\theta_2 (d_1 + d_2)}{\lambda} \text{ (medium 2).} \tag{3.5}$$

The relation of E_j^+, E_j^- can be expressed using

$$\begin{bmatrix} E_0^+ \\ E_0^- \end{bmatrix} = \frac{C_1 C_2 C_3}{t_1 t_2 t_3} \begin{bmatrix} E_3^+ \\ E_3^- \end{bmatrix}. \tag{3.6}$$

Here,

$$C_1 = \begin{bmatrix} 1 & r_1 \\ r_1 & 1 \end{bmatrix}, \tag{3.7}$$

$$C_2 = \begin{bmatrix} e^{i\Delta 1} & r_2 e^{i\Delta 1} \\ r_2 e^{-i\Delta 1} & e^{-i\Delta 1} \end{bmatrix}, \tag{3.8}$$

$$C_3 = \begin{bmatrix} e^{i\Delta 2} & r_3 e^{i\Delta 2} \\ r_3 e^{-i\Delta 2} & e^{-i\Delta 2} \end{bmatrix}. \tag{3.9}$$

Defining $C_1C_2C_3 \equiv \begin{bmatrix} a & b \\ c & d \end{bmatrix}$ and substituting $E_3^- = 0$, we can get

$$\begin{bmatrix} E_0^+ \\ E_0^- \end{bmatrix} = \frac{1}{t_1 t_2 t_3} \begin{bmatrix} a & b \\ c & d \end{bmatrix} \begin{bmatrix} E_3^+ \\ 0 \end{bmatrix}. \tag{3.10}$$

Then reflectance and transmittance are expressed as below:

$$R = \left(\frac{E_0^-}{E_0^+}\right)\left(\frac{E_0^-}{E_0^+}\right)^* = \frac{cc^*}{aa^*}, \tag{3.11}$$

$$T = \frac{n_3}{n_0}\left(\frac{E_3^+}{E_0^+}\right)\left(\frac{E_3^+}{E_0^+}\right)^* = \frac{n_3}{n_0}\frac{(t_1 t_2 t_3)(t_1^* t_2^* t_3^*)}{aa^*} \ , \tag{3.12}$$

For R, we consider polarization,

$$R = \frac{R_s + R_p}{2} \ . \tag{3.13}$$

In addition, we consider non-uniform thicknesses of the Si substrates (1000-1050 μm, 0.01 μm step, 5001 different thicknesses. As it is reported that non-uniformity of thickness induces the spectral change, where the maxima decrease and minima increase [4,5] (Fig. 3.2.2.2), we calculate the averaged reflectance and transmittance using the following equations.

$$R_d = \frac{1}{2\Delta d}\int_{\bar{d}-\Delta d}^{\bar{d}+\Delta d} R(d)\mathrm{d}d, \tag{3.14}$$

$$T_d = \frac{1}{2\Delta d}\int_{\bar{d}-\Delta d}^{\bar{d}+\Delta d} T(d)\mathrm{d}d, \tag{3.15}$$

where Δd=50 μm, $\mathrm{d}d$=0.01 μm.

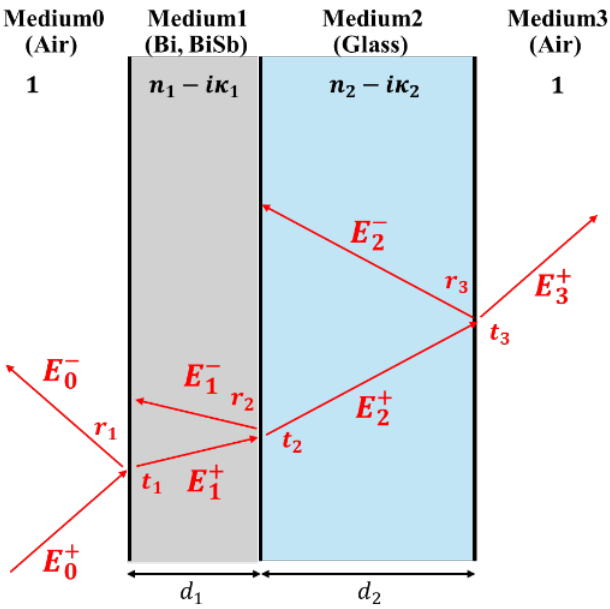

Fig. 3.2.2.1 Model of a wave incident from air to 2-layers medium. Red arrows are transmitted or reflected light on the interfaces of mediums.

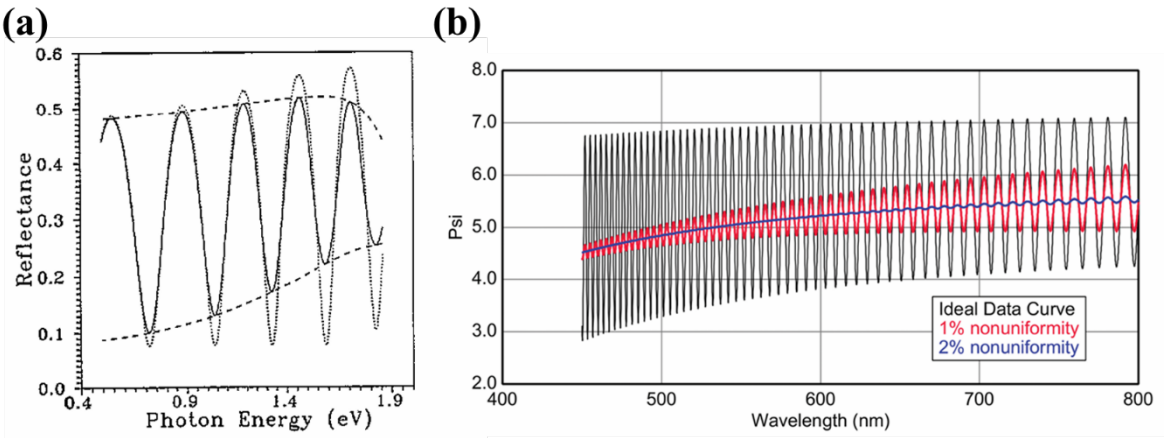

Fig. 3.2.2.2 (a) Reflection spectrum for a typical a-Si:H thin film with uniform thickness d = 0.6 μm (dotted curve) with thickness variation Δd = 0.03 μm (full curve), and the envelopes (broken curves) [4]. Reprinted with permission from Journal of Physics D: Applied Physics. (b) Simulated data sets of ellipsometry with 1% (red) and 2% (blue) thickness nonuniformity compared to the ideal curve (black) [5]. Reprinted with permission from Vacuum Technology & Coating.

3-2-3 Optical spectra measurement by FTIR

We describe the FTIR method for optical spectra measurements [6]. Fig.3.2.3.1 shows a schematic of FTIR measurement. We consider the electromagnetic wave traveling in the z direction (towards the beam splitter). The amplitude can be expressed as

$$E(z,\nu)d\nu = E_0(\nu)e^{i(\omega t - 2\pi\nu z)}d\nu \tag{3.16}$$

At the beam splitter, the beam is divided. By considering that each beam undergoes reflection and transmission, respectively, the recombined wave can be expressed as

$$E_{\mathrm{R}}[z_1, z_2, \nu]d\nu = rt\ \ E_0(\nu)\left[e^{i(\omega t - 2\pi\nu z_1)} + e^{i(\omega t - 2\pi z_2)}\right]d\nu \tag{3.17}$$

, where *r, t* are the reflection and transmission coefficient, respectively.

By definition, the intensity of the beam after the recombination for the fixed spectral range $d\nu$ is given as

$$\begin{aligned} I_{\mathrm{R}}(x) &= \int_0^\infty I(z_1, z_2, \nu)d\nu \\ &= \int_0^\infty E_{\mathrm{R}}(z_1, z_2, \nu)\ \ {E_{\mathrm{R}}}^*(z_1, z_2, \nu)d\nu \\ &= \int_0^\infty 2E_0^2(\nu)|rt|^2[1 + \cos\{2\pi(z_1 - z_2)\ \ \nu\}]d\nu \end{aligned} \tag{3.18}$$

The total intensity at any path difference $x = z_1 - z_2$ for the whole spectral range is calculated by the following equation

$$I_R(x) = 2|rt|^2\int_0^\infty E_0^2(\nu)d\nu + 2|rt|^2\int_0^\infty E_0^2(\nu)\cos(2\pi x\nu)d\nu \tag{3.19}$$

Performing the Fourier transform of (3.19), we can get

$$E_0^2(\nu) = \frac{1}{\pi|rt|^2}\int_0^\infty \left[I_{\mathrm{R}}(x) - \frac{1}{2}I_{\mathrm{R}}(0)\right]\cos(2\pi\nu x)\,dx, \tag{3.20}$$

where $I_R(x)$ is the flux associated at path difference *x*, $I_R(0)$ is the flux associated with coherent interference, and $I_{\mathrm{R}}(x) - \frac{1}{2}I_{\mathrm{R}}(0)$ is called the interferogram. In FTIR, firstly

the interferogram is obtained. Then, by Fourier transforming it, the power spectrum, transmittance spectrum, or reflectance spectrum are obtained. The spectrum $S(\nu)$, which is proportional to $E_0^2(\nu)$, can be given from (3.20) as

$$S(\nu) \propto E_0^2(\nu) = \text{constant} \int_0^{\infty} \left[I_{\mathrm{R}}(x) - \tfrac{1}{2} I_{\mathrm{R}}(0) \right] \cos(2\pi\nu x)\, dx \qquad (3.21)$$

For the monochromatic light, the spectrum $S(\nu)$ is given as

$$S(\nu) = \int_{-\infty}^{+\infty} \left[I_{\mathrm{R}}(x) - \tfrac{1}{2} I_{\mathrm{R}}(0) \right] e^{-i2\pi\nu x} dx. \qquad (3.22)$$

Thus, its corresponding interferogram is

$$I_{\mathrm{R}}(x) - \tfrac{1}{2} I_{\mathrm{R}}(0) = \int_{-\infty}^{\infty} S(\nu) e^{i2\pi\nu x} d\nu. \qquad (3.23)$$

For the frequency of ν_1, the spectrum $S(\nu)$ is

$$S(\nu_1) = \tfrac{1}{2} [\delta'(\nu - \nu_1) + \delta(\nu + \nu_1)], \qquad (3.24)$$

where $\delta'(\nu - \nu_1)$ and $\delta'(\nu - \nu_2)$ are the Dirac delta functions. From (3.23) and (3.24), we can get

$$\begin{aligned} I_{\mathrm{R}}(x) - \frac{1}{2} I_{\mathrm{R}}(0) &= \frac{1}{2} \int_{-\infty}^{\infty} [\delta'(\nu - \nu_1) + \delta(\nu + \nu_1)] e^{i2\pi\nu x} d\nu \\ &= \tfrac{1}{2} \int_{-\infty}^{\infty} [e^{i2\pi\nu_1} + e^{-i2\pi\nu_1}] d\nu. \end{aligned} \qquad (3.25)$$

Its corresponding spectrum is

$$S(\nu) = \int_{-\infty}^{\infty} 2\cos(2\pi\nu_1 x)\, e^{-i2\pi\nu x} dx. \qquad (3.26)$$

As the interferogram cannot be scanned to infinity, the practical equation (scan limit: $-L \sim +L$) is

$$\begin{aligned} S(\nu) &= \int_{-L}^{L} 2\cos(2\pi\nu_1 x)\, e^{-i2\pi\nu x} dx \\ &= \int_{-L}^{L} 2\cos(2\pi\nu_1 x)\, [\cos(2\pi\nu x) - i\sin(2\pi\nu x)] dx \end{aligned}$$

$$= \int_{-L}^{L} [\cos\{2\pi x(\nu_1 + \nu)\} + \cos\{2\pi x(\nu_1 - \nu)\}] dx$$

$$= 2L \left[\frac{\sin\{2\pi(\nu_1 + \nu)L\}}{2\pi(\nu_1 + \nu)L} + \frac{\sin\{2\pi(\nu_1 - \nu)L\}}{2\pi(\nu_1 - \nu)L} \right]$$

$$\cong 2L \left[\frac{\sin 2\pi(\nu_1 - \nu)L}{2\pi(\nu_1 - \nu)L} \right]$$

$$= 2L \ \text{sinc}(z), \tag{3.27}$$

where $z \equiv 2\pi(\nu_1 - \nu)L$. The spectrum of (3.27) is usually known as instrument lineshape function (ILS). In FTIR, the corrective procedure called the apodization is performed on this spectrum. There are several functions used for the apodization (apodization function) [7]. For example, when using the triangular function $1 - \frac{|x|}{L}$, the spectrum is corrected as

$$S(\nu) = \int_{-L}^{L} \left(1 - \frac{|x|}{L}\right) 2\cos(2\pi\nu_1 x)\, e^{-i2\pi\nu x} dx$$

$$= L \ sinc^2\left(\frac{z}{2}\right), \tag{3.28}$$

where $\pi(\nu_1 - \nu)L = \frac{z}{2}$.

In this research, we used the Happ-Genzel function $0.54 + 0.46\cos\left(\frac{\pi x}{L}\right)$ [7]. In this case, we can get

$$S(\nu) = \int_{-L}^{L} \left(0.54 + 0.46\cos\left(\frac{\pi x}{L}\right)\right) 2\cos(2\pi\nu_1 x)\, e^{-i2\pi\nu x} dx$$

$$= \left[\frac{0.54}{\pi(\nu_1 - \nu)} + \frac{0.46 * 4\pi(\nu_1 - \nu)L^2}{\pi^2 - \{2\pi(\nu_1 - \nu)L\}^2}\right] \sin\{2\pi(\nu_1 - \nu)L\} \tag{3.29}$$

As the word “apodization” means, the effect of the apodization function on the interferogram is to reduce the feet or sidelobes of the spectrum.

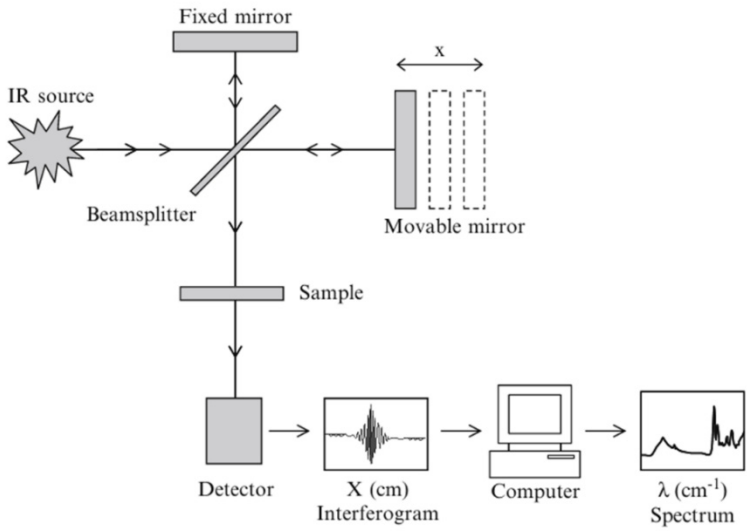

Fig. 3.2.3.1 Schematic of FTIR [8]. Reprinted with permission from Microbial Systems Biology: Methods in Molecular Biology.

Representative measured spectra (interferogram and its corresponding transmittance in NIR) are shown in Fig. 3.2.3.2.

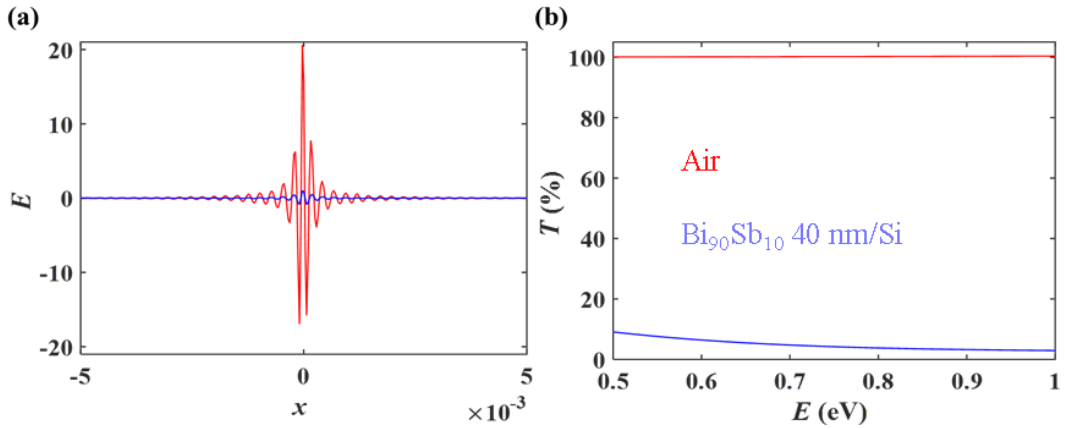

Fig. 3.2.3.2 (a) Interferogram and (b) its corresponding transmittance spectra in NIR of air (red) and a $Bi_{90}Sb_{10}$ 40 nm /Si sample (blue), respectively.

Because the BiSb/Si sample has relatively high reflectance, for FTIR transmittance measurements, the sample was slightly tilted by approximately 1 deg to prevent reflected

light of the sample from returning to the interferometer, by which the transmittance spectra can be obtained more accurately (Fig. 3.2.3.3).

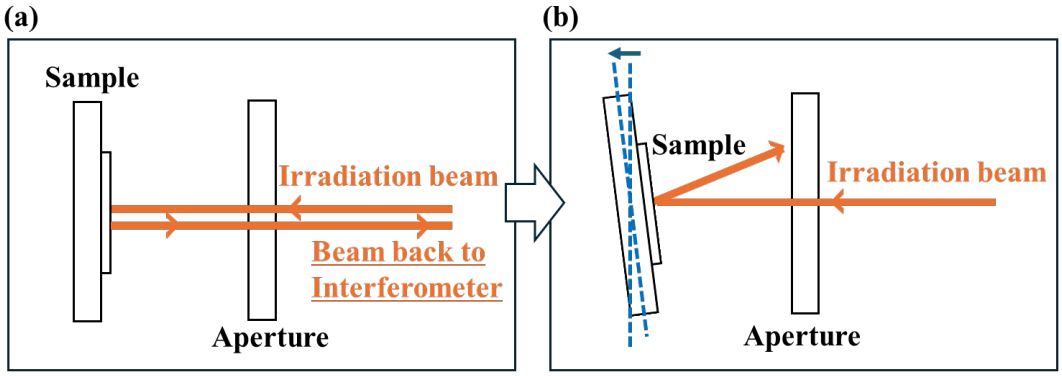

Fig. 3.2.3.3 Schematic of the transmittance measurement. The sample surface is (a) parallel to the normal of the incident light, (b) tilted by ~1 deg from the normal of the incident light.

3-2-4 Photothermoelectric response

For PTE measurements, we use a quantum cascade laser with the wavelength of 4.33 μm and the power of 28.6 mW (L12004-2310H-E, Hamamatsu Photonics) to irradiate the samples with a 1.5 mm spot size. The PTE voltage is measured by a digital multimeter (34980A, KEYSIGHT) and recorded by 5 times a second. In addition, we evaluate the rise time of the PTE voltage to reach 80% of the maximum from the light-on time and the fall time of the PTE voltage to reach 20 % from the light-off time, respectively. The measurement setup is shown in figure 3.2.4.1.

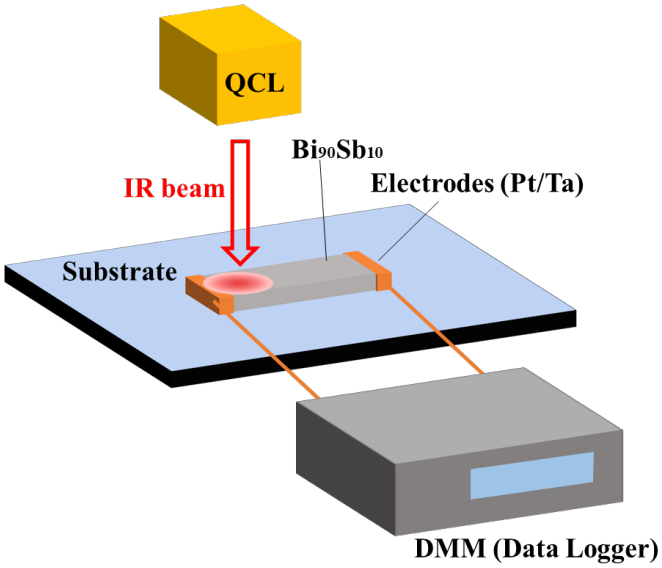

Fig. 3.2.4.1 Illustration of the measurement setup. We used a quantum cascade laser to irradiate the samples with a 1.5 mm spot size. The PTE voltage was measured by a digital multimeter and recorded by 5 times a second.

References

[1] https://www.mitutoyo.co.jp/products/measuring-tools/indicators/digimatic/main/543-781-10/

[2] M. Yasaka, “X-ray thin-film measurement techniques,” The Rigaku Journal, **26,** 1–9 (2010).

[3] O. S. Heavens, *Optical Properties of Thin Solid Films* (Butterworths, 1995), Chap. 4.

[4] T. Pisarkiewicz, "Reflection spectrum for a thin film with non-uniform thickness, "Journal of Physics D: Applied Physics, **27,** 160 (1994).

[5] J. N. Hilfiker, M. R. Linford, "Fitting the Spectroscopic Ellipsometry Data from a Rather Thick (Organic?) Film on Fused Silica Part 2 -Challenges from Bandwidth, Thickness Non-Uniformity, Absorption, and Roughness,"Vacuum Technology & Coating (2021).

[6] N. Jaggi, D.R. Vij, "FOURIER TRANSFORM INFRARED SPECTROSCOPY," In:

Vij, D. (eds) Handbook of Applied Solid State Spectroscopy, Chapter 9, 411–450 (2006).

[7] https://www.shimadzu.com/an/service-support/technical-support/ftir/tips_and_tricks/apodization.html

[8] J. J. Ojeda and M. Dirrrich, (A. Navid; Editor), "Fourier Transform Infrared Spectroscopy for Molecular Analysis of Microbial Cells" in "Microbial Systems Biology: Methods in Molecular Biology", **881**, 194 (2012).

Chapter 4. Evaluation of infra-red light absorption of BiSb

4-1 Evaluation of infra-red optical constants n,κ of BiSb by reflectance- transmittance technique

4-1-1 Overview of the RT method

Figure 4.1.1.1 shows the overview of the RT method and calculation of absorption in this work. Firstly, we measured the reflectance (R) and transmittance (T) spectra of our samples using a Fourier-transform infrared (FTIR) spectrometer (IRTracer-100, Shimadzu).

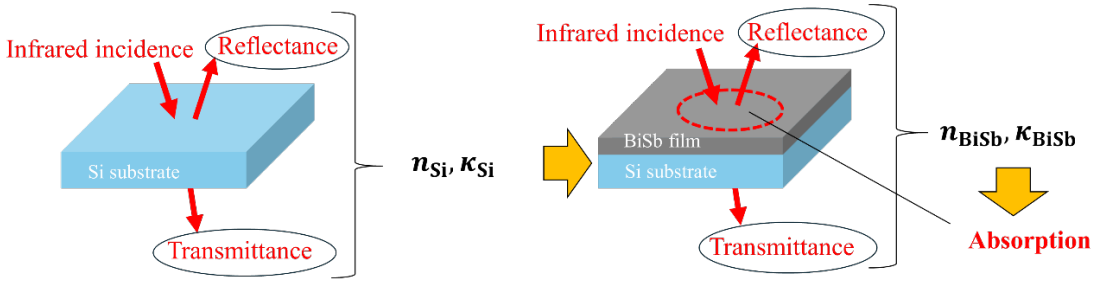

Fig. 4.1.1.1 Overview of the RT method and calculation of absorption. The incident angle is 0 and 10 deg for transmittance and reflectance measurement, respectively.

The measurements covered the mid-infrared (MIR, 0.02 eV - 0.5 eV) and near-infrared (NIR, 0.5 eV - 1 eV) regions with a resolution of 4 cm^{-1}, by two different light sources and detectors. For reflectance measurements, we used a specular reflectance measurement unit (SRM-8000A, Shimadzu) where the incident angle is 10 degrees oblique, and a protected gold mirror (PFSQ10-03-M01, Thorlabs) was employed as a reference. For

transmittance measurements, a blank was used as a reference. Due to the oblique incidence for R measurement, it is essential to take into account the polarization ratio of s-polarization and p-polarization for calculations. To determine the polarization ratio, we measured transmittance through an IR wire grid filter (Edmund optics) by rotating it in 10 degrees increments. The results are shown in Fig. 4.1.1.2. The average spectrum is centered between 0 degrees and 90 degrees in both MIR and NIR, indicating that the ratio of p:s is 1:1 for our light sources.

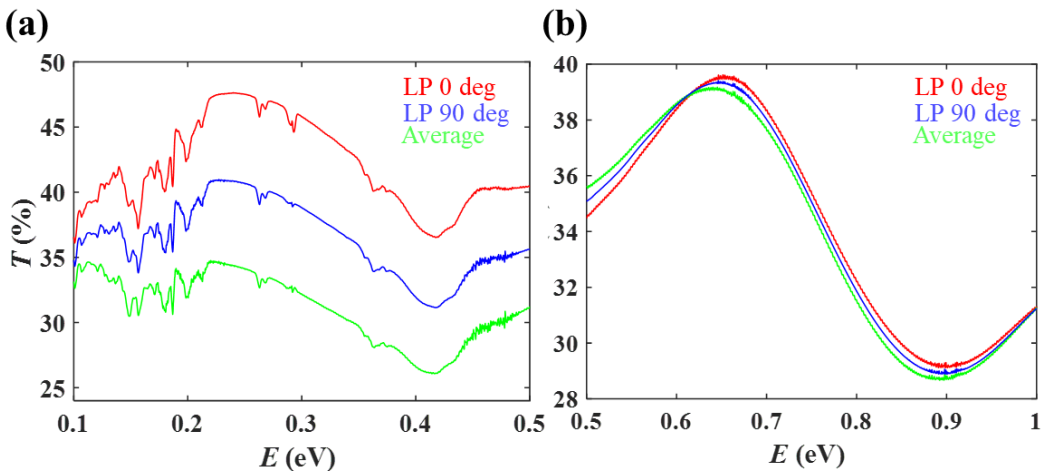

Fig. 4.1.1.2 Transmittance spectrum measured through an IR wire grid filter (Edmund optics) by rotating it in 10 degrees increments. (a) MIR (b) NIR.

Before theoretical RT fitting, we smoothed small oscillations in the measured (R,T) spectra due to noise and interference in the Si substrate, which are not favored for our fitting process. First, we determined the (n, κ) of Si by fitting the smoothed (R,T) spectra of the Si substrates using coherent transmission and reflection theory of a single layer [1]. In the calculation, we assumed non-uniform thicknesses of the Si substrates, with thickness varying from 1000 to 1050 μm (0.01 μm step, 5001 different thicknesses), and

averaged the calculated (R,T) spectra over this thickness range. This procedure suppresses the small oscillations in the calculated (R,T) spectra due to interference in the substrate [2]. Some small oscillations in the obtained (n, κ) of Si are also smoothed. Then, we calculated the (n, κ) of Bi, $Bi_{90}Sb_{10}$, and $Bi_{85}Sb_{15}$ using coherent transmission and reflection theory of multilayers and the (n, κ) values of Si. It is known that (n,κ) solution from (R,T) is generally not unique [3]. As shown in Fig.4.1.1.3, not one but several intersections of reflectance and transmittance contours can be seen. Hence we set initial values and constraints based on the discrete literature data. Finally, the absorption of each film was calculated using the obtained (n, κ).

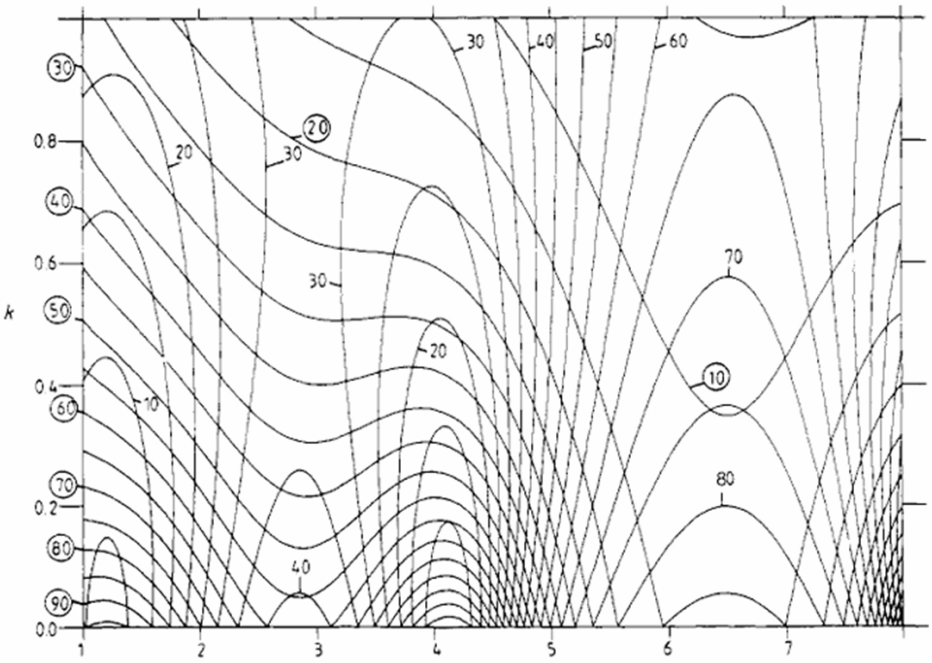

Fig. 4.1.1.3 Contours of R and T [3]. Reprinted with permission from Journal of Physics D: Applied Physics.

We first determined the complex refractive indices of a Si substrate, which is necessary

for later fitting. Figure 4.1.1.4 (a) shows the (R,T) spectra of the Si substrate. The discontinuous jump at 0.5 eV in the spectra is due to the mismatch of MIR and NIR at 0.5 eV. Figure 4.1.1.4(b) shows the obtained (n, κ) of Si, which is about (3.5, 0) for Si and almost the same as those reported in literature [4].

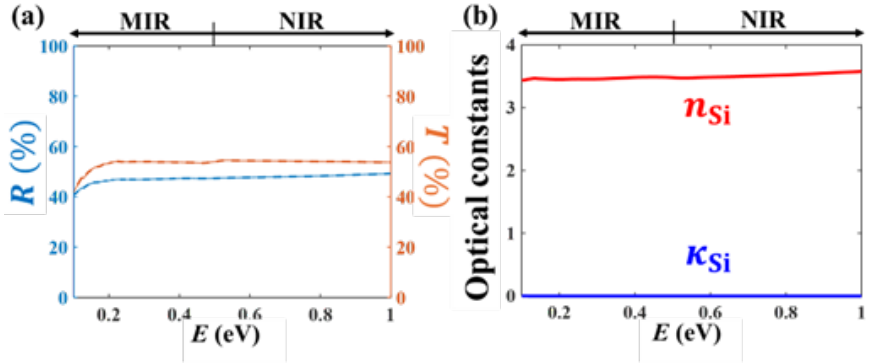

Fig. 4.1.1.4 (a) RT experimental results (solid) and fitting (dashed) of a Si substrate. (b) Calculated (n,κ) of the Si substrate.

4-1-2 (n, κ) map

Figure 4.1.2.1-4.1.2.9 show the (n,κ) maps of BiSb obtained by the Heavens' matrix method. There are two intersection points of the measured R and T indicated by red circles.

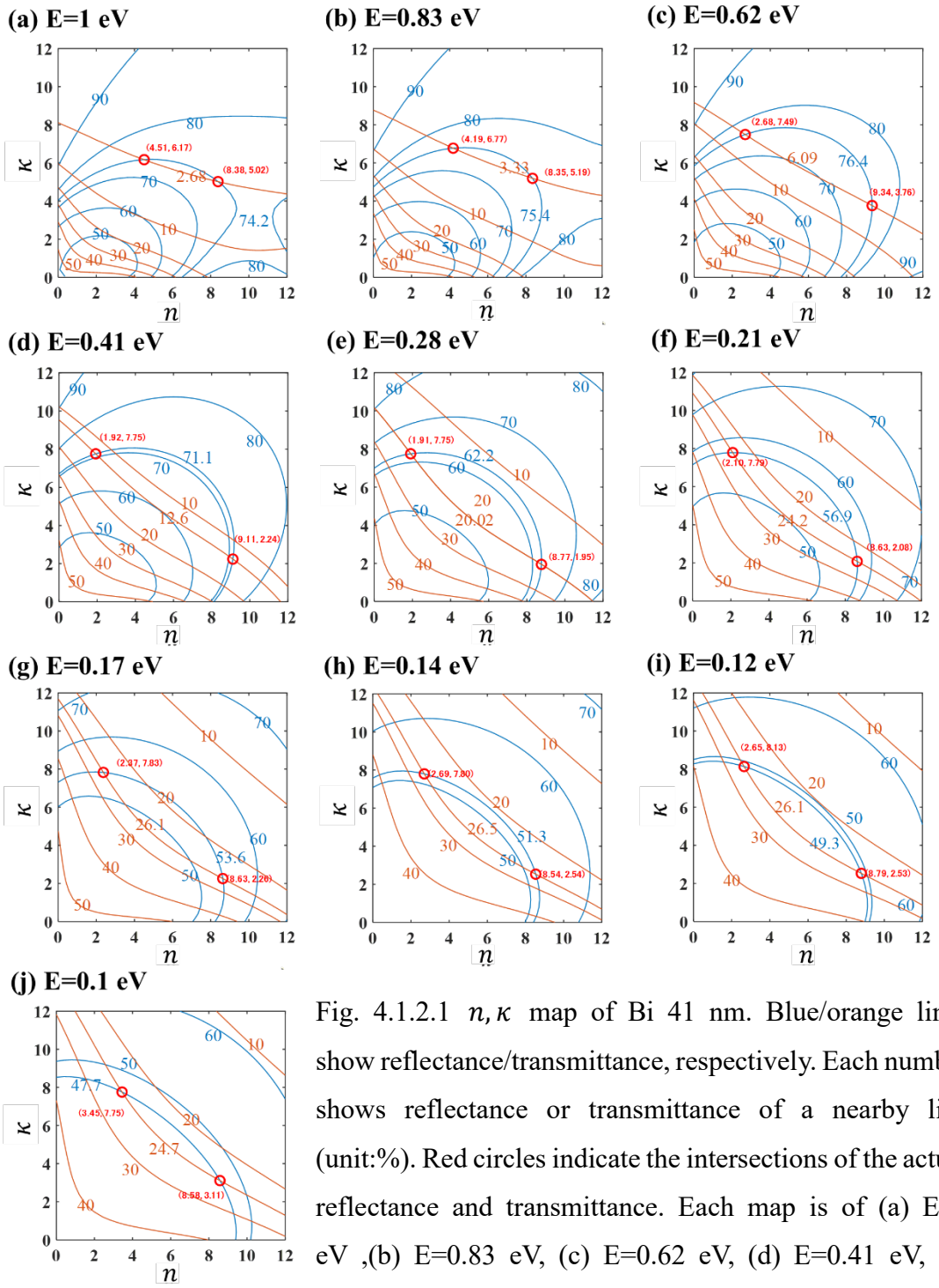

Fig. 4.1.2.1 n, κ map of Bi 41 nm. Blue/orange lines show reflectance/transmittance, respectively. Each number shows reflectance or transmittance of a nearby line (unit:%). Red circles indicate the intersections of the actual reflectance and transmittance. Each map is of (a) E=1 eV ,(b) E=0.83 eV, (c) E=0.62 eV, (d) E=0.41 eV, (e) E=0.28 eV, (f) E=0.21 eV, (g) E=0.17 eV, (h) E=0.14 eV, (i) E=0.12 eV, (j) E=0.1 eV.

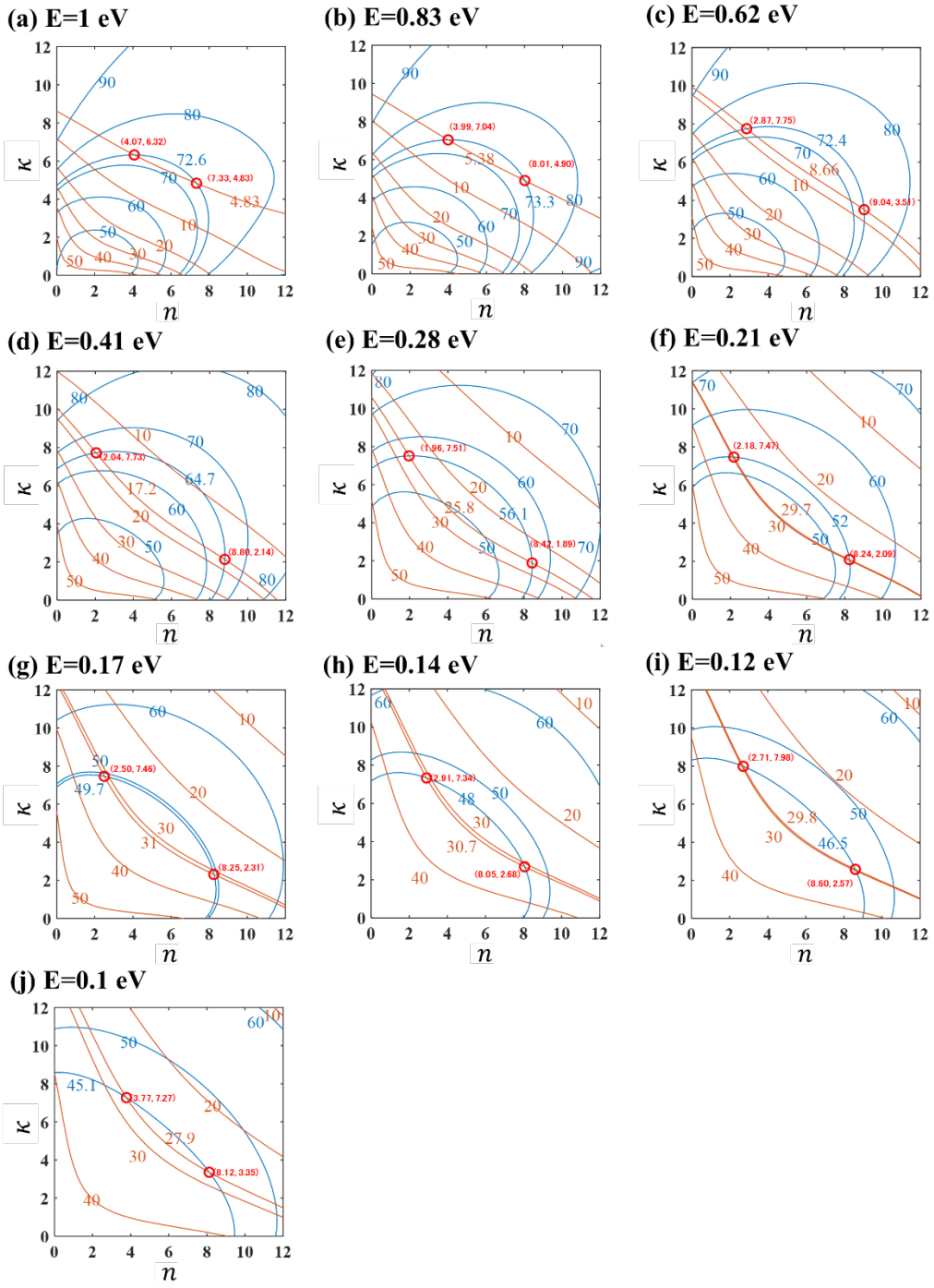

Fig. 4.1.2.2 n, κ map of Bi 31 nm. Colors and energies are the same as Fig. 4.1.2.1.

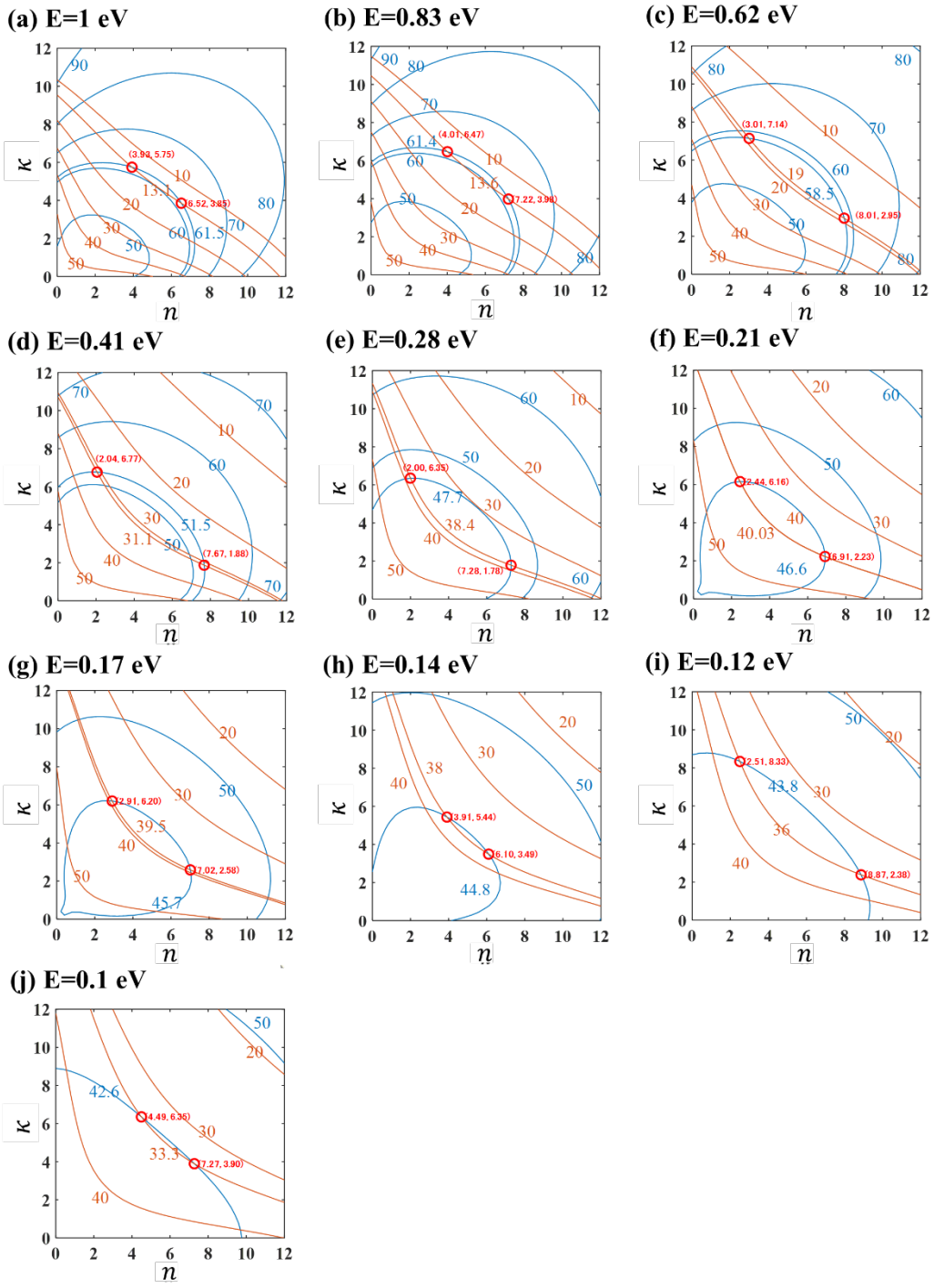

Fig. 4.1.2.3 n, κ map of Bi 17 nm. Colors and energies are the same as Fig. 4.1.2.1.

.

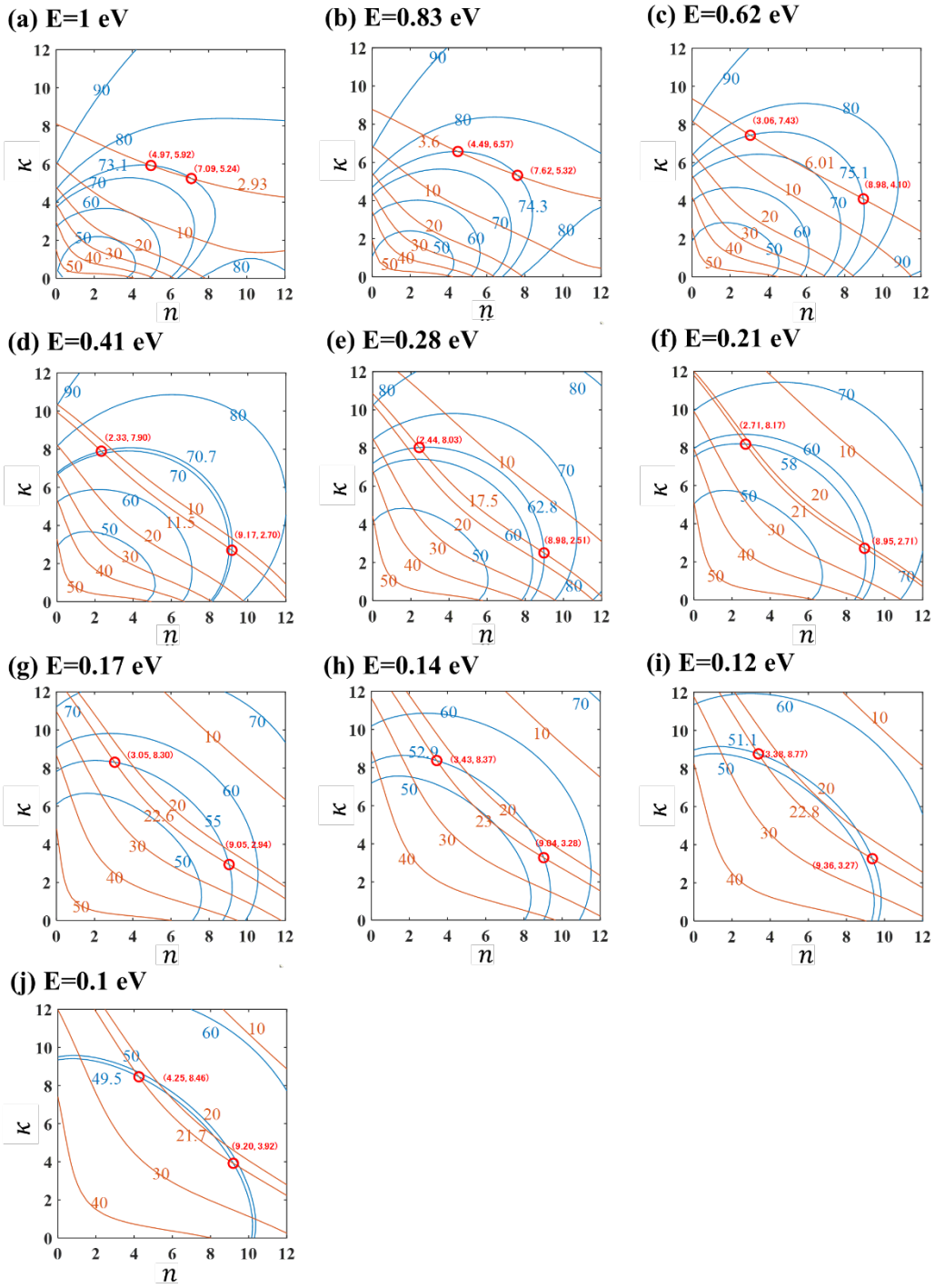

Fig. 4.1.2.4 n, κ map of $Bi_{90}Sb_{10}$ 40 nm. Colors and energies are the same as Fig. 4.1.2.1.

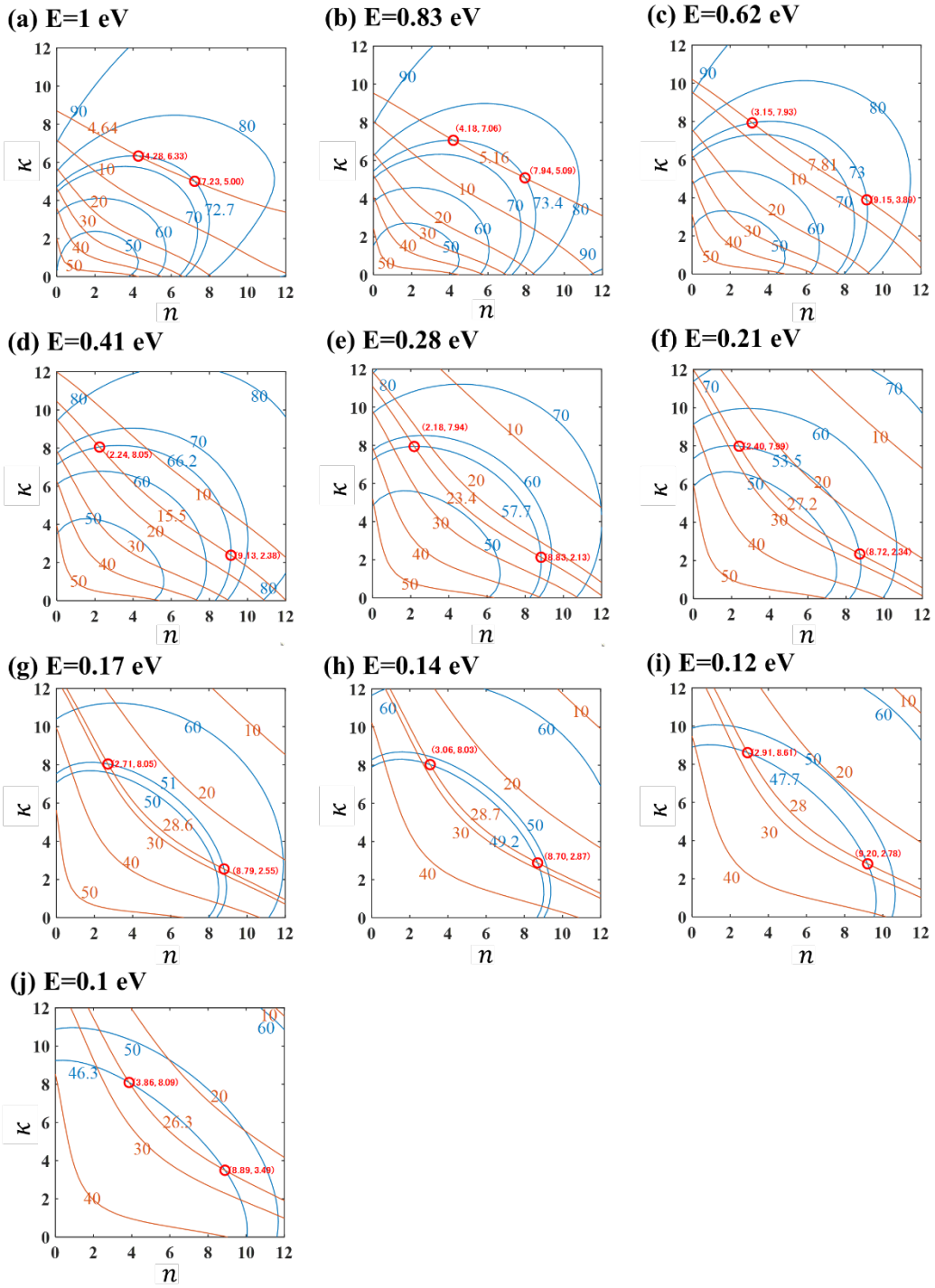

Fig. 4.1.2.5 n, κ map of $Bi_{90}Sb_{10}$ 31 nm. Colors and energies are the same as Fig. 4.1.2.1.

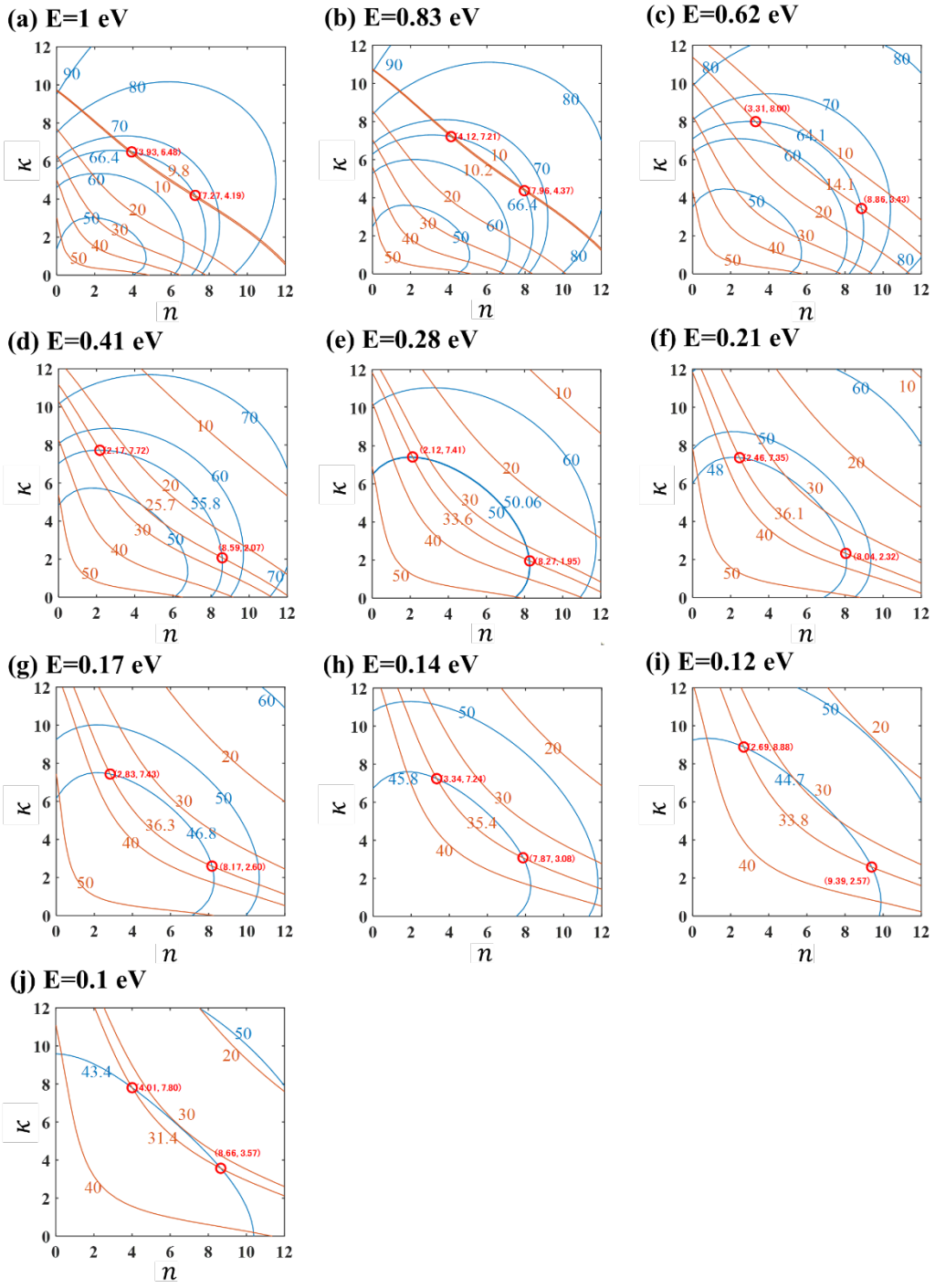

Fig. 4.1.2.6 n, κ map of $Bi_{90}Sb_{10}$ 19 nm. Colors and energies are the same as Fig. 4.1.2.1.

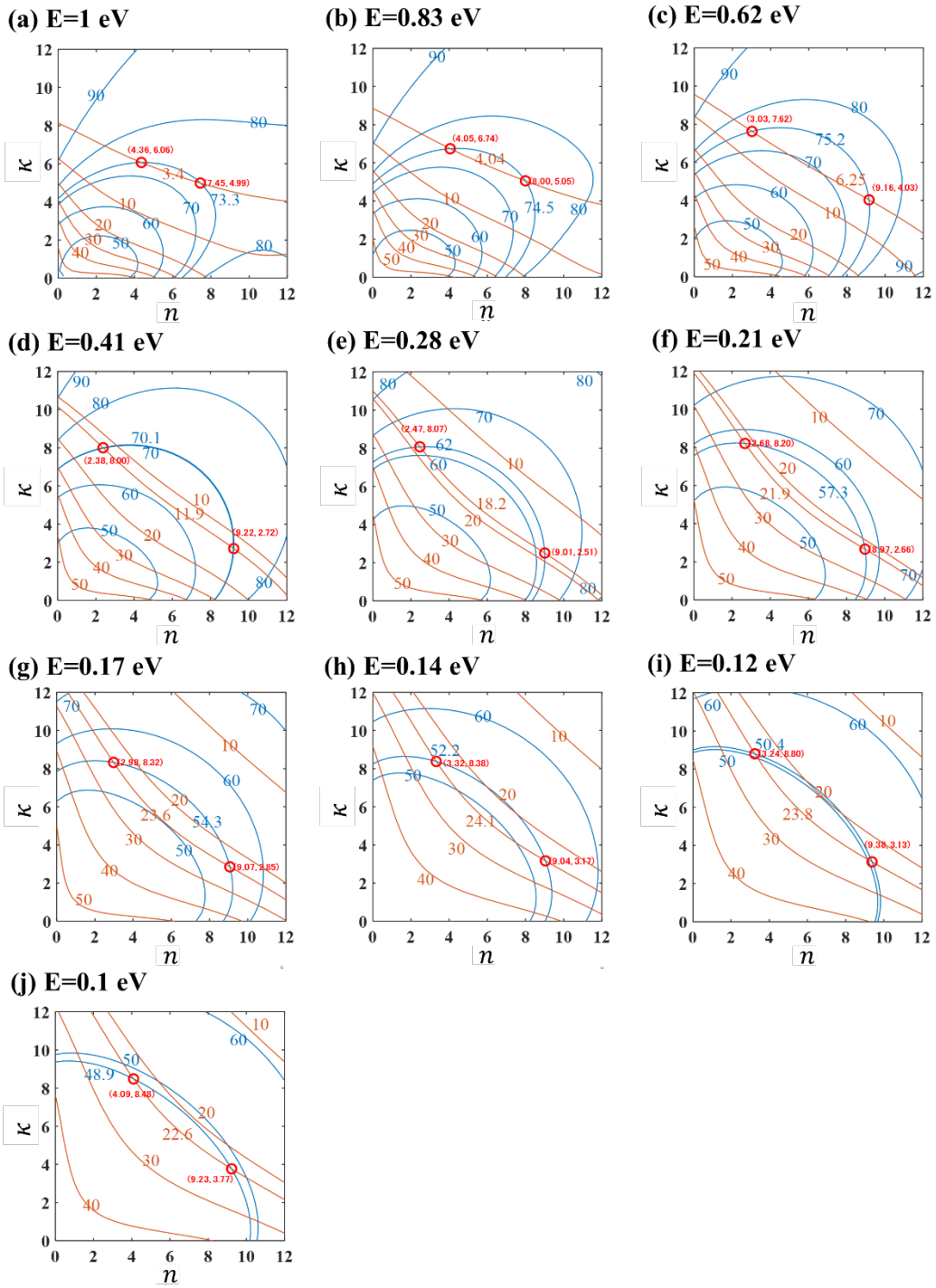

Fig. 4.1.2.7 n, κ map of $Bi_{85}Sb_{15}$ 38 nm. Colors and energies are the same as Fig. 4.1.2.1.

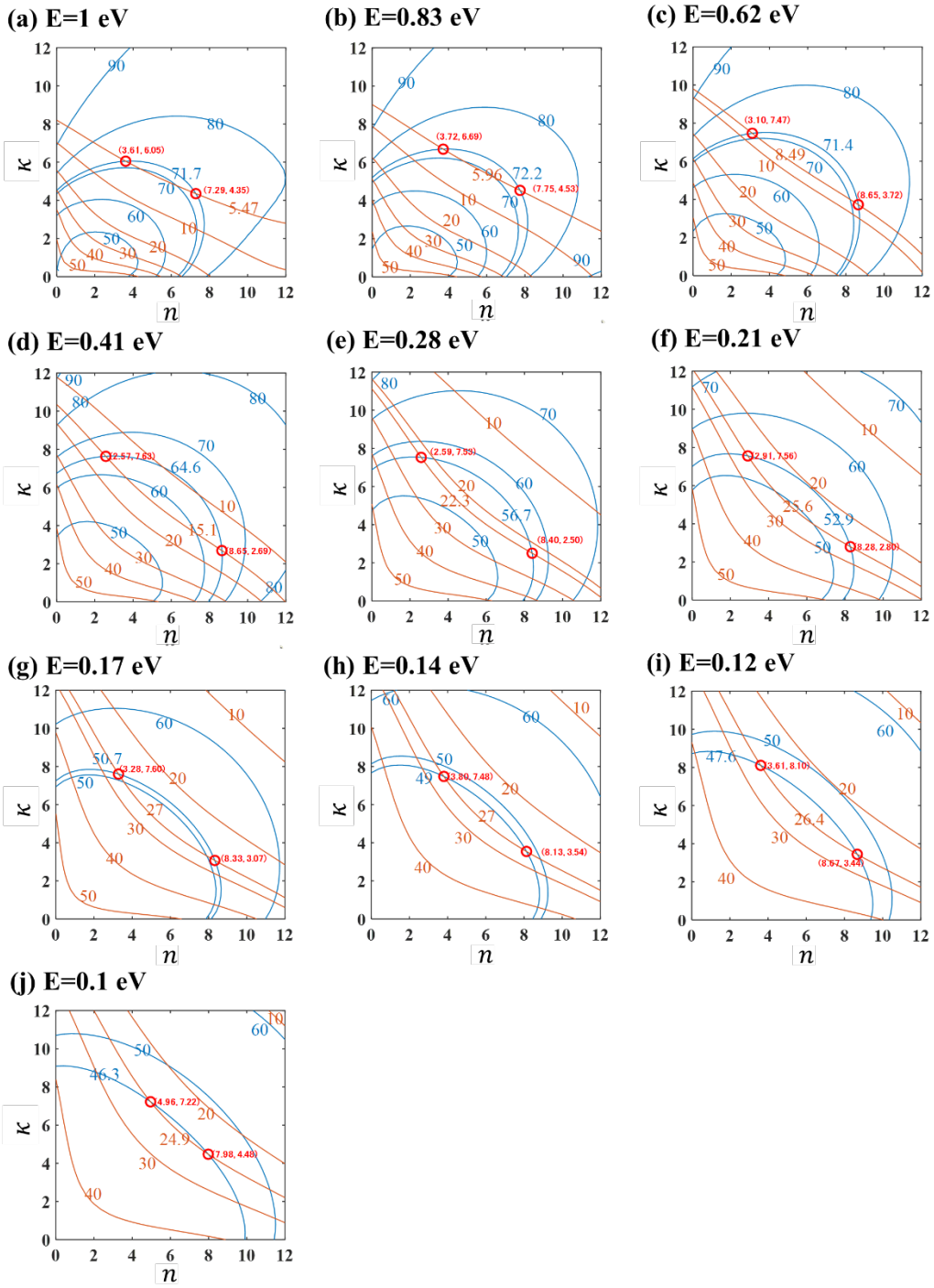

Fig. 4.1.2.8. n, κ map of $Bi_{85}Sb_{15}$ 32 nm. Colors and energies are the same as Fig. 4.1.2.1.

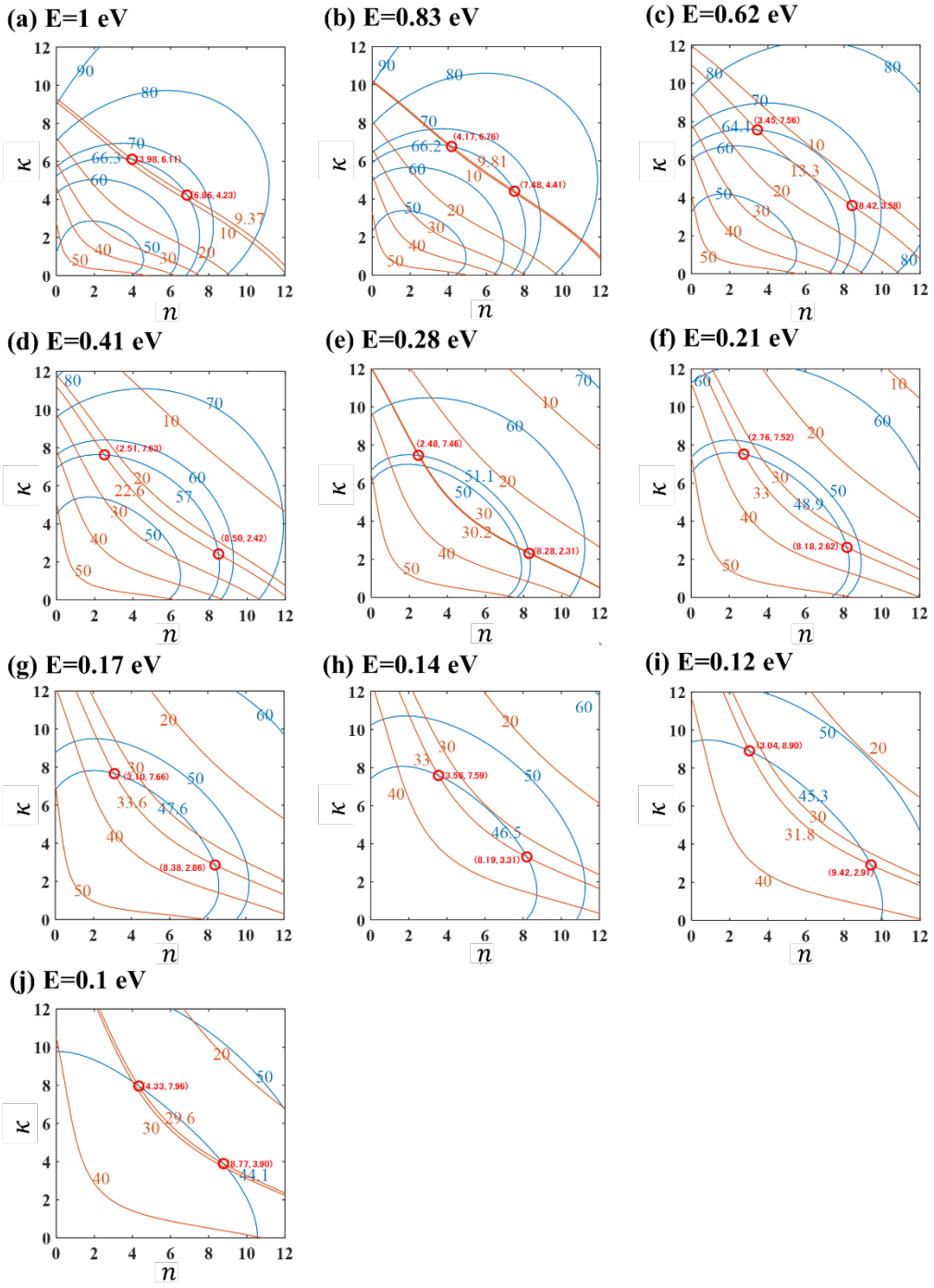

Fig. 4.1.2.9 n, κ map of $Bi_{85}Sb_{15}$ 21 nm. Colors and energies are the same as Fig. 4.1.2.1.

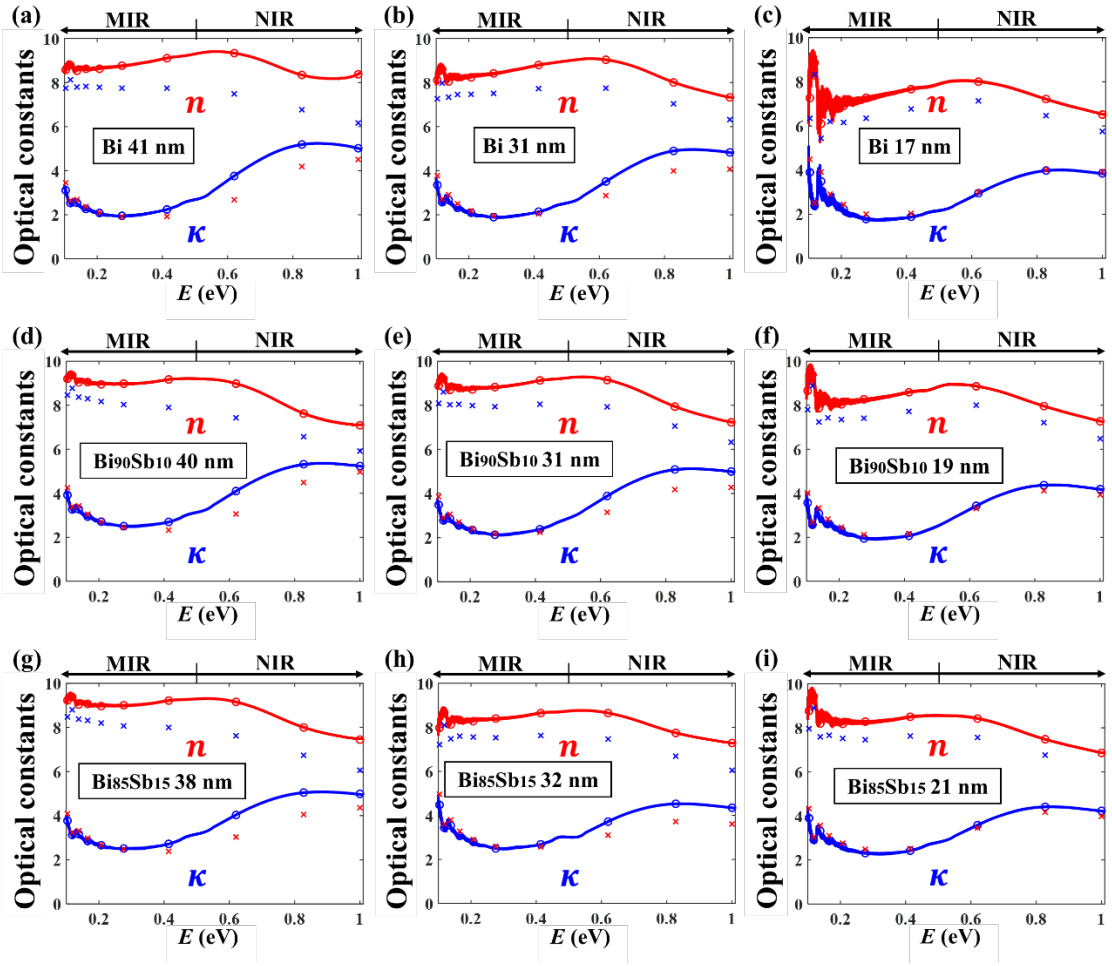

Fig. 4.1.2.10 (n, κ) plots obtained from the intersections of the n, κ map ($n > \kappa$: 'o', $n < \kappa$: '×') and solid lines representing the (n, κ) values determined by RT fitting as presented in the next section. All values were obtained using the Heavens' matrix method. Samples are (a-c) Bi 41, 31, 17 nm, (d-f) $Bi_{90}Sb_{10}$ 40, 31, 19 nm, (g-i) $Bi_{85}Sb_{15}$ 38, 32, 21 nm, respectively.

Figure 4.1.2.10 summarizes (n, κ) plots obtained from the intersections of the n, κ map ($n > \kappa$: 'o', $n < \kappa$: '×') and solid lines representing the (n, κ) values determined by RT fitting as presented in the next section. All values were obtained using the Heavens' matrix method. Samples are (a-c) Bi 41, 31, 17 nm, (d-f) $Bi_{90}Sb_{10}$ 40, 31, 19 nm, (g-i) $Bi_{85}Sb_{15}$ 38, 32, 21 nm, respectively. Using the fact that $n > \kappa$ were obtained in Bi thin films by

using a synchrotron light source and the Kramers-Kronig analysis [5], we will use the (n, κ) values with $n > \kappa$.

4-1-3 Determination of (n,κ) of BiSb by fitting

Figures 4.1.3.1(a), 4.1.3.1(c), and 4.1.3.1(e) show the experimental (R,T) spectra (solid curves) and their fitting (dashed curves) for Bi (17, 31, 41 nm), $Bi_{90}Sb_{10}$ (19, 31, 40 nm), $Bi_{85}Sb_{15}$ (19, 31, 40 nm) on Si substrates, respectively. The spectra show the same trend among Bi, $Bi_{90}Sb_{10}$, $Bi_{85}Sb_{15}$; reflectance is 40-80 %, transmittance is 0-40 % for the film thickness of about 20-40 nm, and reflectance (transmittance) increases (decreases) with increasing thickness. Figures 4.1.3.1(b), 4.1.3.1(d), and 4.1.3.1(f) show the obtained (n,κ) of Bi (17, 31, 41 nm), $Bi_{90}Sb_{10}$ (19, 31, 40 nm), $Bi_{85}Sb_{15}$ (21, 32, 38 nm), respectively. To validate our technique, we first compare the obtained (n,κ) values of Bi to those measured by using a synchrotron light source and the Kramers-Kronig analysis [5]. The obtained κ of Bi are almost the same as those estimated by the Kramers-Kronig analysis in the studied 0.1 eV – 1 eV range, lying between 2-6. However, the obtained n are slightly higher than the reference values. This may be due to the difference in the method or film thickness.

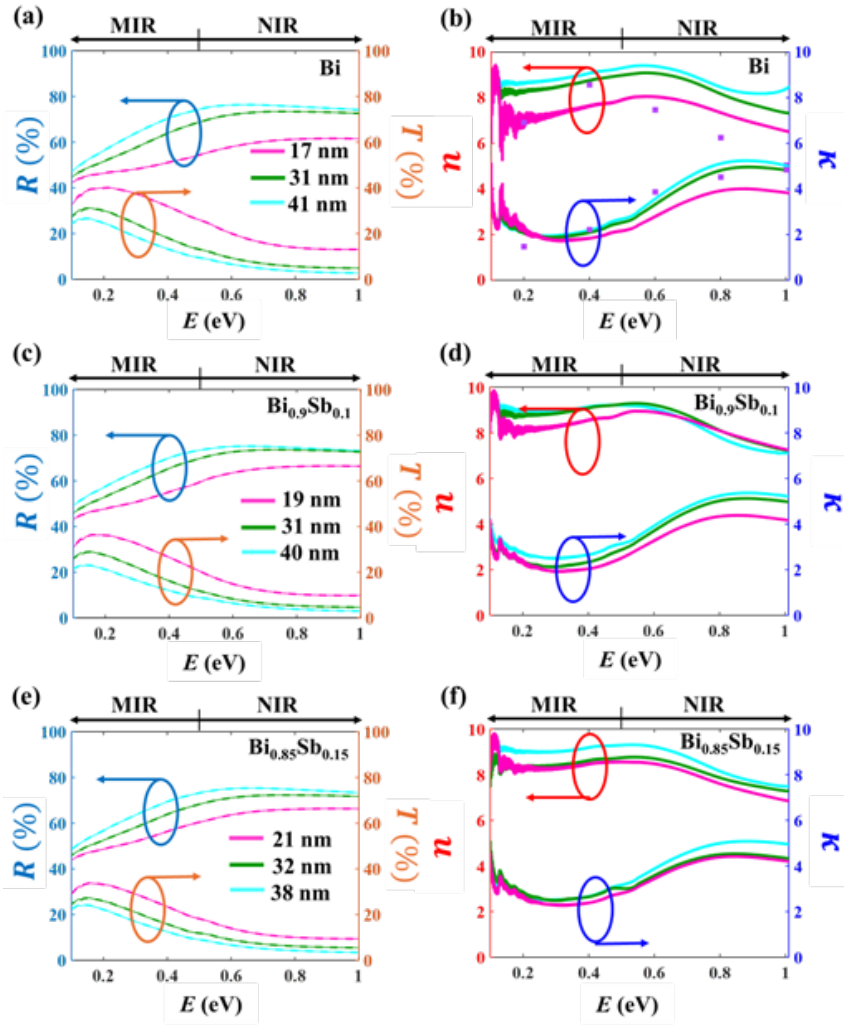

Fig. 4.1.3.1. (a) RT experimental results (solid) and fitting (dashed) of Bi (17, 31, 41 nm) on Si. (b) Calculated (n,κ) of Bi (17, 31, 41 nm) films (solid) and (n,κ) of Bi from the literature (dots). (c) RT experimental results (solid) and fitting (dashed) of $Bi_{90}Sb_{10}$ (19, 31, 40 nm) on Si. (d) Calculated (n,κ) of $Bi_{90}Sb_{10}$ (19, 31, 40 nm) films. (e) RT experimental results (solid) and fitting (dashed) of $Bi_{85}Sb_{15}$ (21, 32, 38 nm) on Si. (f) Calculated (n,κ) of $Bi_{85}Sb_{15}$ (21, 32, 38 nm) films.

Comparing the (n,κ) of different Sb compositions and thicknesses, there is no clear difference among the Sb compositions and no clear trend among thicknesses. As our

main purpose is to estimate optical absorption, we concluded that the refractive index n and the extinction coefficient κ of Bi, $Bi_{90}Sb_{10}$, $Bi_{85}Sb_{15}$ are between 6-9 and 2-6, respectively, which show almost the same trend and no outstanding effect of Sb compositions (0%, 10%, 15%) on the optical constant of BiSb in the 0.1-1 eV range.

4-2 Verification of the validity of the obtained optical properties

To verify the validity of the obtained (n,κ), we calculate the reflectance spectra of Bi (90 nm) and $Bi_{90}Sb_{10}$ (156 nm)/Au/glass samples and compare them with their experimental R spectra. Here, the Au layer acts as a perfect reflector in the studied photon energy range. The calculated and measured R spectra are shown in Fig. 4.2.1. The calculated spectra are in good agreement with the measured spectra. Especially, positions and intensities of interference extrema are almost the same for Bi (90 nm) and $Bi_{90}Sb_{10}$ (156 nm). These results confirm the validity of our obtained (n,κ) for a broad range of thickness.

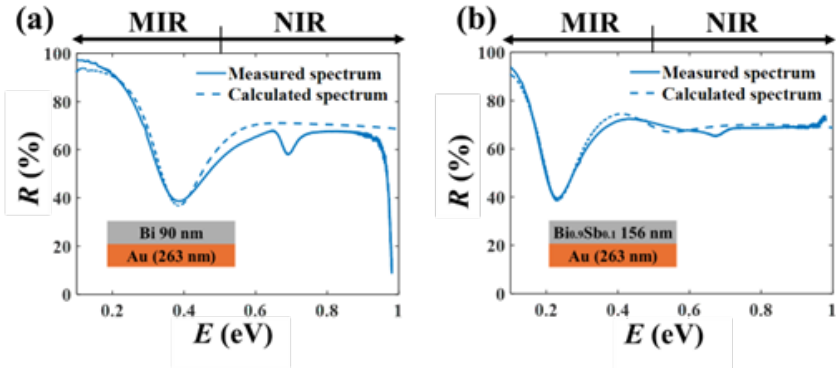

Fig. 4.2.1. Calculated and measured reflectance spectrum of (a) Bi (90 nm)/Au/glass, and (b) $Bi_{90}Sb_{10}$ (156 nm)/Au/glass. We assumed nearly 100% reflectance of Au [6] and a phase-shift correction [7].

4-3 Calculation of absorption from the relation of $A+R+T=1$

Using the obtained (n,κ), we calculated the absorption A=100%-R-T of Bi (17 nm), $Bi_{90}Sb_{10}$ (19 nm), $Bi_{85}Sb_{15}$ (21 nm) films under normal incidence. For comparison, we also calculated the absorption of 20 nm Bi_2Te_3 using the values of the literature [8]. The calculations were performed for free-standing thin films. The results are shown in Fig. 4.3.1. Bi, $Bi_{90}Sb_{10}$, and $Bi_{85}Sb_{15}$ show notably higher absorption than Bi_2Te_3 in the MIR range. The higher absorption of BiSb in the MIR range originates from its much smaller bandgap than that of Bi_2Te_3. Therefore, BiSb can be a good MIR absorber for MIR detectors.

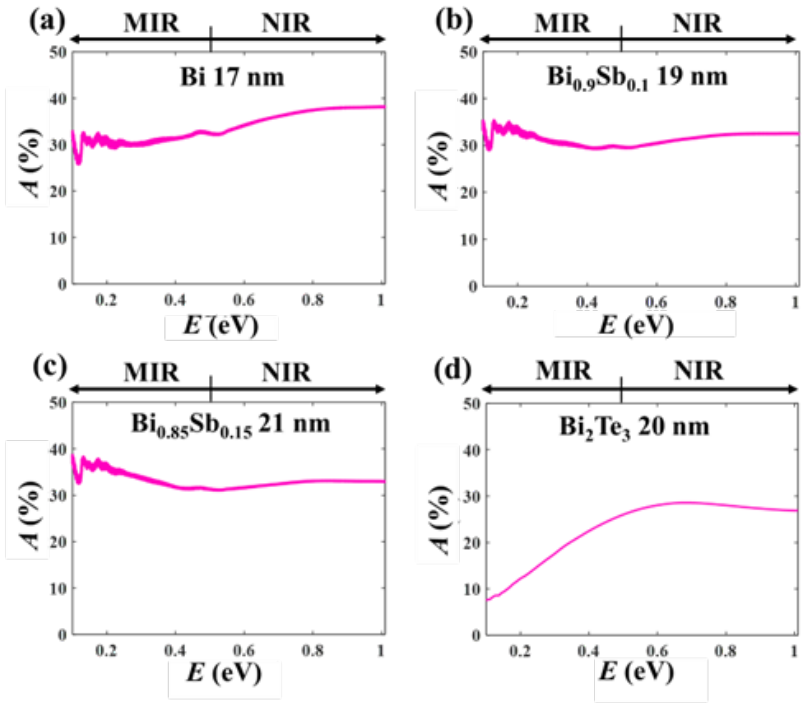

Fig. 4.3.1. Calculated absorption spectra of free-standing thin films of (a) Bi (17 nm), (b) $Bi_{90}Sb_{10}$ (19 nm), (c) $Bi_{85}Sb_{15}$ (21 nm), (d)Bi_2Te_3 (20 nm), respectively. For Bi, $Bi_{90}Sb_{10}$, $Bi_{85}Sb_{15}$, the obtained (n,κ) for each thickness was used to calculate the absorption. For Bi_2Te_3, we used the literature's (n,κ) data [8].

4-4 Optical transition of absorption in IR

In Fig. 4.3.1, the absorption of BiSb in MIR is higher than that of Bi_2Te_3. This can be attributed to the difference of bulk bandgap. As shown in chapter 1, for optical transition in TI, there are several cases; (1) Surface-states-related absorption or (2) Surface-states-non-related absorption. Due to Dirac cones, the surface states can be involved in the case of a weak energy light such as THz. Regarding the IR absorption, not only surface bands but also bulk bands can contribute. As BiSb has a smaller bulk gap than Bi_2Te_3, absorption curve is expected to rise from the much lower energy than Bi_2Te_3. Therefore, we can explain the already saturated absorption of BiSb in MIR at 0.1 eV, while the absorption curve is still rising towards higher energy in the MIR for Bi_2Te_3 (see Fig. 4.4.1) [9].

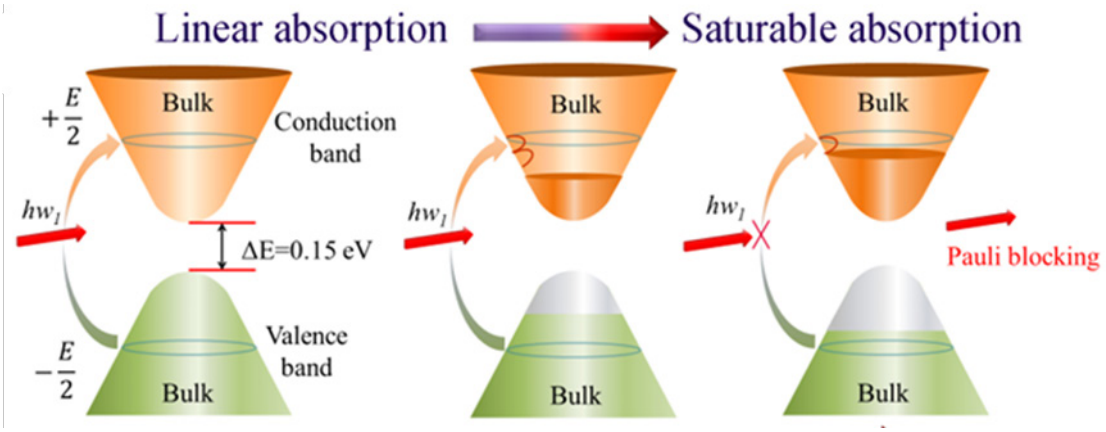

Fig. 4.4.1 Schematic of an optical saturable absorption in Bi_2Te_3 [9]. Reprinted with permission from Optical Materials Express.

Appendix: MATLAB codes for obtaining (n, κ) by fitting

```
clear
close all
```

```
% Reading the data file
filepath = ".¥Results.xlsx";

% Reading the data of wavelength, photon energy (x-axis)
m_wavelength= readmatrix(filepath,"sheet",1, "Range","B2:B7445")*1e-6 ;
ev_hnu= readmatrix(filepath,"sheet",1, "Range","D2:D7445");

% Reading the actual reflectance, transmittance of the sample (smoothed)
refl_act = readmatrix(filepath,"sheet",7, "Range", "F2:F7445") / 100;
tran_act = readmatrix(filepath,"sheet",6, "Range", "F2:F7445") / 100;

% Reading the obtained n, κ of Si (smoothed)
Si_n_act = readmatrix(filepath,"sheet",8, "Range", "AQ2:AQ7445");
Si_k_act = readmatrix(filepath,"sheet",8, "Range", "AR2:AR7445");

% Thickness of Bi or BiSb
Bi_d_thick =19e-9;

% Definition of the calculated n, κ, R, T
vec_n3 = zeros(size(m_wavelength)); vec_k3 = zeros(size(m_wavelength));
refl_est = zeros(size(m_wavelength)); tran_est = zeros(size(m_wavelength));

% Virtual thickness range and step size of Si substrate
d_thick_list = 1000e-6 : 0.01e-6 : 1050e-6;
d_step = d_thick_list(2) - d_thick_list(1);

% Ratio of the p-polarized component (0≤y≤1)
y=0.5;

% 1st for loop to find n, κ (fmincon)
tic;
```

```
shokichi = [6, 2];
for ii = 1 : length(m_wavelength)
    nk = fmincon(@(nk)obj_func(nk(1), nk(2), refl_act(ii), tran_act(ii),
        m_wavelength(ii), Bi_d_thick, d_thick_list,Si_n_act(ii), Si_k_act(ii), y)
        ,shokichi, [], [], [], [], [0, 0], [15, 7]);
    vec_n3(ii) = nk(1); vec_k3(ii) = nk(2);
    shokichi = nk;
end
toc

% 2nd for loop to recalculate R, T using the obtained n, κ
for ii = 1 : length(m_wavelength)
    n = vec_n3(ii); k = vec_k3(ii);
    lambda = m_wavelength(ii);
    refl_vec = est_refl(n, k, lambda, Bi_d_thick, d_thick_list, Si_n_act(ii),
            Si_k_act(ii), y);
    tran_vec = est_tran(n, k, lambda, Bi_d_thick, d_thick_list, Si_n_act(ii),
            Si_k_act(ii),y);

    % Integration of R, T over the thickness range
    refl_est(ii) = sum(refl_vec) *d_step / (d_thick_list(end) - d_thick_list(1));
    tran_est(ii) = sum(tran_vec) *d_step / (d_thick_list(end) - d_thick_list(1));
end

% Writing the obtained data (n, κ, R, T) in the data file
writematrix(vec_n3,filepath,"sheet",8,"Range","G2:G7445");
writematrix(vec_k3,filepath,"sheet",8,"Range","H2:H7445");
writematrix(refl_est,filepath,"sheet",10,"Range","F2:F7445");
writematrix(tran_est,filepath,"sheet",9, "Range", "F2:F7445");

% Plot figure for R, T
```

```
figure
 subplot(2, 1, 1)
 hold on
 plot(ev_hnu, 100 * refl_act); plot(ev_hnu, 100 * refl_est, "--")
 xlim([0.25, 1]); ylim([0, 100]); xlabel("Energy [eV]"); ylabel("Reflectance [%]")
 legend("Actual spectrum", "Fitting curve")

 subplot(2, 1, 2)
 hold on
 plot(ev_hnu, 100 * tran_act); plot(ev_hnu, 100 * tran_est, "--")
 xlim([0.25, 1]); ylim([0, 100]); xlabel("Energy [eV]"); ylabel("Transmittance [%]")
 legend("Actual spectrum", "Fitting curve")

% Plot figure for n, κ
figure
 subplot(2, 1, 1)
 hold on
 plot(ev_hnu,vec_n3)
 xlabel("Energy [eV]"); ylabel("{¥itn}"); xlim([0.1, 1]); ylim([0, 13])

 subplot(2, 1, 2)
 hold on
 plot(ev_hnu,vec_k3)
 xlabel("Energy [eV]"); ylabel("{¥it¥kappa}"); xlim([0.1, 1]); ylim([0, 13])

% Function for integration calculation (used in the 1st for loop)
function val = obj_func(n, k, refl, tran, wavelength, Bi_d_thick,d_thick_list, Si_n,
                Si_k,y)
    d_step = d_thick_list(2) - d_thick_list(1);

    refl_all = est_refl(n, k, wavelength, Bi_d_thick, d_thick_list, Si _n, Si _k, y);
```

```
    tran_all = est_tran(n, k, wavelength, Bi_d_thick, d_thick_list, Si _n, Si _k,y);
    % Integration of R, T over the thickness range
    refl_integration = sum(refl_all) *d_step / (d_thick_list(end) - d_thick_list(1));
    tran_integration = sum(tran_all) *d_step / (d_thick_list(end) - d_thick_list(1));

    val = (refl - refl_integration)^2 + (tran - tran_integration)^2;
end

% Function for reflectance calculation
function refl_list = est_refl(n, k, wavelength, Bi_d_thick, d_thick_list, Si_n_act,
                              Si_k_act, y)
    % Defination of n, κ
    n1 = 1;
    n2 = n - 1i * k;
    n3 = Si_n_act - 1i * Si_k_act;
    n4 = 1;

    % sin, cos for Fresnel coefficient (Incident angle = 10 deg)
    rad_theta1 = 10 / 180 * pi;
    cos_theta1 = cos(rad_theta1);
    sin_theta2 = n1 * sin(rad_theta1) ./ n2; cos_theta2 = sqrt(1 - sin_theta2.^2);
    sin_theta3 = n2 * sin_theta2 ./ n3; cos_theta3 = sqrt(1 - sin_theta3.^2);
    sin_theta4 = n3 .* sin_theta3 ./ n4; cos_theta4 = sqrt(1 - sin_theta4.^2);

    % Fresnel coefficient for s-polarization, p-polarization, respectively
    r1_s = (n2 .* cos_theta2 - n1 * cos_theta1) ./ (n2 .* cos_theta2 + n1 * cos_theta1);
    r2_s = (n3 .* cos_theta3 - n2 .* cos_theta2) ./ (n3 .* cos_theta3 + n2 .* cos_theta2);
    r3_s = (n4 * cos_theta4 - n3 .* cos_theta3) ./ (n4 * cos_theta4 + n3 .* cos_theta3);

    r1_p = (n2 * cos_theta1 - n1 .* cos_theta2) ./ (n2 * cos_theta1 + n1 .* cos_theta2);
    r2_p = (n3 .* cos_theta2 - n2 .* cos_theta3) ./ (n3 .* cos_theta2 + n2 .*cos_theta3);
```

```
r3_p = (n4 .* cos_theta3 - n3 .* cos_theta4) ./ (n4 .* cos_theta3 + n3 .*cos_theta4);

% Phase difference
delta_Bi = 2*pi*n2*cos_theta2*Bi_d_thick/wavelength;
delta_Si = 2*pi*n3.*cos_theta3.*(Bi_d_thick + d_thick_list)./wavelength;

% Reflectance calculation for s-polarization
A11_s = 1; A12_s = r1_s; A21_s = r1_s; A22_s = 1;
B11_s = exp(1i * delta_Bi); B12_s = r2_s * exp(1i * delta_Bi);
B21_s = r2_s * exp(-1i * delta_Bi); B22_s = exp(-1i * delta_Bi);
C11_s = exp(1i * delta_Si); C21_s = r3_s .* exp(-1i * delta_Si);

X11_s = (A11_s * (B11_s .* C11_s + B12_s .* C21_s)) + (A12_s * (B21_s .*
        C11_s + B22_s .* C21_s));
X21_s = (A21_s * (B11_s .* C11_s + B12_s .* C21_s)) + (A22_s * (B21_s .*
        C11_s + B22_s .* C21_s));

r_s = X21_s ./ X11_s; R_s = abs(r_s).^2;

% Reflectance calculation for p-polarization
A11_p = 1; A12_p = r1_p; A21_p = r1_p; A22_p = 1;
B11_p = exp(1i * delta_Bi; B12_p = r2_p * exp(1i * delta_Bi);
B21_p = r2_p * exp(-1i * delta_Bi); B22_p = exp(-1i * delta_Bi);
C11_p = exp(1i * delta_Si); C21_p = r3_p .* exp(-1i * delta_Si);

X11_p = (A11_p * (B11_p .* C11_p + B12_p .* C21_p)) + (A12_p * (B21_p .*
        C11_p + B22_p .* C21_p));
X21_p = (A21_p * (B11_p .* C11_p + B12_p .* C21_p)) + (A22_p * (B21_p .*
        C11_p + B22_p .* C21_p));

r_p = X21_p ./ X11_p; R_p = abs(r_p).^2;
```

```
    % Sum of the reflectances
    refl_list = R_s * (1 - y) + R_p * y;
end

% Function for transmittance calculation
function tran_list = est_tran(n, k, wavelength, Bi_d_thick, Si_d_thick, Si_n_act,
Si_k_act,y)
    % Definition of n, κ
    n1 = 1;
    n2 = n - 1i * k;
    n3 = Si_n_act - 1i * Si_k_act;
    n4 = 1;

    % sin, cos for Fresnel coefficient (Incident angle = 1 deg)
    rad_theta1 = 1 / 180 * pi;
    cos_theta1 = cos(rad_theta1);
    sin_theta2 = n1 * sin(rad_theta1) ./ n2; cos_theta2 = sqrt(1 - sin_theta2.^2);
    sin_theta3 = n2 * sin_theta2 ./ n3; cos_theta3 = sqrt(1 - sin_theta3.^2);
    sin_theta4 = n3 .* sin_theta3 ./ n4; cos_theta4 = sqrt(1 - sin_theta4.^2);

    % Fresnel coefficient for s-polarization, p-polarization, respectively
    t1_s = (2.*n1 * cos_theta1) ./ (n2 .* cos_theta2 + n1 * cos_theta1);
    t2_s = (2.*n2.*cos_theta2) ./ (n3 .* cos_theta3 + n2 .* cos_theta2);
    t3_s = (2.*n3.* cos_theta3) ./ (n4 * cos_theta4 + n3 .* cos_theta3);

    t1_p = (2.*n1 .* cos_theta2) ./ (n2 * cos_theta1 + n1 .* cos_theta2);
    t2_p = (2.*n2 .* cos_theta3) ./ (n3 .* cos_theta2 + n2 .*cos_theta3);
    t3_p = (2.*n3 .* cos_theta4) ./ (n4 .* cos_theta3 + n3 .*cos_theta4);

    % Phase difference
```

```
    delta_Bi = 2*pi*n2*cos_theta2*Bi_d_thick/wavelength;
    delta_Si = 2*pi*n3.*cos_theta3.*(Bi_d_thick + d_thick_list)./wavelength;

    % Transmittance calculation for s-polarization
    A11_s = 1; A12_s = r1_s;
    B11_s = exp(1i * delta_Bi); B12_s = r2_s * exp(1i * delta_Bi);
    B21_s = r2_s * exp(-1i * delta_Bi); B22_s = exp(-1i * delta_Bi);
    C11_s = exp(1i * delta_Si); C21_s = r3_s .* exp(-1i * delta_Si);

    X11_s = (A11_s * (B11_s .* C11_s + B12_s .* C21_s)) + (A12_s * (B21_s .*
            C11_s + B22_s .* C21_s));

    r_s = t1_s .*t2_s.*t3_s./ X11_s; T_s = abs(t_s).^2;

    % Transmittance calculation for p-polarization
    A11_p = 1; A12_p = r1_p;
    B11_p = exp(1i * delta_Bi; B12_p = r2_p * exp(1i * delta_Bi);
    B21_p = r2_p * exp(-1i * delta_Bi); B22_p = exp(-1i * delta_Bi);
    C11_p = exp(1i * delta_Si); C21_p = r3_p .* exp(-1i * delta_Si);

    X11_p = (A11_p * (B11_p .* C11_p + B12_p .* C21_p)) + (A12_p * (B21_p .*
            C11_p + B22_p .* C21_p));

    t_p = t1_p.* t2_p.* t3_p ./ X11_p; T_p = abs(t_p).^2;

    % Sum of the transmittances
    tran_list = T_s * (1 - y) + T_p * y;
end
```

References

[1] O. S. Heavens, *Optical Properties of Thin Solid Films* (Butterworths, 1995), Chap. 4.

[2] T. Pisarkiewicz, "Reflection spectrum for a thin film with non-uniform thickness," Journal of Physics D: Applied Physics, **27,** 160(1994).

[3] R. T. Phillips, “A numerical method for determining the complex refractive index from reflectance and transmittance of supported thin films,” Journal of Physics D: Applied Physics, **16,** 489 (1983).

[4] D. F. Edwards, E. Ochoa, "Infrared Refractive Indexes of Silicon," Applied Optics, **19,** 4130 (1980).

[5] H.-J. Hagemann, W. Gudat, C. Kunz, “Optical constants from the far infrared to the x-ray region: Mg, Al, Cu, Ag, Au, Bi, C, and Al_2O_3,” Journal of the Optical Society of America, **65,** 6 (1975) and DESY report SR-74/7 (1974).

[6] S. Babar, J. H. Weaver, "Optical constants of Cu, Ag, and Au revisited," Applied Optics, **54,** 477-481 (2015).

[7] W. A. Pliskin, "Phase-shift corrections in determining the thicknesses of transparent films on reflective substrates," Solid-State Electronics, **11**, 10, 957-963 (1968).

[8] H. N. S. Krishnamoorthy, G. Adamo, J. Yin, *et al*., “Infrared dielectric metamaterials from high refractive index chalcogenides,” Nature Communications, **11,** 1692 (2020).

[9] S. Chen, C. Zhao, Y. Li, *et al*., "Broadband optical and microwave nonlinear response in topological insulator," Optical Materials Express, **4,** 4 (2014).

Chapter 5. Photothermoelectric response of BiSb

5-1 PTE response of a single BiSb detector

Figure 5.1.1 shows an illustration of a $Bi_{90}Sb_{10}$ PTE detector on a sapphire substrate. The Pt/Ta electrodes were formed to overlap the $Bi_{90}Sb_{0.1}$ film with an area of 50 μm × *w* (*w*: width of $Bi_{90}Sb_{0.1}$ film). The electrodes were designed long enough to facilitate wire bonding. MIR was irradiated onto the edge of each $Bi_{90}Sb_{0.1}$ film. The spot position of MIR was adjusted with a laser viewing card.

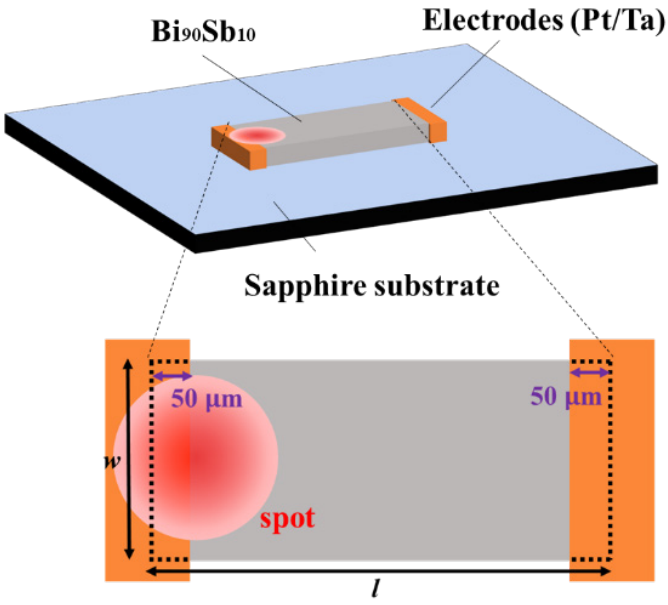

Fig. 5.1.1 An illustration of a sample of $Bi_{90}Sb_{10}$ film on a sapphire substrate. Pt/Ta electrodes were formed to overlap the $Bi_{90}Sb_{10}$ film with an area of 50 μm × *w*.

Figure 5.1.2(a)-5.1.2(c) show the PTE response of $Bi_{90}Sb_{10}$ slabs on sapphire with a

length of 4 mm, 10 mm, and 16 mm, respectively. At each length, we fabricated three types of devices with the width w = 2 mm, 0.5 mm, and 0.25 mm. Figure 5.1.2(d) summarizes the PTE maximum voltages of those devices. We observed the general trend that the PTE voltage is higher for longer l and shorter w.

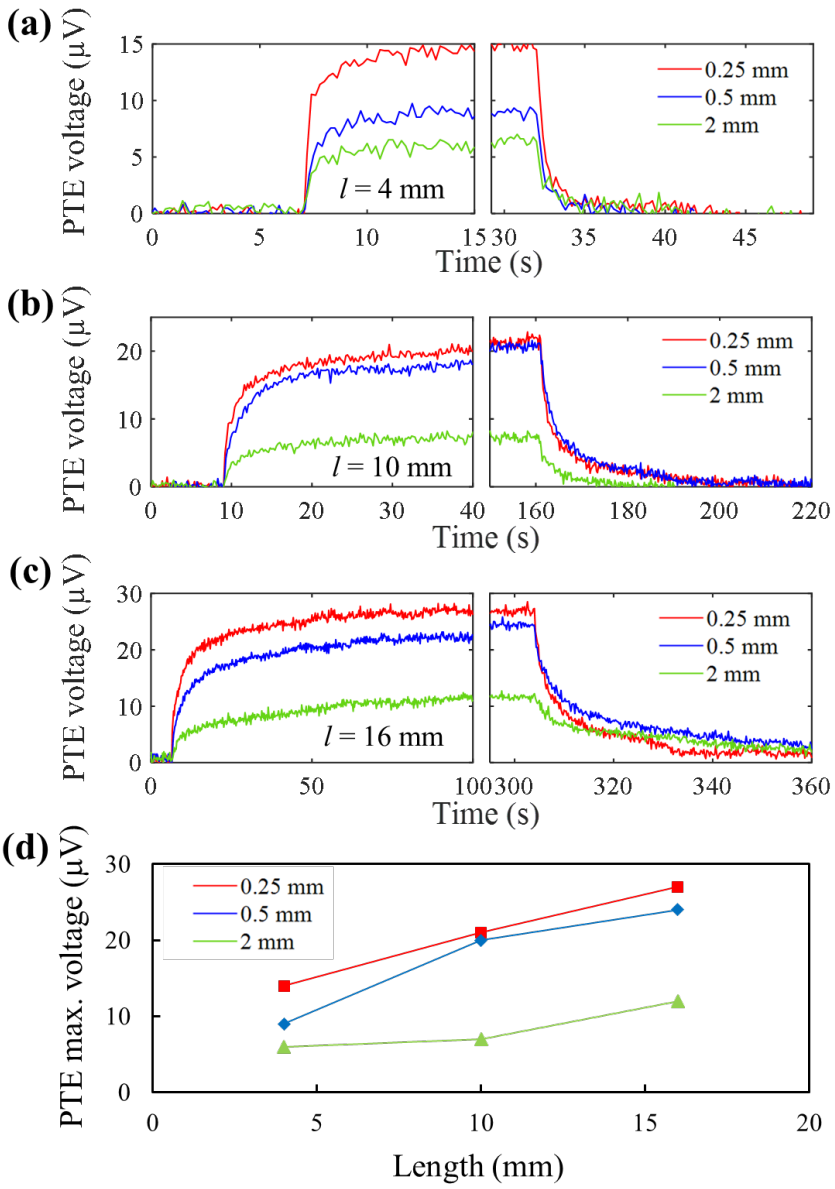

Fig. 5.1.2. PTE response of $Bi_{90}Sb_{10}$ films on a sapphire substrate with a length of (a) 4 mm, (b) 10 mm, (c) 16 mm and different widths. (d) PTE max. voltages of those samples.

For l = 4 mm samples, the maximum voltage is about 14 μV, 9 μV, and 6 μV, for w =0.25 mm, 0.5 mm, and 2 mm, respectively. For l =10 mm samples, the maximum voltage is about 21 μV, 20 μV and 7 μV, for w = 0.25 mm, 0.5 mm, 2 mm, respectively. For l =16 mm samples, the maximum voltage is about 27 μV, 24 μV and 12 μV, for w = 0.25 mm, 0.5 mm, 2 mm, respectively. These experimental results can be explained qualitatively by the Fourier's law for heat conduction in a $Bi_{90}Sb_{10}$ slab with the length L,

$$q = -k\frac{\Delta T}{L}$$

, where q is the heat flux density, k is the thermal conductivity of $Bi_{90}Sb_{10}$, and ΔT is the temperature difference between the two ends of the BiSb slab. At a fixed width, q is a constant, thus ΔT and consequently the maximum PTE voltage increase with longer L. Meanwhile, at a fixed length, q depends on the area-averaged laser power density received by the edge. When the width is 2 mm, which is larger than the laser spot size of about 1.5 mm, the area-averaged laser power density received by the edge is lower because the laser beam is Gaussian. When the width is reduced to 0.5 mm, the area-averaged laser power density received by the edge now approaches the Gaussian center power density, and it reaches maximum when the width is 0.25 mm.

From the data in Figs. 5.1.2(a)-5.1.2(c), we evaluated the rise time t_{on} and the fall time t_{off} of the PTE voltage. Table 1 shows t_{on} and t_{off} for each sample. We found that PTE response becomes faster with decreasing the size. However, not all the data follows the trend. In this measurement, as the differences between the spot size and the widths are small, it is thought to be in the margin of error, for l=4 mm, 10 mm. For l=16 mm, it takes more time to reach the max voltage and the trend is clearer that the sample of the smallest

width is the fastest to reach the max voltage. However, we note that there is a trend that, among the samples of a same length, a sample of the smallest width is the fastest to reach a certain voltage. For example, for l=4 mm sample, the fastest to reach 5 μV is w=0.25 mm sample, the slowest is w=2 mm sample, and this is true for l=10 mm, 16 mm samples, too.

Table. 5.1.1 On-time and off-time of each sample in Fig. 5.1.2.

w \ *l*	4 mm	10 mm	16 mm
0.25 mm	t_{on}~1.4 s, t_{off}~0.2 s	t_{on}~6.2 s, t_{off}~7.8 s	t_{on}~10 s, t_{off}~13 s
0.5 mm	t_{on}~1.3 s, t_{off}~1.2 s	t_{on}~8.0 s, t_{off}~10 s	t_{on}~25 s, t_{off}~32 s
2 mm	t_{on}~1.3 s, t_{off}~1.4 s	t_{on}~6.2 s, t_{off}~5.0 s	t_{on}~30 s, t_{off}~39 s

t_{on}: time to reach 80% of the maximum voltage after light-on.
t_{off}: time to fall to 20% of the maximum voltage after light-off.

Overall, we found that the noise floor is about 1 μV. As this noise is independent of the width and the length of the $Bi_{90}Sb_{10}$ slabs, this can be attributed to the measurement system with many electrical wiring bonding. Further lowering of measurement noise can be possible by using a dedicated measuring circuitry.

We estimated the noise (V_{noise}), noise equivalent power (NEP), and detectivity (D^*) of the detectors. As the PTE detector operates under zero voltage and the effect of the flicker noise can be avoided, the thermal noise (Johnson noise) is dominant[1]. The thermal noise (V_{noise}) and the responsivity ($\boldsymbol{R}$) were calculated as follows

$$V_{\text{noise}} = \sqrt{4k_{\text{B}}TR}$$

$$\boldsymbol{R} = \frac{V}{P_{\text{effect}}}$$

,where k_{B} is the Boltzmann constant, T is the temperature, R is the resistance, V is the PTE voltage, and P_{effect} is the effective power of irradiated IR at the detector. NEP [2] and D^* [3] were calculated as follows

$$\mathrm{NEP} = \frac{V_{\mathrm{noise}}}{\boldsymbol{R}} = \frac{\sqrt{4k_{\mathrm{B}}TR}}{V} P_{\mathrm{effect}}$$

$$D^* = \frac{\sqrt{A_{\mathrm{eff}}}}{\mathrm{NEP}}$$

,where A_{eff} is the area of the detection. The detectivity D^* and NEP are different in that D^*considers A_{eff} while NEP does not. As the laser was Gaussian beam, we calculated A_{eff}, P_{eff} as shown in Figure 5.1.3. These two parameters were calculated by the equation in Fig. 5.1.3(b) (numerical calculation by MATLAB).

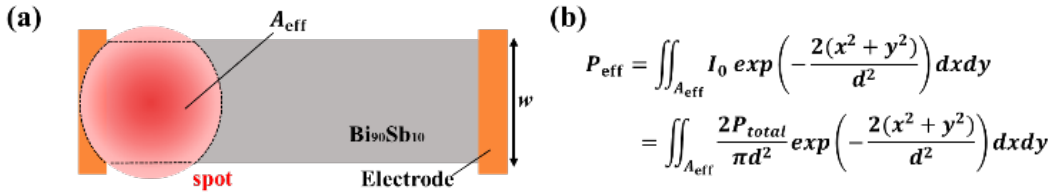

Fig. 5.1.3 (a) Illustration of how to calculate P_{eff} for NEP, assuming that the effective area A_{eff} is the region of the Gaussian beam spot that overlaps with the film the area (Gaussian intensity distribution). P_{total}: total power of the laser (=28.6 mW), d: radius of the beam spot (=0.75 mm). (b) The equation to calculate P_{eff}.

The calculations were performed under the condition of T=300 K. The results are shown in Table 5.1.2. V_{noise} are ~nV/$\sqrt{\mathrm{Hz}}$, NEP are ~μW/$\sqrt{\mathrm{Hz}}$, and D* are ~10^4 cm$\sqrt{\mathrm{Hz}}$/W. V_{noise} are 10^3 lower than the noise floor (~1 μV), which further verifies the aforementioned discussion of the cause of the noise floor. Comparing the D* with that of the recently reported IR PTE detector of Graphene/PEDOT (operating wavelength=4.3 μm)[4], it is one order lower ($6.95 \cdot 10^5$ cm$\sqrt{\mathrm{Hz}}$/W).

Table. 5.1.2 V_{noise}, P_{eff}, NEP and D^* calculated under an assumption as shown in Fig. 5.1.3.

	V_{noise}	P_{eff}	NEP	D^*
4 mm × 0.25 mm	$7.7\ \mathrm{nV}/\sqrt{\mathrm{Hz}}$	7.5 mW	$4.1\ \mu\mathrm{W}/\sqrt{\mathrm{Hz}}$	$1.5 \cdot 10^4\ \mathrm{cm}\sqrt{\mathrm{Hz}}/\mathrm{W}$
4 mm × 0.5 mm	$5.5\ \mathrm{nV}/\sqrt{\mathrm{Hz}}$	14 mW	$8.5\ \mu\mathrm{W}/\sqrt{\mathrm{Hz}}$	$1.0 \cdot 10^4\ \mathrm{cm}\sqrt{\mathrm{Hz}}/\mathrm{W}$
4 mm × 2 mm	$3.1\ \mathrm{nV}/\sqrt{\mathrm{Hz}}$	29 mW	$15\ \mu\mathrm{W}/\sqrt{\mathrm{Hz}}$	$9.0 \cdot 10^3\ \mathrm{cm}\sqrt{\mathrm{Hz}}/\mathrm{W}$

5-2 PTE response of a BiSb detector array

Based on the results of the single BiSb detector, we fabricated a 3×3 array of 4 mm × 0.25 mm elements, for a cell size of 5 mm × 5 mm. Figure 5.2.1(a) shows an illustration of the array. We labelled each row by “A, B, C” and each column by “1,2,3.” One edge of three elements in a row (e.g., A1, A2, A3) was connected to a common ground pad for simplification of the measurement setup. Figures 5.2.1(b)-5.2.1(d) shows the PTE response of the elements. Here, each element was illuminated individually to measure its standalone performance. The timing of laser irradiation was manually aligned across the measurements, as in Fig. 5.1.2. The maximum voltages are around 7-10 μV, which are smaller than that of 14 μV observed for the single device with same size in Fig. 5.1.2. One possible explanation for the reduction of PTE voltages in the array is that the extra common ground pads around the elements may add extra heat sinks to the large sapphire heat sink, resulting in more heat diffusion away from the edges. This leads to a smaller heat flow in the element and thus smaller PTE response.

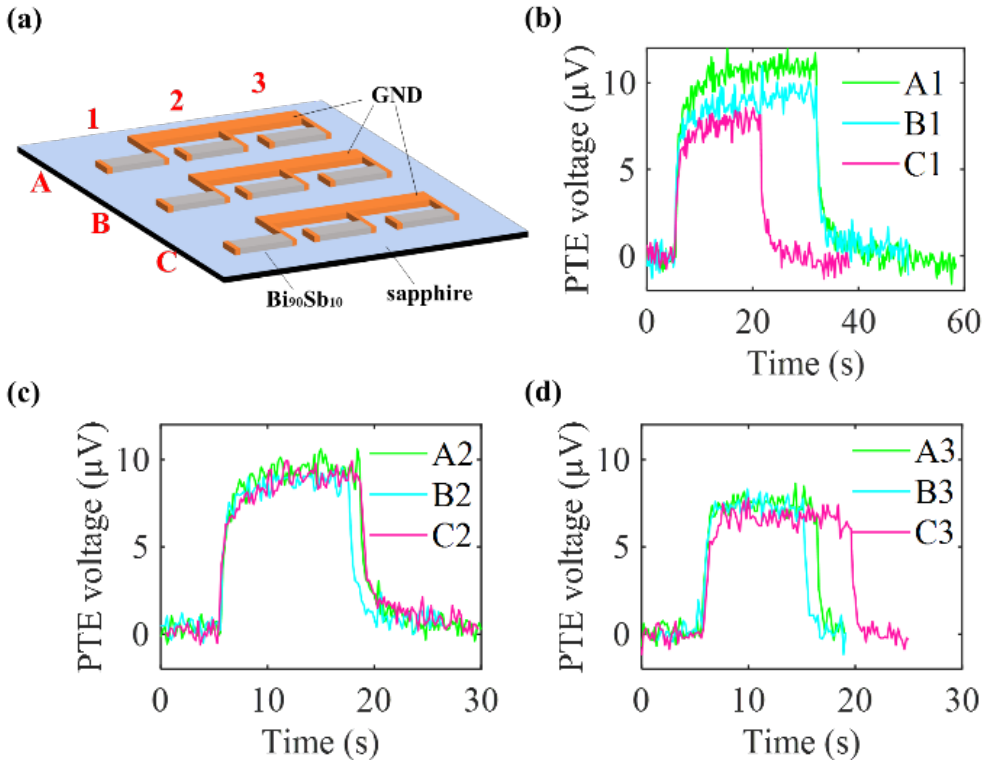

Fig. 5.2.1 BiSb PTE array with 3 × 3 elements. (a) An illustration of the array. (b)-(d) PTE responses of each three elements in the same column.

From the data in Figs. 5.2.1(b)-5.2.1(d), we evaluated the rise time t_{on} and the fall time t_{off} of the PTE voltage. Table 5.2.1 shows t_{on} and t_{off} for each element. There can be seen a rough trend that elements with longer ground pads operate slower. For example, the element Al operates slower than the element A3. This can be attributed to the size of the heat sink in the same way as the voltage.

Despite the smaller PTE voltages, the array can be used as an array detector for MIR imaging when the *D** is good enough.

Table. 5.2.1 On-time and off-time of each sample in Fig. 5.2.1.

column / row	1	2	3
A	t_{on}~1.5 s, t_{off}~1.6 s	t_{on}~1.2 s, t_{off}~1.5 s	t_{on}~0.8 s, t_{off}~1.0 s
B	t_{on}~1.5 s, t_{off}~1.2 s	t_{on}~0.7 s, t_{off}~1.2 s	t_{on}~0.7 s, t_{off}~0.6 s
C	t_{on}~1.4 s, t_{off}~1.0 s	t_{on}~1.7 s, t_{off}~1.7 s	t_{on}~0.7 s, t_{off}~0.9 s

t_{on}: time to reach 80% of the maximum voltage after light-on.
t_{off}: time to fall to 20% of the maximum voltage after light-off.

5-3 PTE response of a BiSb detector on a Kapton tape

To further increase the D^*, we fabricated a $Bi_{90}Sb_{10}$ PTE detector (4 mm × 0.5 mm × 81 nm) on a Kapton substrate. The Kapton substrate[5] has a significant lower thermal conductivity than the sapphire substrate[6]. The lower thermal conductivity of Kapton helps reduce the heat diffusion away from the edge and increase the heat flux in the BiSb slab, and leads to higher ΔT and PTE response. Figure 5.3.1(a) shows the illustration of a sample. We applied Ag paste to both ends of the slab as electrodes. Figure 5.3.1(b) shows the PTE response of the detector, which shows a significantly higher maximum voltage of 170 μV, lower NEP of $0.81\mu W/\sqrt{Hz}$, and higher D^* of $1.1\cdot 10^5$ $cm\sqrt{Hz}/W$. The D^* improved by one order and became the same order as that of the IR PTE detector of Graphene/PEDOT ($6.95 \cdot 10^5$ $cm\sqrt{Hz}/W$) [4]. The response times were t_{on}~ 1 s and t_{off}~1.2s, which are almost the same as that of BiSb/sapphire sample. The response time (thermal time constant) can be evaluated as follows[7]:

$$\tau = \frac{C_T}{G_T}$$

, where C_T is the total thermal capacitance (JK^{-1}), G_T is the total thermal conductance (WK^{-1}),of the detector. Representative values of thermal capacity are 0.77 $Jg^{-1}K^{-1}$(sapphire [8]), 1.09 $Jg^{-1}K^{-1}$(Kapton [9]), and those of thermal conductivity are 30 $Wm^{-1}K^{-1}$(sapphire [6]), 0.20 $Wm^{-1}K^{-1}$(Kapton [9]), respectively. The ratios of thermal capacity/thermal conductivity are 0.026 (sapphire), 5.45 (Kapton), respectively. From this calculation, it is estimated that BiSb/Kapton detector operates slower than BiSB/Sapphire detector. The mismatch between this calculated ratio and the actual ratio (~1) can be attributed to the conditions such as the contacts between BiSb and substrate (sapphire, Kapton), the difference of electrodes (Pt/Ta and Ag paste).

The large D^* of our BiSb PTE detector on the Kapton substrate and the recent development of organic semiconductor-based amplifier circuitries[10] indicate that BiSb can be used for a flexible MIR detector with large area and low fabrication costs.

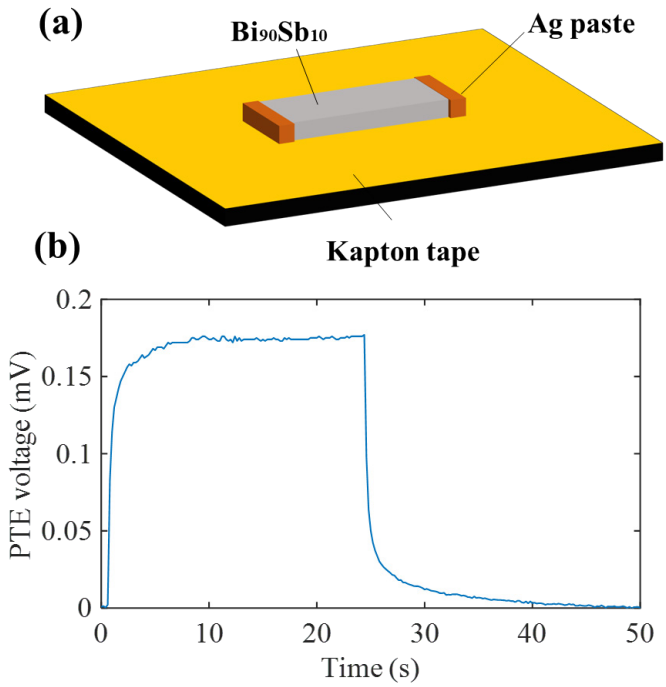

Fig. 5.3.1 $Bi_{90}Sb_{10}$ PTE detector on a flexible Kapton substrate. (a) An illustration of a

$Bi_{90}Sb_{10}$ slab with a size of 4 mm × 0.5 mm on a Kapton substrate. (b) PTE response of the detector.

References

[1] D. Suzuki, S. Oda, Y. Kawano., “A flexible and wearable terahertz scanner,” Nature Photon **10**, 809–813 (2016).

[2] D. Suzuki, Y. Ochiai, Y. Kawano, "Thermal Device Design for a Carbon Nanotube Terahertz Camera," ACS Omega, **3,** 3540-2547(2018).

[3] A. Das, M. L. Mah, J. Hunt, *et al*., "Thermodynamically limited uncooled infrared detector using an ultra-low mass perforated subwavelength absorber," Optica, **10,** 1018-1028(2023).

[4] G. Lu, J. Wang, W. Gao, *et al*., "Flexible Free-Standing Infrared Photothermoelectric Detector Based on Graphene/PEDOT," IEEE Nanotechnology Magazine, **19,** 6-13(2025).

[5] D.J Benford, T.J Powers, S.H Moseley, "Thermal conductivity of Kapton tape," Cryogenics **39,** 93-95(1999).

[6] D. Vaca, M. Barry, L. Yates, *et al*., "Measurements and numerical calculations of thermal conductivity to evaluate the quality of β-gallium oxide thin films grown on sapphire and silicon carbide by molecular beam epitaxy," Applied Physics Letters **121,** 042107 (2022).

[7] A. Das, M. L. Mah, J. Hunt, *et al*., "Thermodynamically limited uncooled infrared detector using an ultra-low mass perforated subwavelength absorber," Optica, **10,** 1018-1028(2023).

[8] S. Picard, D. T. Burns, and P. Roger, "Measurement of the Specific Heat Capacity of Synthetic Sapphire (α-Al2O3) from 293 K to 301 K," Bureau International des Poids et Mesures (2008).

[9] DuPont(corp),"DuPont^{TM}Kapton®,"https://www.dupont.com/content/dam/electronics/amer/us/en/electronics/public/documents/en/EI-10142_Kapton-Summary-of-Properties.pdf.”

[10] R. Kawabata, K. Li, T. Araki, *et al*., "Ultraflexible Wireless Imager Integrated with

Organic Circuits for Broadband Infrared Thermal Analysis," Advanced Materials **36,** 309864 (2024).

Chapter 6. Future prospects and Summary

6-1 Future prospects

6-1-1 Large area MIR PTE detector array

As shown in above chapters, high-quality BiSb can be deposited not only by the MBE technique but also by the magnetron sputtering technique, which can significantly reduce fabrication costs and increase the substrate size. Therefore, BiSb has a potential to be a good material for PTE MIR detection material with low fabrication costs and large substrate size with the help of large sputtering machine (Fig. 6.1.1.1). This is especially important when the substrate is required to be large and flexible, such as large non-intrusive cargo scanner, which can have size of ~ 1 m or larger.

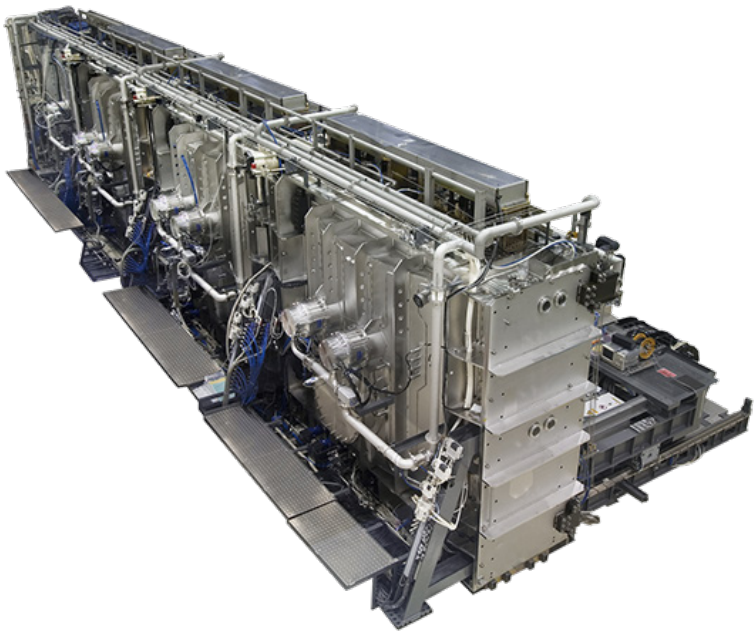

Figure 6.1.1.1 Sputter machine for large scale devices (ULVAC, Inc.) [1].

6-1-2 IR detector using interference dips

In addition to the investigation of optical constant of BiSb, we have observed the optical dip in the reflectance spectra of BiSb/Au samples (Fig. 6.1.2.1). As already investigated in another research [2], using the interference inside the BiSb film, we can enhance the absorption and thus the PTE response with adequate configuration of the device.

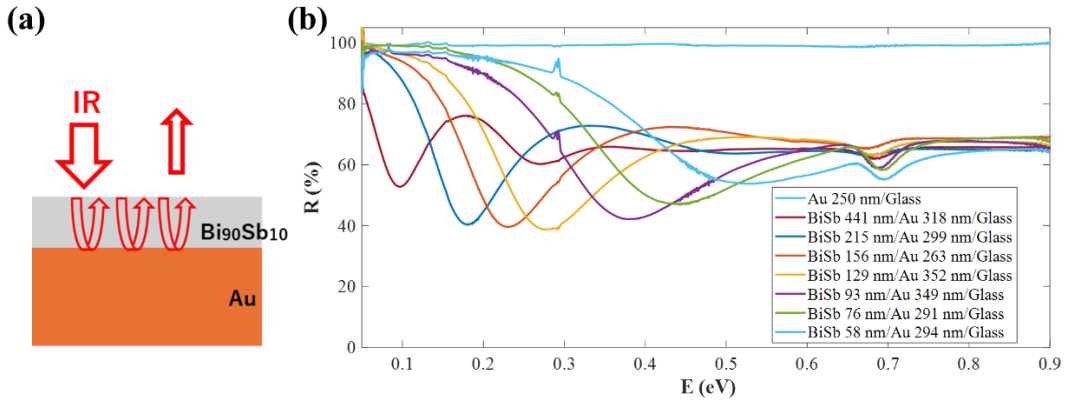

Fig. 6.1.2.1 (a) Schematic o IR irradiated BiSb/Au sample. (b) Reflection spectra of different BiSb thicknesses of BiSb/Au samples.

6-1-3 IR detector using spin Seebeck effect

There is a phenomenon called Spin Seebeck effect besides the normal Seebeck effect [3]. As BiSb is known for its large SHA and absorption in IR, it is possible that BiSb can be utilized for Spin Seebeck PTE IR detector using BiSb and a magnetic material (Fig. 6.1.3.1).

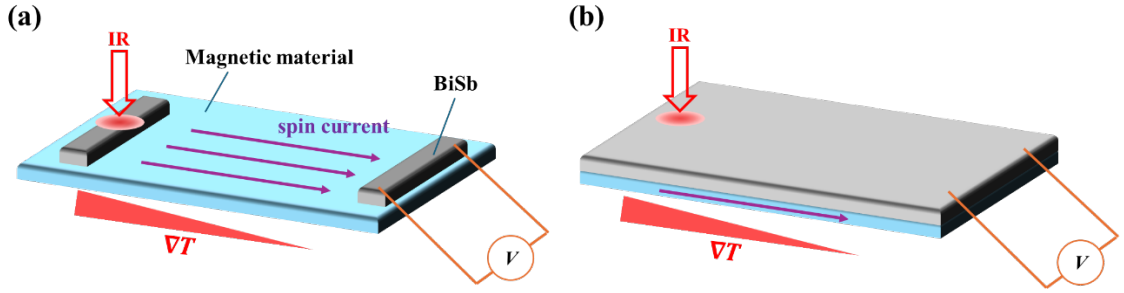

Fig. 6.1.3.1 Schematic of potential IR detector utilizing the spin Seebeck effect with the large SHA of BiSb. BiSb is placed at (a) edge, (b) on the surface of magnetic material, respectively.

6-1-4 Metamaterial application

There is a concept called topological insulator metamaterials in which that TI can be used among Photonics, Electronics, Spintronics (Fig. 6.1.4.1) [4]. As shown in chapter 4, BiSb has a high refractive index in the IR region. Another TI, Bi_2Te_3, also has a high refractive index, and optical resonance in IR has been observed for the Bi_2Te_3 nano slit arrays (Fig. 6.1.4.2) [5].

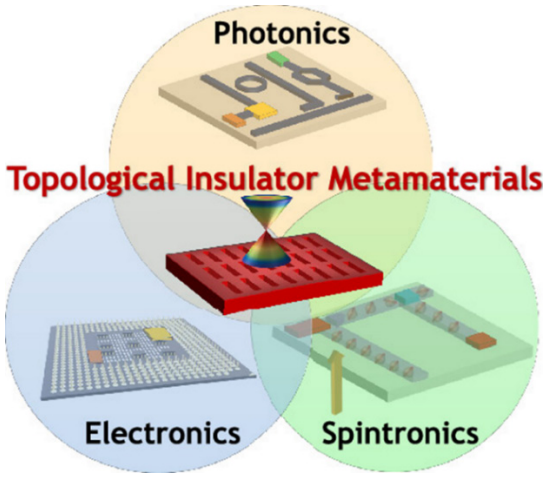

Fig. 6.1.4.1 Concept of TI metamaterials in photonics, electronics, and spintronics [4]. Reprinted with permission from Chemical Reviews.

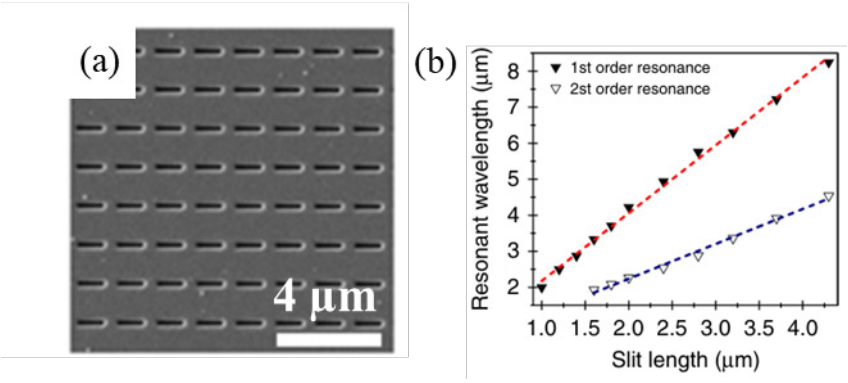

Fig. 6.1.4.2 (a) Image of slit arrays of Bi_2Te_3 with length L=4.3 μm. (b) IR resonance of the arrays with different length L [5].

6-2 Summary

This thesis presents the first comprehensive studies of the optical properties and device application of BiSb topological insulator in the infra-red region.

In Chapter 1, we introduced the background of this thesis, with focus on the IR technology and TI materials. We explained the importance of the IR technology and various types of IR detectors. We briefly explained TI and described BiSb as the first discovered 3D TI with a very small band gap. Finally, we stated the motivation for this research and the thesis outline.

In Chapter 2, we introduced the fundamental properties of BiSb as a TI and its potential for thermoelectric detectors. First, we explained previous applications of BiSb. Then, we discussed the prospect of BiSb as a material candidate for IR detectors, which is the most important part for this thesis as it supports the motivation of this thesis.

In Chapter 3, we showed experimental methods, including sample preparation, measurements. For sample preparation, we described three parts: selection of substrates, cleaning process, photolithography and evaporation. For measurement, we described the

thickness evaluation methods (XRR, XRF, digimatic indicator), evaluation of optical properties, and measurement of the PTE response.

In Chapter 4, we determined the (n,κ) of BiSb thin films by the RT method in the 0.1 eV- 1 eV range. Using the obtained (n, κ), we reveal that Bi, $Bi_{90}Sb_{10}$, and $Bi_{85}Sb_{15}$ show absorption of about 30% for film thicknesses around 20 nm and a large refractive index ranging from 6 to 9 in the infrared region. The high absorption is promising for use in PTE or PVE photodetector in MIR. Furthermore, the high refractive index of BiSb can be utilized to confine light and generate local heat with its high absorption, which can further enhance PTE. This chapter showed that BiSb has the potential to be a good material for MIR detectors, which can be fabricated with an easy process and low cost.

In Chapter 5, we demonstrated that $Bi_{90}Sb_{10}$ thin films fabricated by magnetron sputtering exhibit strong photothermoelectric responses in the MIR region. The PTE response was systematically evaluated for various device geometries. A maximum voltage of 27 μV was obtained for a 16 mm × 0.25 mm × 80 nm film on sapphire. A 3 × 3 array of 4 mm × 0.25 mm elements was demonstrated. Finally, we demonstrated a large PTE response of 170 μV with improved detectivity D^* of $1.1 \cdot 10^5$ cm$\sqrt{\text{Hz}}$/W for a BiSb-based PTE device on a Kapton flexible substrate. These results highlight the potential of sputtered BiSb thin films for high spatial resolution MIR detector arrays with low fabrication cost.

In Chapter 6, we discussed the future prospects and summarized this thesis. The use of sputtering enables fabrication on large-area and flexible substrates with lower cost and higher throughput compared to epitaxial growth methods. The key advantage lies in BiSb's suitability for scalable array-type MIR detectors using standard thin-film

processing techniques. Finally, we note that BiSb is a topological insulator with a giant spin Hall effect (SHE), thus new MIR detector concept utilizing the photothermal and spin Seebeck effects is possible in BiSb/ferromagnetic bilayers.

References

[1] https://www.ulvac.co.jp/products/sputtering_system/smd-vertical/

[2] S. Wredh, M. Dai, K. Hamada, *et al*., "Sb_2Te_3–Bi_2Te_3 Direct Photo–Thermoelectric Mid-Infrared Detection," Advanced Optical Materials, **12,** 2401450 (2024).

[3] K. Uchida, S. Takahashi, K. Harii, *et al*., "Observation of the spin Seebeck effect," Nature, **455,** 778 (2008).

[4] H. N. S. Krishnamoorthy, A. M. Dubrovkin, G. Adamo, *et al*., "Topological Insulator Metamaterials," Chemical Reviews, **123,** 8 (2023).

[5] H. N. S. Krishnamoorthy, G. Adamo, J. Yin, *et al.,* "Infrared dielectric metamaterials from high refractive index chalcogenides," Nature Communications, **11**, 1692 (2020).

Acknowledgments

I would like to thank Prof. Pham Nam Hai and Prof. Yukio Kawano (Chuo university) for supervising this study, and Prof. Shigeki Nakagawa, Prof. Takaaki Manaka, Prof. Akira Yamada, Assoc. Prof. Shinsuke Miyajima, Prof. Wakana Kubo (Tokyo University of Agriculture and Technology) for reviewing the doctoral thesis. Especially, Prof. Pham Nam Hai and Prof. Yukio Kawano have provided me with profound and insightful advice, grounded in their long and distinguished research careers, and have shown me the true fascination of research.

I would like to thank Assoc. Prof. Tomohiro Amemiya for the use of FTIR and the useful advice of the RT method regarding the 1st paper.

I would like to thank Prof. Tanaka (Hokkaido university), Assoc. Prof. Shun Hashiyada (Hokkaido university), for discussions on optics in my research.

I would like to thank Dr. Hiroki Ohkawa (Kanagawa Institute of Industrial Science and Technology; KISTEC) for the advice of the calculation codes of MATLAB and the discussions.

I would like to thank Prof. Takaaki Manaka and Assoc. Prof. Dai Taguchi for the training and the use of the evaporator.

I would like to thank Assoc. Prof. Yuya Shoji and the members of Shoji lab, especially Mr. Kousuke Nakanishi for the training and the use of the sputtering machine.

I would like to thank the members of the Pham lab, especially Dr. Takanori Shirokura, Dr. Ho Hoang Huy for the machine maintenance, training, and discussions. And I would like to thank Ms. Liu Min and Mr. Zhang Ruixian for working together

toward the doctor degrees, Mr. Sho Kagami and Mr. Kota Ejiri for the discussion, and Mr. Daiki Ito and Mr. Ohiro Fujie for the use of the machine.

I would like to thank the members of the Kawano lab (formerly at Tokyo Institute of Technology), especially Assist. Prof. Kou Li (now at Chuo university) for the training and valuable guidance and discussions from my master course, Mr. Jian Xiao, Mr. Tomoya Furukawa, Ms. Satsuki Yasui, Mr. Shota Wada for working together toward the master degrees, Mr. Toshio Sugaya for the valuable guidance and discussions throughout my master course, Mr. Kouki Miura for the discussion on the Tamm plasmon polariton, and Dr. Takuya Okamoto for the discussion on the SNOM and the valuable advice.

I would like to thank Dr. Takamasa Kawanago for the useful advice of the fabrication process for my master course.

I would like to thank the engineering staffs of Mechano-Microprocess Cleanroom (Semiconductors and MEMS Processing Division, Core Facility Center), especially Dr. Akihiro Matsutani for the support of the fabrication process in my master course.

I would like to thank the engineering staffs of Collaboration Center for Design and Manufacturing, especially Ms. Takako Kanai for the training and use of the SEM from my master course.

I would like to thank the members of the Kawano lab (Chuo university), especially Mr. Miki Kubota for the training and use of the measurement system, Mr. Yukito Kon for the discussion on the detector array, Mr. Daiki Shikichi for the use of the MIR laser, Mr. Hayato Hamashima for the use of the digital multimeter, Mr. Reo Takai for the discussion on the detectors, Mr. Masakazu Konishi, Mr. Ryoga Odawara, Mr. Kota

Shirahata, and Mr. Aozora Ohi for the discussion mainly on the plasmonics. And I would like to thank Mr. Yuto Aoshima, Mr. Yuya Kinoshita, Mr. Daiki Sakai, Mr. Kosei Tanizaki, and Mr. Ryo Harashima, with whom I shared the early stage of the Kawano lab in Chuo university.

I would like to thank the engineering assistant staffs in Kawano lab (Chuo university), especially Ms. Noa Izumi for the use of the measurement system, Ms. Norika Takahashi for being a part of the starting member of the Kawano lab in Chuo university. And I would like to thank the administrative staffs, especially Ms. Hiromi Nakamura (Chuo University) for the assistance from the early stage of the Kawano lab in Chuo university.

I would like to thank Assoc. Prof. Masahiko Nakase for the use of a three-dimensional laser scanning microscope.

I would like to thank the engineering staffs of Materials Analysis Division, Open Facility Center of Institute of Science Tokyo, especially Mr. Hiroshi Iida, Mr. Yuichi Suzuki, and Mr. Ryo Ohta for the training and use of XRR, XRF, and ICP equipment.

I would like to thank the corporations for their valuable technical support and assistance with the experimental apparatus. Especially, I would like to thank Shimadzu Corporation, Advantest Corporation, and Rigaku Corporation.

I would like to thank the staffs of KISTEC for the use of FTIR and their administrative supports.

I would like to thank the staffs of Research Laboratory of Ultra-High Speed Electronics for the use of the digimatic indictor, P-CVD, sputtering machine, spin coater.

I would like to thank TIRI (Tokyo Metropolitan Government established Tokyo Metropolitan Industrial Technology Research Institute), especially Mr. Shuichi Date for the support of the fabrication process.

I would like to thank the engineering staffs of Takeda clean room (the University of Tokyo) for the training and use of machines and discussions in my doctoral course.

I would like to thank the Tsubame scholarship for the financial support throughout my doctoral course.

Finally, I would like to show my deepest appreciation to my family for their constant support throughout my PhD and daily life.

Publications and presentations

Reviewed Journal Papers

[1] H. Nishiyama, P. N. Hai., T. Amemiya, S. Hashiyada, and Y. Kawano, “Infrared optical constants n, κ of topological insulator BiSb thin film determined by reflectance-transmittance technique,” Optics Letters, to be published.

[2] H. Nishiyama, P. N. Hai, Y. Kawano, “Mid-infrared photothermoelectric detector using topological insulator BiSb thin film,” Optical Materials Express 16, 603 (2026). https://doi.org/10.1364/OME.571598

Presentations

[1] 西山 黎, ファム ナムハイ, 河野 行雄. “トポロジカル絶縁体 BiSb を用いた中赤外検出の検証”, 第 73 回応用物理学会春季学術講演会, Mar. 2026.

[2] 西山 黎, ファム ナムハイ, 雨宮 智宏, 橋谷田 俊, 河野 行雄. “RT 法による BiSb の赤外光学定数および吸収の評価”, 第 73 回応用物理学会春季学術講演会, Mar. 2026.

[3] 西山 黎, ファム ナムハイ, 橋谷田 俊, 河野 行雄. “トポロジカル絶縁体 BiSb のテラヘルツ分光特性”, 第 71 回応用物理学会春季学術講演会, Mar. 2024.

[4] 西山 黎, ファム ナムハイ, 橋谷田 俊, 河野 行雄. “トポロジカル絶縁体 BiSb のテラヘルツ吸収特性”, 日本光学会年次学術講演会, Nov. 2023.